NONISOTHERMAL FILM CASTING OF A VISCOUS FLUID

By

W. SPENCER SMITH, B. ENG. C.S.

A Thesis Submitted to the School of Graduate Studies

in Partial Fulfilment of the Requirements

for the Master of Engineering Degree.

McMaster University

MASTER OF ENGINEERING (1997) **McMaster University**
(Civil Engineering) **Hamilton, Ontario**

TITLE: **Nonisothermal Film Casting of a Viscous Fluid**

AUTHOR: **Spencer Smith, B.Eng. C. S. (McMaster University)**

SUPERVISOR: **Dr. D. F. E. Stolle and Dr. B. Koziey**

NUMBER OF PAGES: **xvi, 146**

Abstract

Finite element models were developed for simulating one-dimensional (1D) and two-dimensional (2D) nonisothermal film casting of a viscous polymer. These models accommodate inertia and gravity, allow the thickness to vary across the width of the film (in the 2D case), but exclude die swell and sag. The numerical algorithm is based on a Newton-Raphson approach to solve simultaneously for the velocity, thickness, temperature and the width of the film. Numerical simulations using the finite element model found the following:

i) upwinding is unnecessary for predicting the temperature distribution;

ii) the average temperature distribution in the air gap is well approximated by a linear function;

iii) once the film contacts the chill roll the geometry remains essentially unchanged;

iv) for low viscosity polymers, the self-weight of the material can aid in reducing neck-in and in promoting a uniform thickness;

v) nonconstant thickness and/or velocity profiles at the die could potentially lead to less neck-in and a more uniform thickness for the finished product; and

vi) cooling of the film, especially when localized cooling jets are employed, reduces neck-in and promotes a uniform thickness.

Acknowledgments

I would like to extend my gratitude to my supervisors, Dr. Stolle and Dr. Koziey, for the considerable effort they exerted on my behalf. In addition, I wish to thank Dr. Stolle's other graduate students for their interest and help. The assistance, financial and otherwise, of the Civil Engineering Department at McMaster University is also greatly appreciated. Furthermore, I would like to acknowledge the financial support provided by the Natural Sciences and Engineering Research Council of Canada. Finally, I would like to thank my friends and family, especially my brother, mother and the Aussems (for the loan of their computer!).

Table of Contents

List of Figures

List of Tables

List of Symbols

The symbols used in this thesis are defined on their first usage.

Chapter 1

Symbol	*Meaning*
Dr	Draw ratio
u	Speed of the film in the machine direction

Subscript	*Meaning*
die	At the die
roll	At the roll

Chapter 2

Symbol	*Meaning*
$\overline{h}$	A characteristic film thickness
$\overline{T}$	Mean temperature across the film's cross-section
$\overline{W}$	Weighting factor
α	Heat transfer coefficient
Δ	Change in the subsequent variable
δ	Virtual quantity or weighting function
δ_{ij}	Kronecker delta, equal to 1 when i = j, otherwise equals zero
η	Shear viscosity
η_p	Planar elongational viscosity
κ	Thermal diffusivity
ν	Kinematic viscosity
ξ	Optimum integration point for upwinding
ρ	Density
σ_{ij}	Stress tensor
$\boldsymbol{\psi}$	Residual vector
a, c, d	Parameters for the temperature dependence of viscosity
$\mathbf{a}$	Degree of freedom vector
b	Acceleration

C	Specific heat capacity
Cn	Capillary number
D/Dt	Material or substantial derivative
E	Activation energy
F	Tension in the film
g	Acceleration due to gravity
Gz	Graetz number
h	Thickness of the film
h	Vector of thickness degrees of freedom
J	Determinant of the Jacobian of transformation
K	Stiffness matrix
k	Thermal conductivity
$\mathbf{K}_T$	Tangential stiffness matrix
L	Length of film from the die to the point where the film sticks to the roll
L_{gap}	Length of the film in the air gap
L_{roll}	Length of the film on the chill roll from contact to where the film sticks
m	Constant used in closed-form solution for nonisothermal velocity
N	Shape function matrix
N_i	Shape function for node i
Nu	Nusselt number
O^e	Origin of an isoparametric element
p	Hydrostatic pressure
Pe	Peclet number
Pr	Prandtl number
Q	Mass flux
q	Thermal flux due to conduction
R	The gas constant (8.314 J mol^{-l} K^{-1})
R	Load vector
Re	Reynolds number
S	Surface energy per unit area
T	Vector of temperature degrees of freedom
T	Temperature
t	Processing time
U	Dimensionless velocity for film falling under its own weight
u	Vector of velocity degrees of freedom
u_1, u_2, u_3	Velocity in the machine, transverse and out-of-plane directions
u_{air}	Speed of the forced air relative to that of the film
W	Weight of the film
X	Dimensionless distance for film falling under its own weight
x_1, x_2, x_3	Axes in the machine, transverse and out-of-plane directions, respectively
$\|\|$ $\|\|$	Euclidean norm of a vector

ε_{ij}	Rate of deformation tensor

Subscript	*Meaning*
0	For reference values
1, 2, 3	Corresponding to nodes 1,2 and 3, respectively
advt	Contribution to conservation of energy equation from advection
air	Associated with the air surrounding the film
cond	Contribution to conservation of energy equation from conduction
cont	Applies to the continuity equation
eqlb	Applies to the equilibrium equation
f	Property of a fluid
gap	Over the air gap
grad	Contribution to equilibrium balance from the stress gradient
h	Applies to the thickness
i, j, k	For index notation over three dimensions
inrt	Contribution to the equilibrium balance from inertia
L	Over the distance L
n	An integer
newt	Contribution to the conservation of energy from Newton's Law of Cooling
p	Property of a plate
s	Applies to the solidification temperature
T	Applies to the temperature
thrm	Applies to the conservation of energy
u	Applies to the velocity
water	Applies to water

Superscript	*Meaning*
T	Transpose of a matrix

Chapter 3

Symbol	*Meaning*
$\bar{T}_{\alpha}$	Applied traction vector
Γ	Boundary of the film
Ω	Domain of the film
b_{α}	Acceleration vector
n_{α}	Surface normal vector
q_{α}	Thermal flux vector

s	Arc-length coordinate along the free surface
u_α	Velocity vector
w	Half width of the film

Subscript	*Meaning*
α, β, γ	For index notation in two dimensions
free	Along the free surface of the film
sym	At the line of symmetry of the plane of the film

Appendix A

Symbol	*Meaning*
θ	A constant used for the temperature distribution in a moving sheet
A, z	Parameters used for the closed-form solution for 2D film casting
C_1, C_2	Constants used in the derivation of the closed-form solutions
k_0, r, y_1, y_2	Parameters used for the closed-form solution of the velocity for a curtain of viscous fluid

Superscript	*Meaning*
^	Used for the variable of integration

Appendix B

Symbol	*Meaning*
$\boldsymbol{\varepsilon}$	Vector of rate of deformation components
$\boldsymbol{\sigma}$	Vector of stress tensor components
B	Matrix of shape function derivatives
D	Constitutive matrix
le	One-dimensional finite element length
∇	Gradient operator

Subscript	*Meaning*
u	Associated with the velocity vector
s	Associated with the thickness and temperature scalars

Chapter 1 Introduction and Background

Cast film production is a large component of the polymer processing industry. The global output of cast film was 2.79 million tonnes in 1996 and is expected to grow to 3.65 million tonnes by the year 2000 (Gabriele 1996). This growth trend in the industry puts pressure on cast film technology to improve both the quantity and quality of the film produced. In determining how to accomplish this, the designer of a cast film line is currently forced to rely on experimental and trial-and-error approaches, rather than on theoretical analyses and numerical simulations. Increasing the contribution of theory to the design phase would make it possible for more design alternatives to be investigated and optimized, before resorting to experimentation. This would provide three potential advantages:

i) a reduction in the time required for design;

ii) a reduction in materials wasted in experimentation; and

iii) a more efficient final design.

These advantages translate directly into economic and environmental benefits. The economic benefit is reduced cost because of the reduction in wasted time and materials, while the environmental benefit is the reduction in wasted materials that have to be scrapped. A more efficient final design is important for gaining both benefits because even a small percentage improvement results in a significant reduction in wastage, given

the large amounts of film produced. As a step toward realizing the above advantages, this thesis contributes to the theoretical and numerical modelling of the cast film process.

This chapter acts as the introduction and background for the subsequent development of the theoretical model and numerical solution technique. Section 1.1 provides an overview of the cast film process, which includes the uses of the finished product, identification of the range of material and processing conditions, and a description of the overall process. Section 1.2 consists of a literature review that identifies the current state of theoretical knowledge on film casting. This review provides the context for further studies by showing what has been researched and what areas are still open to investigation. Given this context, Section 1.3 details the contribution of this study through a description of its purpose and scope.

1.1 Description of the Cast Film Process

Film casting produces plastic sheets for many different applications, such as plastic bags, packaging for food and other consumer products, magnetic audio and video tape, and air and vapour barriers used in construction applications. Films are also produced by the blown film process, but film casting is generally preferred when a uniform thickness or a smooth surface is needed, or when products are manufactured with low viscosity polymers (Cotto, Duffo and Haudin 1989). Cast film is also considered superior to blown film for clarity, efficiency, and coextrusion operations (Keller 1989). Coextrusion is used to produce films with multiple layers where each layer contributes a desired trait to the finished product, such as impermeability to oxygen or moisture, heat

sealability, strength, chemical resistance, or colour. Although this thesis focuses on polymer films, similar film casting processes are used in the production of metal foils. Furthermore, the physics of film casting closely resemble those for curtain coating, which is used to apply lacquer or paint to a continuously moving substrate.

1.1.1 Materials and Processing Conditions

To produce sheets for the broad variety of uses described above, an extensive range of materials and processing conditions are used by manufactures. A few examples of film casting materials are low density polyethylene (LDPE), high density polyethylene (HDPE), polyethylene terephthalate (PET), polystyrene (PS), and polypropylene (PP). These polymers cover a large range of viscosity values, from 10^2 Pa·s to 10^5 Pa·s. The range of processing conditions is also large due to the wide range of products manufactured. In fact, the processing conditions can be set for film with a width of between 0.1 m and 10 m (Pearson 1985: 473) and with a thickness of between 20 μm and 2000 μm (Pearson 1985: 473). Another indication of the diversity of the processing conditions used, is that the throughput can be between 20 kg/h and 2000 kg/h.

1.1.2 An Overview of the Cast Film Process

Figure 1.1 provides an overview of a typical continuous film casting operation. At the left side of the figure the solid polymer, usually in pellet form, enters the extruder from the hopper. The extruder consists of a screw that melts the polymer and provides the pressure for it to exit the centre-fed “T” or coat-hanger die. After exiting the die, the film is exposed to the air where it is cooled by convected cold air or an inert gas before it contacts the thermoregulated chill roll. To ensure good contact of the film with the chill

roll and to aid in freezing, an air knife is used to blow a jet of air at the film. Up to this point the film is called the primary film; once it is outside the air gap region however, it is termed the secondary film. After freezing, the secondary film is hauled off for further treatment, such as biaxial stretching. Once treated, the finished product goes to a winder that puts the film onto rolls, which is the final stage shown on the right of Figure 1.1. Some examples of winder technology are described in Kreisher (1993) and Wilder (1991).

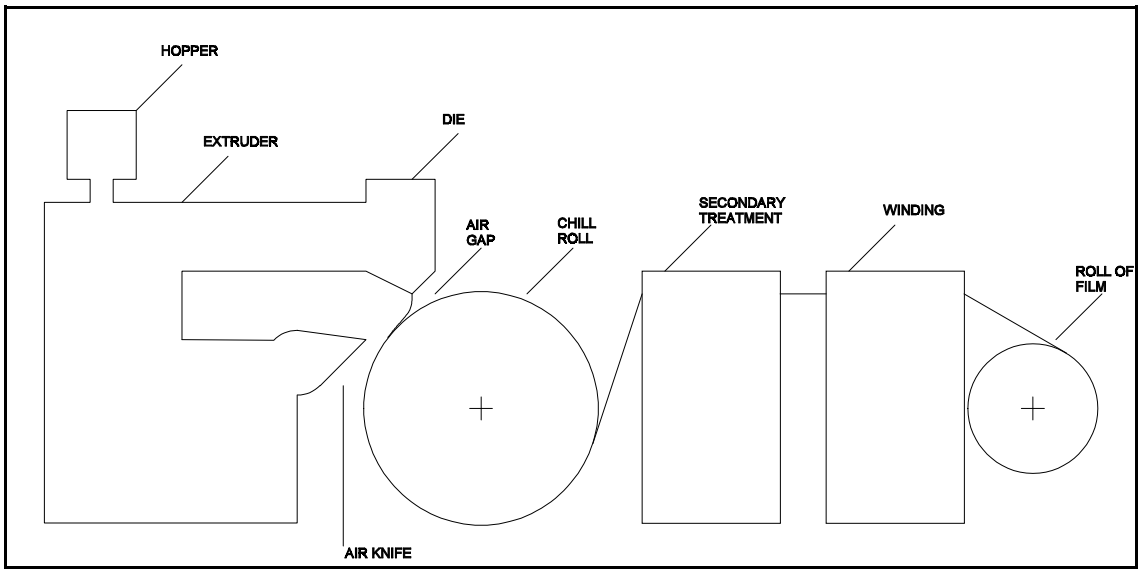

Figure 1.1 Overview of the cast film process

Although the preceding description is typical for film casting, variations on this approach are possible. For instance, air jets can be added in the air gap region to freeze the edges of the film, thereby reducing tearing problems. Another variation is to replace the air knife with an electrostatic pinning system (Barq et al. 1992) that consists of a high voltage wire held parallel to the zero voltage roll. The wire creates an electric discharge and the associated electrostatic force is responsible for pinning the film to the roll. A

vacuum box is another alternative to an air knife. This device removes the air, plus air-born dirt and contaminants, from beneath the film and the negative pressure forces intimate contact between the film and the roll (Flanagan 1993). An alternative to the chill roll shown in Figure 1.1, is to use a water bath to freeze the film. Many options are also available when it comes to the secondary treatment phase, with the choice of treatment depending on the properties required of the finished product. For the secondary treatment of magnetic films, the polymer is held at a temperature just below the film's melting point while being stretched in the transverse and longitudinal directions. This is followed by stabilization of the film in an oven maintained at a temperature of approximately 100 °C. Further details of this process are presented in d'Halewyu et al. (1990).

1.1.3 The Behaviour of the Film in the Air Gap

Studies on film casting, including the one presented in this thesis, focus on how the film behaves in the air gap because the properties of the finished product are mainly determined here (Barq et al. 1992). The air gap behaviour is important as the success of downstream operations depends on the quality of the film supplied from upstream. A close up schematic of the air gap is shown in Figure 1.2. Just outside of the die, the film swells due to the sudden change from a confined shear flow to an essentially extensional flow field. To keep the reduction in the width (neck-in) as small as possible, the air gap length is kept short, generally only a few centimetres. Besides trying to reduce neck-in, film line designers also want to control a defect called "edge bead" or "dog-bone." This defect appears as an increase in thickness at the film's edges, which is typically several centimetres wide and can be five times the thickness of the middle of the film (Dobroth

and Erwin 1986). Edge beads are a problem, as they can lead to entrapped air between the film and the roll. In addition, edge beads have to be trimmed and then either scrapped or recycled. For these reasons, manufactures consider it desirable to reduce edge bead size, although not necessarily to eliminate them entirely, since an edge bead can be helpful in reducing neck-in and in ensuring the uniformity of the thickness over the rest of the film's width (Pearson 1985: 476). In fact, to gain these benefits, some production lines intentionally add edge beads.

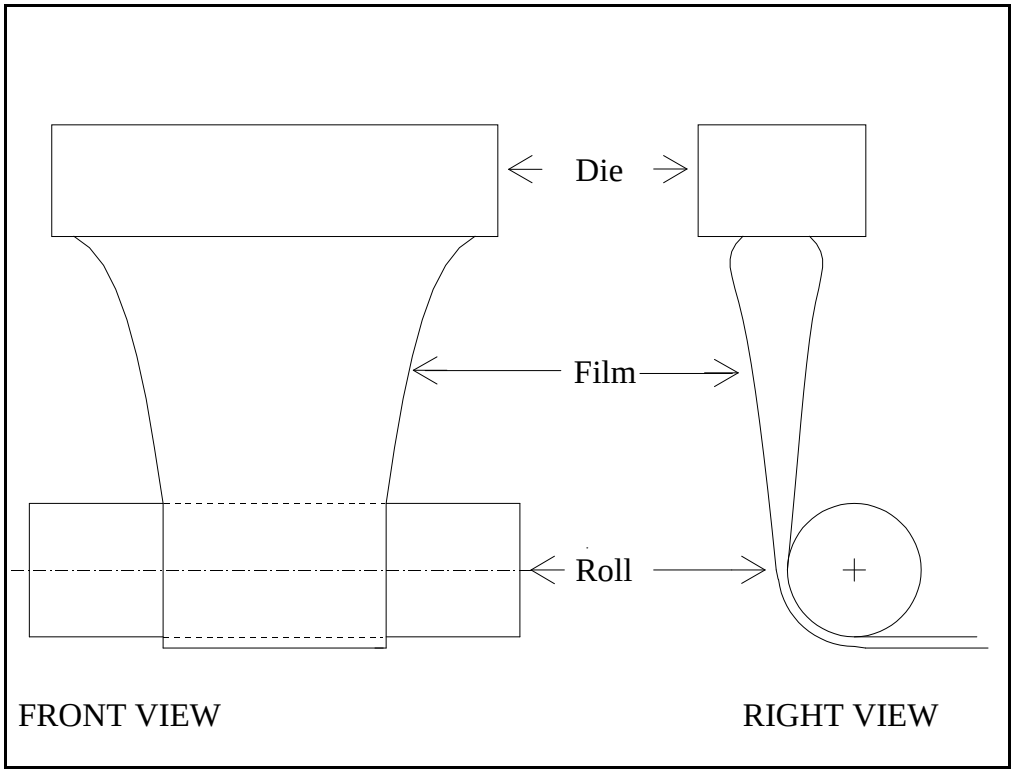

Figure 1.2 Overview of the cast film process in the air gap

1.1.4 The Draw Ratio and Draw Resonance

The properties of the film in the air gap are influenced considerably by the amount of stretching. The dimensionless number used to express stretching is the draw ratio (Dr), which is defined as

$$Dr = \frac{u_{roll}}{u_{die}} \tag{1.1}$$

where u_{roll} and u_{die} are the velocities of the film, at the chill roll and die, respectively. The value of Dr is typically between 2 and 20 (Pearson 1985: 475), although some film lines operate with Dr as high as 40 or more. A potential problem, termed draw resonance, exists when the draw ratio is too high. Draw resonance consists of a periodic variation of the film's width and thickness, even at steady state operations.

1.2 Literature Review on Cast Film

Compared with other industrial polymer processing techniques, simulation of film casting has not received as much attention in the literature. Therefore, before considering the research done specifically on cast film, it is worthwhile to look at the applicability of related work on membrane deformation, coating flows and fibre spinning.

Studies on the deformation of Newtonian and viscoelastic membranes (Wineman 1976; White 1975; Acierno et al. 1976) have limited applicability to film casting because, unlike film casting, the thickness is assumed constant over the membrane at each time step. Research on coating flows (Kistler and Scriven 1983; Brown 1961) and on a curtain of Newtonian fluid falling under its own weight (Adachi et al. 1988) include the effects of

changes in thickness, but differ from the film casting process because they do not allow for displacement control at the roll. Furthermore, coating flows, unlike film casting, involve low viscosity fluids and complications caused by unusually shaped fluid and solid surfaces. Fibre spinning studies (Mewis and Petrie 1986; Denn 1980) also consider issues related to film casting, but whereas fibre spinning is essentially one-dimensional, film casting is two-dimensional. From the preceding discussion, film casting clearly has requirements that are not addressed by the related research.

The following literature review addresses film casting's special requirements. To start with, the mathematical models proposed in the literature are discussed. Next, the solution techniques used in solving the mathematical models are reviewed and finally, the experimental data available from the literature are identified.

1.2.1 Mathematical Modelling of Film Casting

A mathematical model for film casting describes the physics of the process; that is, it provides the governing equations for continuity, equilibrium, and conservation of energy. Such a model must also address the selection of an appropriate constitutive equation and boundary conditions. Several different mathematical models of film casting have been presented in the literature. These models are distinguished from one another by the simplifying assumptions made; for example, all of the proposed models assume that surface tension, air drag and die swell effects can be neglected. The most general model proposed to date is provided by Pearson (1985: 473-479). His model is fully two-dimensional and can capture both neck-in and edge bead phenomena. Furthermore, the model allows for inertia, gravity, the sag of the sheet and nonisothermal conditions.

Unfortunately, owing to the complexity of the model and the lack of a specific constitutive law, Pearson (1985: 473-479) presents the governing equations, but does not solve the system. Other models, which are less general, have been used to develop solutions for specific film casting boundary-valued problems. A summary of these models is given in Tables 1.1 and 1.2. Table 1.1 has the models associated with draw resonance research, whereas Table 1.2 has the models used in simulation studies. These tables compare the research according to: the number of dimensions allowed; whether the model is for isothermal conditions; the constitutive law used and whether the model includes edge beads. For the dimension column, the model is considered one-dimensional (1D) if the width of the sheet is either assumed constant or infinite. On the other hand, the two-dimensional (2D) models allow the width to vary and the 3D model makes no restrictive assumption about how the variables change with respect to direction.

Table 1.1 Summary of the Mathematical Models in Draw Resonance Research

Reference	Dim	Constitutive Equation	Thermal	Edge Bead
Yeow (1974)	1D	Newtonian	iso	N
Aird and Yeow (1983)	1D	Power-Law	iso	N
Minoshima and White (1983)	1D	Newtonian	noniso	N
Lee (1984)	2D	Power-Law	iso	N
Anturkar and Co (1988)	1D	Modified Convected Maxwell	iso	N
Barq et al. (1990)	1D	Newtonian	iso	N
Silagy et al. (1996a)	2D	Newtonian	iso	N
Silagy et al. (1996b)	2D	Newtonian	iso	N
Iyengar and Co (1996)	1D	Modified Giesekus	iso	N

The theoretical models used for draw resonance research are generally simpler than those used for simulation studies because the interest is on predicting the critical draw ratio, not on finding precise steady state values. This is illustrated by the fact that all of the research on the stability of film casting neglects the edge bead defect and only three of the nine studies cited allow for neck-in. Moreover, those studies that do include neck-in, do so in a simplified manner. For example, the model proposed by Lee (1984) does not actually predict neck-in, but instead uses it as an input parameter. Silagy et al. (1996a, 1996b) reduce the complexity of the neck-in phenomenon by using a simplified flow field and neglecting the shear terms in the rate of deformation tensor. Another simplification that is common to the models proposed in the stability research, is the assumption that the process is isothermal. The only exception to this is the study by

Minoshima and White (1983), but their focus is on comparing the heat transfer behaviour of film casting with fibre spinning and blown film extrusion, rather than on finding a specific solution for their system of equations.

The main area for complexity in the stability research comes from the constitutive laws considered. Table 1.1 shows that four of the nine studies cited use non-Newtonian fluids. Two of these studies are for power law fluids (viscosity depends on the shear rate) and the other two introduce viscoelasticity. The viscoelastic equations studied are all of the differential type. That is, some objective measure of the stress rate appears in the constitutive equation.

From examining the models proposed in the draw resonance research, one finds that they are too simple to predict neck-in, edge beads and nonisothermal effects.

Table 1.2 Summary of the Mathematical Models Found in Simulation Studies

Reference	Dim	Constitutive Equation	Thermal	Edge Bead
Avenas et al. (1986)	2D	Newtonian	iso	N
Cotto, Duffo and Haudin (1989)	2D	Newtonian	noniso	N
d'Halewyu, Agassant and Demay (1990)	2D	Newtonian	iso	Y
Duffo, Monasse and Haudin (1991)	2D	Newtonian	noniso	N
Agassant et al. (1991)	2D	Newtonian	iso	N
Alaie and Papanastasiou (1991)	1D	BKZ-type integral	noniso	N
Barq et al. (1992)	2D	Newtonian	noniso	N
Iyengar and Co (1993)	1D	Modified Giesekus	iso	N
Debbaut et al. (1995)	2D	Power-Law, Maxwell-B and Giesekus	iso	Y
Sakaki et al. (1996)	3D	Newtonian	iso	Y

Table 1.2 summarizes the simulations studies, which use mathematical models that are characterized as one, two or three-dimensional. The 1D models proposed have the drawback that they cannot show neck-in or edge beads. Alaie and Papanastasiou (1991) also suggest that a 1D model may make poor predictions near the die due to flow rearrangements and near the chill roll due to contact problems. To avoid these drawbacks, two-dimensional models have been proposed. Although all of the 2D models in Table 1.2 allow for neck-in, most do not allow for edge beads because they assume that the thickness does not vary across the width of the sheet. All of the 2D studies that incorporate this assumption cite Sergent (1977) as the original source of their model.

Possibly because Sergent's model cannot account for edge beads, it also cannot properly capture the width reduction during stretching. This is demonstrated by Barq et al. (1992) who, based on the model of Sergent, show good agreement with their experimental data except for the width reduction, which they predict as linear but observation shows as curved. D'Halewyu et al. (1990) show that by allowing the thickness to vary across the width, a more realistic width reduction is obtained. Unfortunately, their model does not provide a realistic thickness profile across the width. They obtain an edge bead, but the thickness profile is U-shaped over the centre of the film, instead of being close to uniform as often observed in practice. A U-shaped thickness profile is reproduced in the three-dimensional analysis of Sakaki et al. (1996), except that Sakaki et al. (1996) show a larger neck-in than d'Halewyu et al. (1990). A possible explanation for why films typically have a uniform thickness in the middle has been put forward by Debbaut et al. (1995). Their analysis shows that the U-shaped profile in the centre of the film predicted for a Newtonian fluid is replaced by a constant thickness profile when viscoelasticity is introduced. Christodoulou (1996) also states that increasing the elasticity of the melt results in a more uniform thickness. Furthermore, the explanation that a more uniform thickness is due to elastic effects is supported by Chambon et al. (1996), as they show that when a low elasticity melt is cast, the uniform thickness is lost and a U-shaped profile is obtained. An open question remains concerning how nonisothermal effects influence edge bead formation and neck-in.

Although no nonisothermal model including edge beads appears to have been developed, the thermal effects have been introduced into other models. Thermal effects

are presented in Michaeli and Menges (1982) for extrusion processes, but the effects of stretching in the air are excluded. Another thermal study recognizes the influence of the stretching, but separates its influence from the thermal effects by assuming all of the stretching occurs in the air gap and all of the cooling occurs on the chill roll (Billon et al. 1991). Only a few studies allow for combined thermomechanical effects in the air gap, and all these assume that the mechanical effects on the roll are unimportant. One reason thermal effects have been introduced is to consider crystal growth in the film (Cotto and Haudin 1988; Duffo et al. 1991; Cotto et al. 1989). The crystal growth studies show that the crystallization of the polymer does not begin until contact has been made with the chill roll.

The influence of heat transfer on the velocity and thickness of the film differs considerably, depending on the polymer and the processing conditions simulated. Some studies (Barq et al. 1992; Duffo et al. 1991; Cotto et al. 1989), show only a minor difference between isothermal and nonisothermal results, whereas, for the processing conditions of Alaie and Papanastasiou (1991), the thickness is dramatically changed when heat transfer is introduced. Alaie and Papanastasiou (1991) has the only nonisothermal viscoelastic model proposed to date. Moreover, this study is the only one that uses an integral-type constitutive equation for viscoelasticity.

Several factors are common to all of the papers in Table 1.2. For one, they all use constant value boundary conditions at the die; that is, the velocity, thickness and temperature are assumed constant across the width, which is not always the case in practice. Furthermore, all of the studies, except Barq et al. (1992), assume that inertia,

gravity and sag effects can be neglected. Finally, only a single layer of film is considered in each of these studies. To date, multilayer films have received only limited theoretical study (Park 1991; Pis-Lopez and Co 1996a; Pis-Lopez and Co 1996b).

1.2.2 Solution Techniques

Table 1.3 summarizes the solution techniques corresponding to the simulation studies of Table 1.2. This summary shows that closed-form solutions are rare and only exist for the simplifying assumption that thickness does not vary across the width. Of the numerical techniques used, the finite element method (FEM) is the most popular, as it is used for 4 out of the 8 studies that require numerical solutions. The remaining 4 studies are equally divided between the finite difference method, and Runge-Kutta methods. For the finite element simulations, the algorithm is either step-wise uncoupled or coupled. When the analysis is uncoupled, the velocity, width and thickness are each solved in turn, based on the current values of the other variables. This approach may be slow or it may have convergence problems; therefore, use is often made of coupled algorithms, which solve all of the variables simultaneously in each step. No coupled solution technique has been proposed for two-dimensional nonisothermal simulations.

Table 1.3 Techniques used for Solving the Mathematical Models

Reference	Solution Technique
Avenas et al. (1986)	closed-form solution
Cotto, Duffo and Haudin (1989)	an explicit finite difference method
d'Halewyu, Agassant and Demay (1990)	step-wise uncoupled solution technique: i) the velocity is found using FEM; ii) the width is found using the Newton-Raphson method; and then iii) the thickness is found using the finite volume method.
Duffo, Monasse and Haudin (1991)	an explicit finite difference method
Agassant et al. (1991)	closed-form solution
Alaie and Papanastasiou (1991)	fully coupled Newton-Raphson FEM
Barq et al. (1992)	Runge-Kutta's and Adams-Bashforth's methods (Conte and De Boor 1980: 373-376)
Iyengar and Co (1993)	4^{th} order Runge-Kutta with adaptive step size control
Debbaut et al. (1995)	fully coupled Newton-Raphson mixed FEM
Sakaki et al. (1996)	streamline finite element method

1.2.3 Experimental Data

Little experimental data for film casting appears to have been reported in the literature. For draw resonance, some data has been published (Barq et al. 1990; Bergonzoni and DiCresce 1966), but this data has a periodic variation and cannot be used for calibrating models that simulate behaviour below the critical draw ratio. The most comprehensive set of data is found in Kase (1974) for the temperature and thickness

profiles of steady state PP film casting. Some data is also reproduced in Cotto et al. (1989) and in Duffo et al. (1991) that shows the width and thickness at the roll for different polymers and inlet conditions. Barq et al. (1992) present data for PET casting, but for proprietary reasons their data is in dimensionless form. Chambon et al. (1996) include data for velocity, thickness and width as part of the validation of several film casting models. Finally, experimental data is provided in deGroot et al. (1993). This data examines how changing the fabrication variables affects the ultimate stretch, load retention, cling characteristics, and abuse resistance of the film.

1.3 Purpose and Scope

The purpose of the study reported in this thesis is to investigate film casting using a finite element model. Important requirements were that the model could take into account the following: two-dimensional, nonisothermal behaviour; a viscous constitutive law; gravitational and inertial effects; and the possibility of the formation of edge beads. The effects of die swell, sag and elasticity were neglected. To be able to solve the highly nonlinear system of equations, which contain a strong coupling between velocity and thickness, a Newton-Raphson strategy was adopted. Parametric studies were performed using the finite element model to investigate the influence of heat transfer and self-weight on the velocity, thickness, temperature and width.

This study is original in several respects. First, this is the only model that predicts the thickness variation across the width and simultaneously accommodates nonisothermal effects, gravity and inertia. Second, unlike previous studies, this thesis considers the

influence of nontrivial boundary conditions at the die by allowing the boundary conditions to vary over the width. Third, this study leaves as an open question whether modelling the mechanics of the film is necessary once contact has been made with the chill roll. Finally, this thesis presents an algorithm that uses a tangential stiffness matrix for solving the coupled system of equations. Although not an immediate contribution of this thesis, it is hoped that the model developed here will eventually provide a framework for the addition of a viscoelastic constitutive equation.

The analysis of film casting begins in Chapter 2, with a one-dimensional model of the film casting process. The theoretical model is presented, along with a discussion on the validity of the assumptions used. After that, the solution technique is detailed and tested by comparison to the closed-form solutions that are available. This chapter also includes a parametric study considering the influence of nonisothermal effects and a comparison of the simulated results with the experimental data of Kase (1974). Chapter 3 has the same organization as Chapter 2, except that here the focus is on the development, solution and investigation of a two-dimensional model. Chapter 4 consists of conclusions and recommendations for future work.

Chapter 2 One-Dimensional Model

A one-dimensional (1D) model has several advantages over a two-dimensional (2D) model: a 1D model is simpler to derive and implement than a 2D model; the appropriateness of modelling assumptions can be presented more clearly in one dimension; a 1D model provides a convenient framework for considering the effect of boundary conditions and for doing parametric studies; and a 1D model is often a reasonable representation of wide sheets, and of the central portion of smaller sheets. Once a 1D model has been fully investigated, the analysis can proceed to a 2D model with greater confidence.

This chapter starts with a presentation of the governing equations and boundary conditions for a cast film simulation, including both mechanical and thermal equations and a discussion of the assumptions made in their derivation. Thereafter, the numerical algorithm used to solve the thermomechanical system is described. One aspect of the numerical algorithm described is whether upwinding is necessary for the heat advection term. The following sections present specific numerical simulations, including:

i) comparison to the theoretical isothermal solutions, with and without the effects of self-weight;

ii) investigation of the effects of heat transfer to the chill roll and to the air;

iii) investigation of the influence of the temperature sensitivity of the viscosity; and

iv) comparison of the numerical solution to published experimental data.

The final section in this chapter provides a summary of the results.

2.1 Governing Equations and Boundary Conditions

In this section, the 1D mathematical model for film casting is developed, using the momentum, continuity, constitutive, and conservation of energy equations, together with suitable boundary conditions. Thereafter, the appropriateness of the modelling assumptions is discussed. The presentation of the 1D model is based on the setup shown in Figure 2.1, with the origin of the coordinate system placed at the midpoint between the die lips. By definition, the x_1, x_2 and x_3 axes are in the machine, transverse and out-of-plane directions, respectively. This system can be considered one-dimensional in the x_1-direction if the following conditions hold: the film is thin; extrudate swell is neglected; and the film is either infinite, or constrained, in the transverse direction. Although Figure 2.1 shows a chill roll, a water bath could have been illustrated in its place. Furthermore, the machine direction (x_1) need not be vertical as shown.

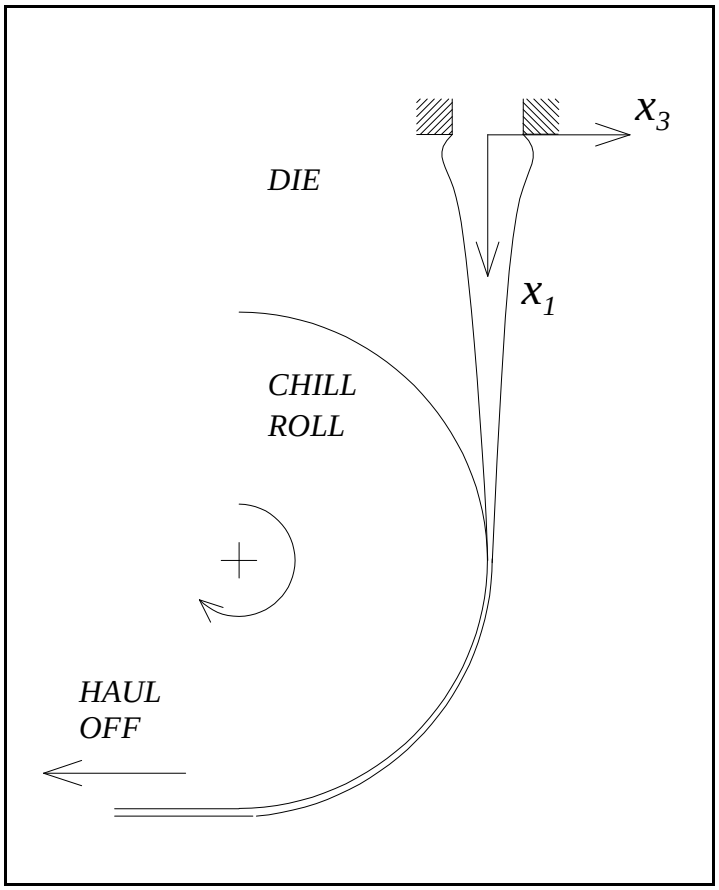

Figure 2.1 Setup for one-dimensional film casting

2.1.1 Mechanical Equations

To find the 1D momentum equation, one can consider the forces applied to a section of film with unit width and infinitesimal length. Figure 2.2 shows the tension and body force applied to the film; air drag and surface tension are neglected as they are assumed small. The tension is the product of thickness (h) and longitudinal stress (σ_{11}), while the body force is the product of density (ρ), acceleration (b), thickness (h) and length (dx_1). Equilibrium requires that the unbalanced force be equal to the change in momentum. In a spatial frame of reference this requirement is expressed as

$$\frac{d(h\sigma_{11})}{dx_1} + \rho bh = \rho h u_1 \frac{du_1}{dx_1} \qquad \textbf{(2.1)}$$

where the inertial term on the right corresponds to the material derivative of velocity in the x_1-direction (u_1), under steady state conditions. When the film is vertical, the acceleration (b) is equal to the acceleration due to gravity (g). The gravity term and the inertial term in Equation 2.1 can be neglected when they are much less than the tensile force. This simplification is discussed further in Section 2.1.3.

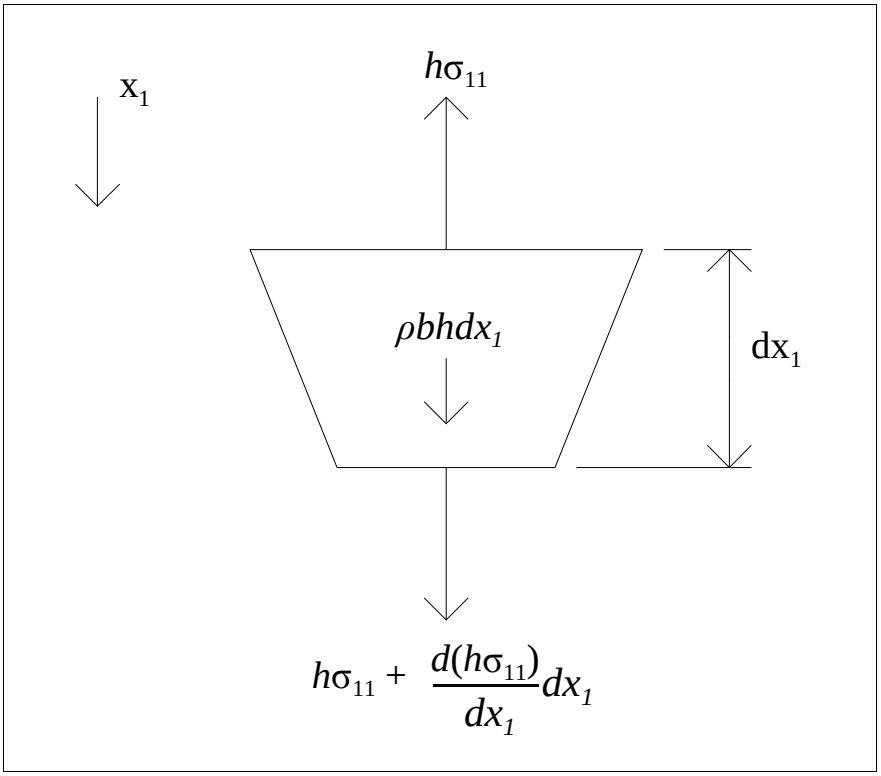

Figure 2.2 Derivation of the 1D momentum equation

A similar approach to that used for deriving the momentum equation can be used to derive the continuity equation. Figure 2.3 shows the mass flux into and out of a

control volume at steady state. For an incompressible fluid these rates are equal; therefore,

$$\frac{d(\rho u_1 h)}{dx_1} = 0 \qquad \textbf{(2.2)}$$

Assuming the density is constant, this equation can be written as

$$\frac{d(u_1 h)}{dx_1} = 0 \qquad \textbf{(2.3)}$$

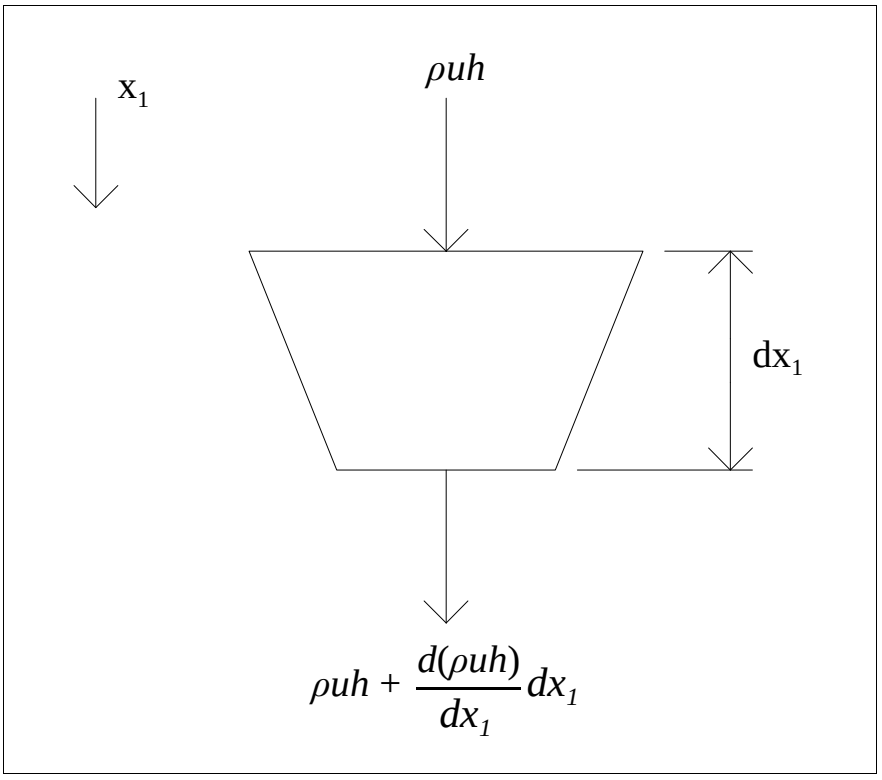

Figure 2.3 Derivation of the 1D continuity equation

The constitutive equation adopted in this research is that for a Newtonian fluid,

$$\sigma_{ij} = -p\delta_{ij} + 2\eta\varepsilon_{ij} \qquad \textbf{(2.4)}$$

where σ_{ij} is the stress tensor, p is the hydrostatic pressure, δ_{ij} is the Kronecker delta, η is the shear viscosity and ε_{ij} is the rate of deformation tensor. For a film, the out-of-plane stress (σ_{33}) is zero, thereby allowing one to relate the hydrostatic pressure to the rate of deformation in the x_3-direction via

$$p = 2\eta \frac{\partial u_3}{\partial x_3} \tag{2.5}$$

where u_3 is the out-of-plane velocity. The pressure (p) can in turn be related to $\partial u_1/\partial x_1$ by using the continuity requirement. Since the rate of change of the velocity in the transverse direction ($\partial u_2/\partial x_2$) is zero for plane strain conditions, continuity requires that

$$\frac{\partial u_3}{\partial x_3} = -\frac{\partial u_1}{\partial x_1} \tag{2.6}$$

Substituting Equations 2.5 and 2.6 into Equation 2.4, allows one to relate the stress in the machine direction to the rate of deformation in that direction; that is,

$$\sigma_{11} = 4\eta \frac{\partial u_1}{\partial x_1} = \eta_p \frac{\partial u_1}{\partial x_1} \tag{2.7}$$

where η_p is by definition the planar elongational viscosity.

Equations 2.1, 2.3, and 2.7 govern the mechanical response of the domain. A solution however, requires specification of the boundary conditions, which are defined in Figure 2.4. The inflow at the die is specified by the velocity and thickness at the die, u_{die} and h_{die}, respectively. For a displacement-controlled setup, the downstream velocity is specified as u_{roll}. This is the velocity at the location where the film is assumed to stick to the roll so that no further deformation is possible. As mentioned in Chapter 1, the ratio of

u_{roll}/u_{die} is defined as the draw ratio (Dr). On the other hand, for a load-controlled problem, the force ($F = h\sigma_{11}$) can be specified at the point where the film sticks to the roll. This sticking is assumed to occur at a distance of L from the die, where

$$L = L_{gap} + L_{roll} \tag{2.8}$$

In this equation L_{gap} is the length in the air gap and L_{roll} is the length along the roll before sticking. This study assumes that there is no friction between the film and the roll prior to the point where the film ceases to deform. The other parameters provided in Figure 2.4 apply to the thermal boundary conditions and heat transfer and are defined in the next section.

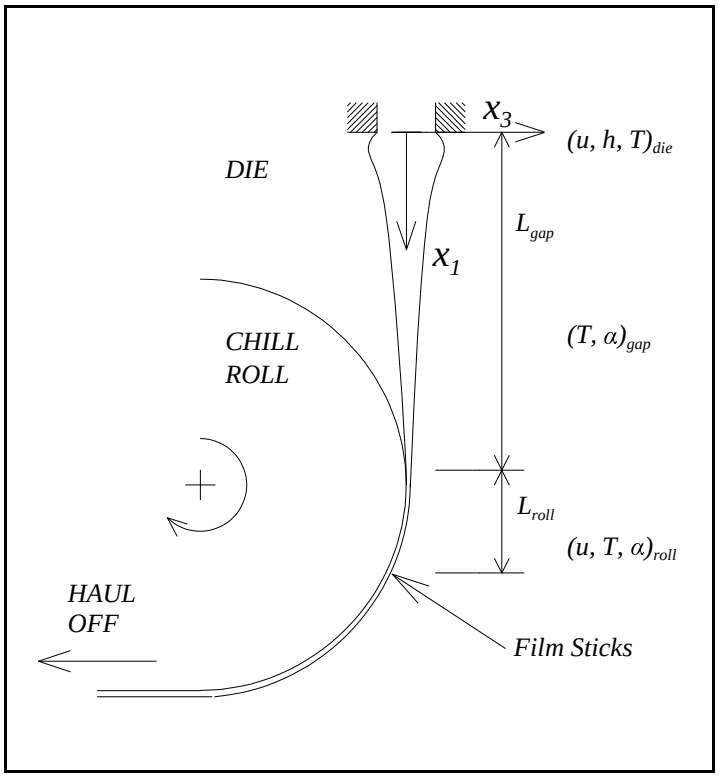

Figure 2.4 Mechanical and thermal boundary conditions and heat transfer characteristics

2.1.2 Heat Transfer Equations

Figure 2.5 shows the heat transfer for a section of film due to conduction, surface cooling and the change in the heat energy stored in the section. At steady state, the change in storage of the heat energy leads to an advective term. Advection is the product of density (ρ), specific heat capacity (C), velocity (u_1) and thickness (h), while conduction (q) follows Fourier's law; that is, $q = -k\frac{dT}{dx_1}$, where k is the thermal conductivity and T is the film temperature. The surface cooling is modelled using Newton's law of cooling, with α being the one-sided heat transfer coefficient and T_{air} the temperature of the surrounding air. If the principle of conservation of energy is applied to this section of film, the following equation results:

$$\rho C u_1 h\frac{dT}{dx_1} + 2\alpha(T - T_{air}) - kh\frac{d^2T}{dx_1^2} = 0 \qquad \textbf{(2.9)}$$

Equation 2.9 does not include a source term for viscous dissipation, as it is assumed negligible for the film casting process.

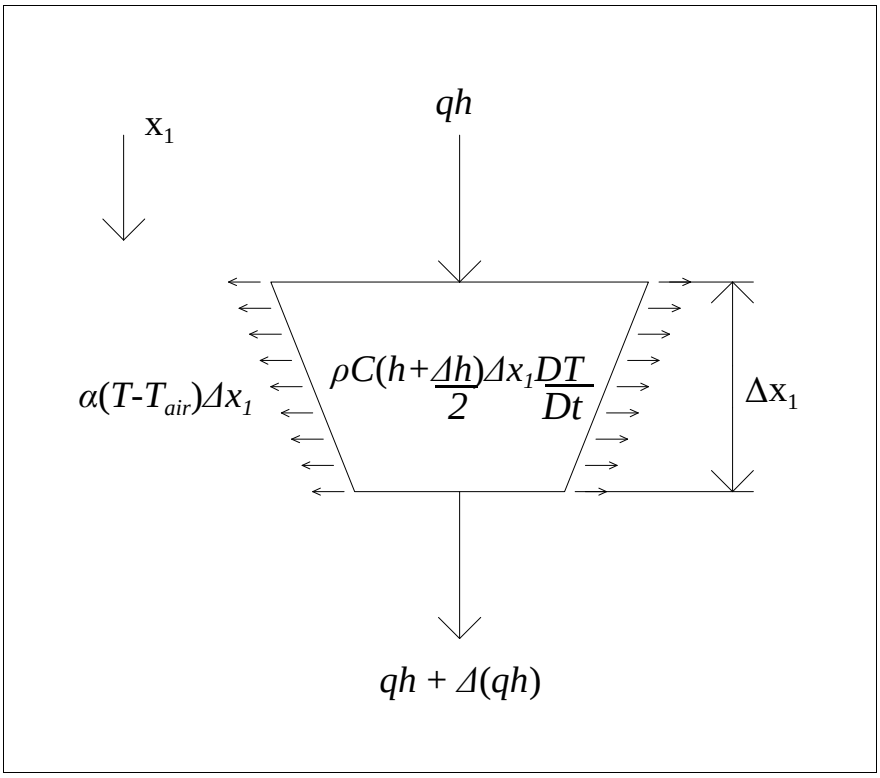

Figure 2.5 Derivation of the 1D conservation of thermal energy equation

An illustration of the thermal boundary conditions and heat transfer coefficients is provided in Figure 2.4. At the die, the temperature is prescribed as T_{die} and over the film's length the heat transfer coefficient (α_{gap} and α_{roll}) and ambient temperatures (T_{gap} and T_{roll}) are specified. The film is divided into two sections, of lengths L_{gap} and L_{roll}, as the heat transfer properties of these two sections differ. Over L_{gap} the heat transfer is to the surrounding air, whereas over L_{roll} the heat transfer is to the chill roll, or water bath. In general, the heat transfer coefficient must take into account free convection, forced convection, and radiation. The heat transfer then, will vary along the length of the film and from one side of it to the other. A detailed analysis of the heat transfer for L_{gap} is

found in Barq et al. (1992) and for L_{roll} in Billon et al. (1991), Cotto et al. (1989) and Duffo et al. (1991). In the current investigation a simple approach is considered adequate; a single heat transfer coefficient and ambient temperature are specified for each section.

Estimation of α_{gap}

To estimate the heat transfer coefficient over L_{gap} the process is considered analogous to forced convection over a flat plate. For this type of heat transfer α_{gap} is found using the following equation (Incropera and DeWitt 1985: 277):

$$\alpha_{gap} = \frac{k_{air} Nu_L}{L_{gap}} \qquad \textbf{(2.10)}$$

where α_{gap} is the average one-sided heat transfer coefficient, k_{air} is the thermal conductivity of the surrounding air and Nu_L is the average Nusselt number. The Nusselt number for laminar forced convection of a fluid over a flat plate is approximated by (Incropera and DeWitt 1985: 318)

$$Nu_L = 0.664 Re_L^{\frac{1}{2}} Pr^{\frac{1}{3}} \qquad For\ Re_L < 5\times10^5\ and\ Pr \geq 0.6 \qquad \textbf{(2.11)}$$

For Equation 2.11 the Reynolds number (Re_L) and the Prandtl number (Pr) have the following definitions:

$$Re_L \equiv \frac{\rho_{air} u_{air} L_{gap}}{\eta_{air}} \qquad and\ Pr \equiv \frac{\nu_{air}}{\kappa_{air}} \qquad \textbf{(2.12)}$$

in which u_{air} is the speed of the forced air relative to that of the plate, L_{gap} is the length of the film in the air gap, ρ_{air} is the density, η_{air} is the absolute viscosity, ν_{air} is the kinematic

viscosity and κ_{air} is the thermal diffusivity. The air properties are estimated for a pressure of one atmosphere (101.3 kPa) and a temperature of $T_f = (T_{air} + T_p)/2$, where T_{air} is the air temperature far from the plate and T_p is the temperature of the plate. For the cast film process, T_p is assumed equal to the temperature at the die (T_{die}). Figure 2.6 summarizes the variables of interest for the calculation of α_{gap}.

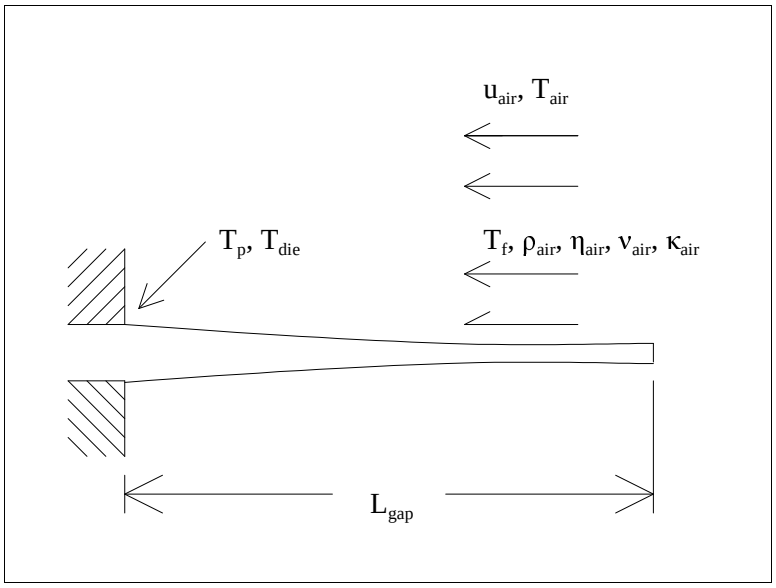

Figure 2.6 Definition of the variables for the calculation of the heat transfer coefficient in the air gap (α_{gap})

Estimation of α_{roll}

Over the chill roll the heat transfer coefficient does not have a simple analogy like that for α_{gap} because of two complications: each side of the film is cooled at a different rate; and the heat transfer characteristics of an air-knife or a vacuum box are difficult to estimate. With a water bath however, a simple analogy can be used; α_{roll} can be estimated using the approach described above for a flat plate, but now the fluid properties are for

water, instead of air. The influence of the heat transfer over L_{roll} is considered further in Section 2.4.1.

Temperature Dependence of Material Properties

Changes in the temperature of the melt result in changes to its material properties. In this analysis, the assumption is that, over the range of temperatures in question, only the viscosity change is significant. An Arrhenius relation is generally a good representation of the temperature dependence of viscosity:

$$\eta = \eta_o e^{\left(\frac{E}{R}\left(\frac{1}{T}-\frac{1}{T_o}\right)\right)} \qquad \textbf{(2.13)}$$

where η_o is the reference viscosity, E is the activation energy, R is the gas constant (8.314 J $mol^{-1} K^{-1}$), T is the temperature and T_o is the reference temperature. This relation has the drawback that the viscosity of the material near the solidification temperature may increase more rapidly than is predicted by Equation 2.13. To address this shortcoming, an alternative viscosity function has been introduced within the context of blown film production (Sidiropoulos 1996):

$$\begin{aligned} \eta(T) &= \eta_o e^{-a(T-T_o)+c\left(\frac{1}{(T-T_s)^d}-\frac{1}{(T_o-T_s)^d}\right)} && \text{when } T > T_s \\ \eta(T) &= \infty && \text{when } T \le T_s \end{aligned} \qquad \textbf{(2.14)}$$

where a, c and d are constant parameters and T_s is the solidification temperature. Both viscosity-temperature relations are used in subsequent simulations.

2.1.3 Discussion of Assumptions

The assumptions made in the above derivations of the governing equations place several physical requirements on the system, including the following: the film is thin; the thickness gradient is small; viscoelasticity can be neglected; a simple thermal model is adequate; and the viscosity is within an appropriate range of values. The appropriate range of viscosity values is determined by the assumptions that viscous dissipation, inertia, self-weight and surface tension can be neglected. This section discusses the physical requirements placed on the system and whether or not they are reasonable for a typical cast film line. To make quantitative statements about the validity of the various assumptions, the behaviour of the 1D, gravity free, isothermal solution is used as a basis for comparison. Appendix A.1 presents the closed-form solution for this case.

i) The Thin Film Requirement

In the derivation of the governing equations the film is considered thin, so that the variables of longitudinal stress (σ_{11}), velocity in the machine direction (u_1), and temperature (T) can be assumed independent of x_3. This assumption is used in the derivations so that the film can be considered in plane stress, and so that the derivations of the equilibrium, continuity and conservation of energy equations are straightforward. The assumption that velocity and stress do not vary over the thickness appears valid, but Pearson (1985: 475) points out that this is not true for the temperature. Pearson shows this by demonstrating that the Graetz number (Gz) is generally too high to consider the temperature constant over the thickness. The Graetz number, which represents the ratio

of thermal conductance due to advection over the length to the thermal conductance due to conduction over the thickness, is defined as

$$Gz = \frac{Q\bar{h}}{\kappa L_{gap}} \qquad \textbf{(2.15)}$$

where Q (= $u_{die}h_{die}$) is the volume flux per unit width, κ is the thermal diffusivity of the polymer and $\bar{h}$ is a characteristic sheet thickness. Figure 2.7 shows a schematic of these variables for film casting. Generally, thickness values are not small enough to compensate for the facts that the polymer melt is a poor thermal conductor and that the processing speeds are relatively high. However, the 1D conservation of energy equation (Eq. 2.9) is still valid if T is considered as the mean temperature ($\bar{T}$):

$$\bar{T}(x_1) = \int_{-\frac{h}{2}}^{\frac{h}{2}} T(x_1, x_3)\,dx_3/h \qquad \textbf{(2.16)}$$

The assumption that the mean temperature is adequate for relating the temperature and viscosity is suggested by Pearson (1985: 475).

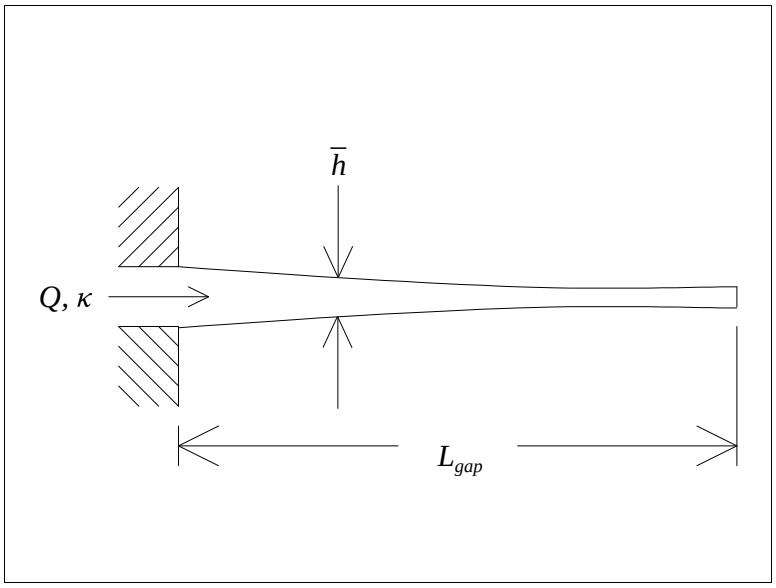

Figure 2.7 Definition of the variables for the calculation of the Graetz number

ii) The Small Thickness Gradient Requirement

In the derivation of governing equations, the implicit assumption that the thickness gradient is small is necessary in two places. First, this requirement is necessary for the plane stress assumption that σ_{33} equals zero. In order for this assumption to be true, the x_3-axis and the normal to the surface have to be the same, which implies that the thickness gradient must be small. Second, the heat transfer from the surface of the film assumes that dh/dx_1 is small. In the derivation of the energy conservation equation (Figure 2.5) the film loses heat over the length Δx_1. This approximation is only valid if the thickness changes very little over the length; that is, if the arc length of the surface of the film can be considered equal to the film's length along the x_1-axis. For the theoretical

isothermal solution (Appendix A.1), the requirement that dh/dx_1 be small is met. This is seen from the solution for the thickness gradient, which is largest at the outlet where $dh/dx_1 = -h_{die}\ln(Dr)/L$. For typical values of $h_{die} = 10^{-3}$ m, Dr = 10 and L = 0.5 m, the value of $dh/dx_1 \approx 5\times10^{-3}$. Although dh/dx_1 is generally small, this is not always the case. Therefore, care should be taken when interpreting the numerical results. The 2D model for example, has sharp corners at the edges and the nonisothermal simulations may show high thickness gradients at the die outlet.

iii) Viscoelasticity

The constitutive equation used in the derivations of Section 2.1.1 assumes a viscous fluid, but often polymers are better represented by a viscoelastic constitutive equation. This thesis uses the simpler viscous model for two reasons. First of all, the main goal of this research is to investigate the influence of nonisothermal effects, and viscoelasticity adds complexity that does not directly contribute to this goal. Secondly, some polymers used in film casting are well represented by a viscous model, such as polyethylene terephthalate (Pearson 1985: 10, 42; Barq et al. 1992).

iv) Simple Heat Transfer Model

Heat transfer in this study is simpler than that actually observed in film casting. The proposed model uses a constant heat transfer coefficient and neglects free convection, radiation and the heat released during solidification. Support for the decision to use a simpler model for heat transfer is found in the fact that even a more rigorous model shows an almost constant heat transfer coefficient in the air gap, except near the die and the roll (Barq et al. 1992). Also, the proposed model can provide a framework for

investigating the influence of nonisothermal effects without necessarily having to provide quantitative predictions. Furthermore, assuming that heat released during solidification can be ignored is valid because solidification occurs on the roll, after the geometry is no longer changing (Cotto et al. 1989; Duffo et al. 1991; Billon et al. 1991). Finally, in recognition that the heat transfer coefficients may not be estimated accurately, a parametric study is presented in Sections 2.4.1 and 2.4.2, to learn the sensitivity of the model to changes in these coefficients.

v) Viscous Dissipation

The assumptions made in deriving the governing equations restrict the admissible range of viscosity values. The upper limit is set by the assumption that viscous dissipation can be neglected, while the lower limit is set by the assumptions that inertia, self-weight and surface tension can be neglected. Once the limits are determined, they can be compared with the limits typically encountered for polymer melts, 10^2 Pa·s $\leq \eta \leq$ 10^5 Pa·s.

To find the viscosity below which viscous dissipation would not make a significant contribution, one can consider the theoretical isothermal solution under typical processing conditions. Viscous dissipation can be neglected if its contribution to the heat transfer in the conservation of energy equation (Eq. 2.9) is much less than that due to advection; that is, if

$$\sigma_{11}\frac{du_1}{dx_1} \ll \rho C u_1 \frac{dT}{dx_1} \qquad \textbf{(2.17)}$$

The constitutive equation (Eq. 2.7) and the theoretical solutions for u_1 and du_1/dx_1 (Appendix A.1) can be substituted into this equation. By recognizing that $(Dr)^{x_1/L}$ is largest for $x_1 = L$ and rearranging, the following relationship is found:

$$\eta \ll \frac{\rho C \frac{dT}{dx_1} L^2}{4 u_{die} Dr (\ln Dr)^2} \tag{2.18}$$

For typical values of $\rho = 900$ kg/m^3, $C = 2000$ J/(kg K), $dT/dx_1 = 100$ K/m, $L = 0.2$ m, $u_{die} = 0.01$ m/s, and $Dr = 10$, the requirement is that $\eta << 3.4\times10^6$ Pa·s. This means that the contribution of viscous dissipation can be considered negligible up to and including the upper limit of typical viscosity values. Even for $\eta = 10^5$ Pa·s the heat transfer by viscous dissipation is only about 3% of that due to advection.

vi) Inertia Term

The lower limit for the value of viscosity is influenced by the assumptions that the inertia term in the momentum equation can be ignored. To find the lower limit associated with neglecting inertia one considers the Reynolds number (Re), which is the ratio of inertial to viscous forces. Reynolds number is defined in Equation 2.12 and can be evaluated for the film. So that the inertia term can be neglected, Re must be less than one; therefore,

$$\eta \gg \rho u_1 L \tag{2.19}$$

where u_1 is a characteristic velocity, which has an upper estimate of u_{roll}. For the typical values defined previously and for $u_1 = u_{roll} = 0.1$ m/s, the viscosity (η) must be much greater than 18 Pa·s. This shows that at the lower limit of viscosity, $\eta = 10^2$ Pa·s, caution

should be used if ignoring the inertial contribution. Therefore, the inertial term is included as an option in the numerical model proposed in this study.

vii) Surface Tension

Another assumption that effects the admissible lower limit of viscosity is that surface tension can be neglected. The capillary number (Cn), which is the ratio of surface tension to viscous forces, is presented in Dobroth and Erwin (1986) in order to figure out the importance of surface tension:

$$Cn = \frac{St}{\eta \bar{h}} \ll 1 \qquad \textbf{(2.20)}$$

where S is the surface energy per unit area, and t is the processing time, which is considered as the time spent in the air gap. These variables are summarized for film casting in Figure 2.8. Equation 2.20 implies that

$$\eta \gg \frac{St}{\bar{h}} \qquad \textbf{(2.21)}$$

Sample numbers that provide a maximum estimate for the right-hand side of this equation are provided in Dobroth and Erwin (1986): $\bar{h}$ = 0.001 m, t = 10 s and S = 0.035 N/m. The result is that $\eta >> 350$ Pa·s. This suggests that the lower limit of typical viscosity values (10^2 Pa·s) must include surface tension effects when the processing time is greater than 10 s. However, the processing time is usually much shorter than this, so generally surface tension can be neglected.

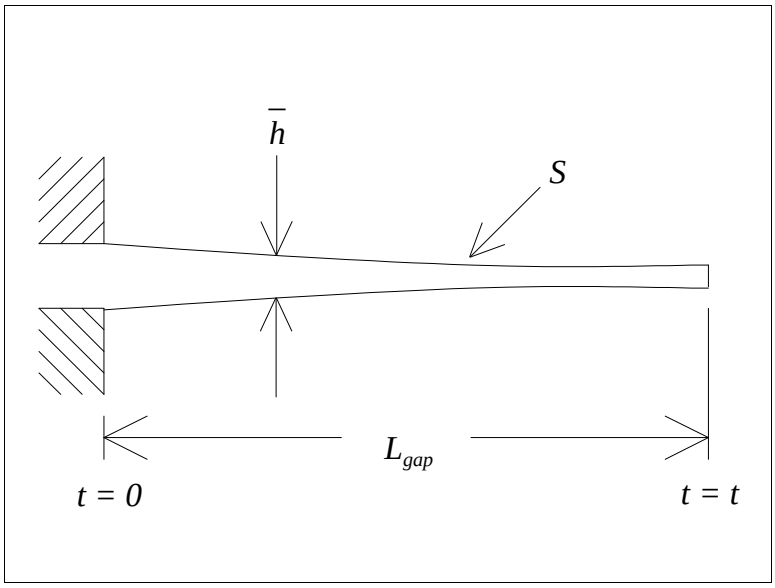

Figure 2.8 Definition of the variables for the calculation of the Capillary number (Cn)

viii) Self-Weight

Finally, the assumption that the self-weight can be ignored also places a lower limit on the viscosity value. The self-weight can be ignored if it is much less than the tension applied to the film. For a vertical film the weight is greatest at the die. To find an approximate weight, the theoretical weightless solution for thickness is substituted into an expression for the differential weight ($dW = \rho g h dx_1$) and integrated over the length to yield:

$$W = \frac{\rho g h_{die} L (Dr - 1)}{Dr \ln(Dr)} \qquad \textbf{(2.22)}$$

To relate the tension (F) to the viscosity, the constitutive equation and the theoretical solution for h are substituted into the tension equation ($F = h\sigma_{11}$) to find:

$$F = 4\eta h_{die} u_{die} \ln(Dr)/L \qquad \textbf{(2.23)}$$

If the self-weight can be neglected then W << F. Using this condition with Equations 2.22 and 2.23, the lower limit required for viscosity can be expressed as

$$\eta \gg \frac{\rho g L^2 (Dr - 1)}{4 u_{die} Dr (\ln Dr)^2} \qquad \textbf{(2.24)}$$

Typical values of $\rho = 900$ kg/m^3, $g = 9.81$ m/s^2, $L = 0.2$ m, $Dr = 10$ and $u_{die} = 0.01$ m/s, require that $\eta >> 1.5 \times 10^3$ Pa·s. This means that, for viscosity values less than approximately 10^4 Pa·s, the self-weight of the film can make a contribution. Consequently, self-weight is included as an option in the current model of polymer film casting.

A summary of how the above assumptions relate to viscosity is provided in Figure 2.9, along with the typical viscosity range.

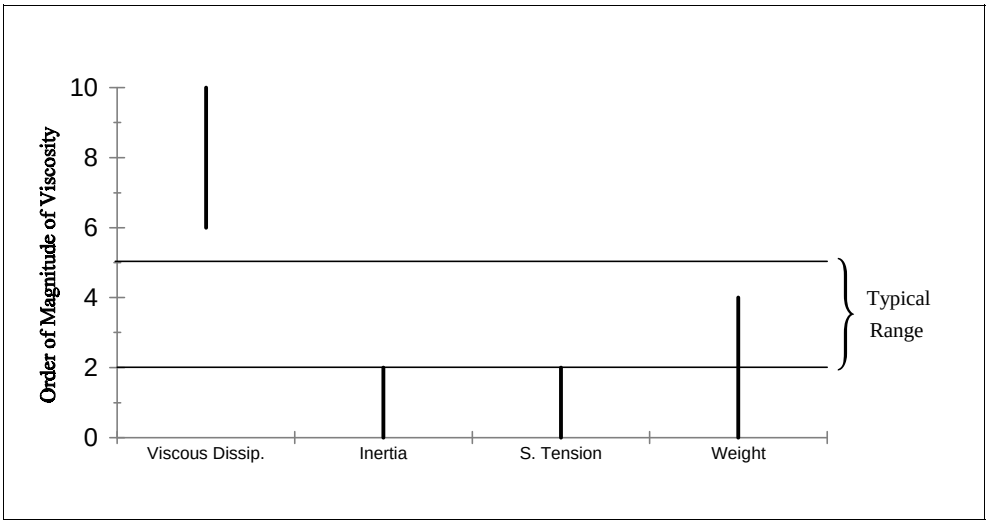

Figure 2.9 Ranges of viscosity values for which viscous dissipation, inertia, surface tension and self-weight may have to be included in the mathematical model of film casting

2.2 Solution of the Coupled System

The goal of this analysis is to find the velocity, thickness and temperature distributions. To find these variables a coupled algorithm was developed that solves the governing equation simultaneously, as opposed to an uncoupled algorithm, which solves each equation in a stepwise manner. A coupled approach has the advantage of more rapid convergence. Moreover, the solution provided by a coupled algorithm does not depend on the order the equations are solved in, which is a potential pitfall for uncoupled algorithms.

2.2.1 Finite Element Equations

The solution of the thermomechanical system by the finite element method first involves expressing the governing differential equations in their equivalent integral form. For the equilibrium equation (Eq. 2.1), this is done by multiplying by a virtual velocity (δu_1) and integrating over the length to obtain

$$\int_0^L \delta u_1 \left(\frac{d(h\sigma_{11})}{dx_1} + \rho g h - \rho h u_1 \frac{du_1}{dx_1} \right) dx_1 = 0 \qquad \textbf{(2.25)}$$

After integrating by parts, this equation can be modified to express the weak form of equilibrium,

$$\int_0^L \delta \varepsilon_{11} h \sigma_{11} dx_1 + \int_0^L \delta u_1 \rho h u_1 \frac{du_1}{dx_1} dx_1 = \int_0^L \delta u_1 \rho g h dx_1 + \delta u_1 h \sigma_{11} \Big|_0^L \qquad \textbf{(2.26)}$$

where $\delta\varepsilon_{11}$ is the virtual rate of deformation in the machine direction that is consistent with the virtual velocity δu_1. These integrations are carried out for a unit width and the product $h\sigma_{11} = F$ is the force applied at the roll. When solving boundary value problems,

either the force (F) or the velocity (u_1) is specified at the boundary, but not both simultaneously.

The integral form of the continuity equation (Eq. 2.3) involves multiplication by a weighting function (δh) and integrating over the length to yield:

$$\int_0^L \delta h \left(u_1 \frac{dh}{dx_1} + \frac{du_1}{dx_1} h \right) dx_1 = 0 \qquad \textbf{(2.27)}$$

Finally, the integral of the conservation of energy equation multiplied by a virtual temperature (δT) is

$$\int_0^L \delta T \left(\rho C u_1 h \frac{dT}{dx_1} - hk \frac{d^2T}{dx_1^2} + 2\alpha (T - T_{air}) \right) dx_1 = 0 \qquad \textbf{(2.28)}$$

which after integration by parts results in the following:

$$\int_0^L \delta T \rho C u_1 h \frac{dT}{dx_1} dx_1 - \delta T h k \frac{dT}{dx_1} \Big|_0^L + \int_0^L \frac{d\delta T}{dx_1} hk \frac{dT}{dx_1} dx_1 + \int_0^L \delta T \cdot 2\alpha (T - T_{air}) dx_1 = 0 \qquad \textbf{(2.29)}$$

Although T is known at the upstream boundary ($x_1 = 0$), it is not known at the downstream boundary ($x_1 = L$), as this boundary is artificial and the physics of heat transfer are unknown here a priori. The approach used in this analysis is to specify a natural boundary condition of $q = 0$ at $x_1 = L$, for two reasons. First, specifying that the heat flux due to conduction is zero is a good approximation of the conductive flux for polymers, which have very low thermal conductivity. Second, specifying a zero boundary flux at synthetic boundaries has often shown success (Papanastasiou et al. 1992). With the boundary terms removed the equation is

$$\int_0^L \delta T \rho C u_1 h \frac{dT}{dx_1} dx_1 + \int_0^L \frac{d\delta T}{dx_1} hk \frac{dT}{dx_1} dx_1 + \int_0^L \delta T \cdot 2\alpha T dx_1 = \int_0^L \delta T \cdot 2\alpha T_{air} dx_1 \tag{2.30}$$

With the governing equations expressed in an integral form, a finite element discretization can be introduced. The discretization for a n-noded, one-dimensional element is

$$\begin{pmatrix} u_1 \\ h \\ T \end{pmatrix} = \mathbf{Na} = \begin{bmatrix} N_1 & 0 & 0 & \cdots & N_n & 0 & 0 \\ 0 & N_1 & 0 & \cdots & 0 & N_n & 0 \\ 0 & 0 & N_1 & \cdots & 0 & 0 & N_n \end{bmatrix} \begin{pmatrix} u_1 \\ h_1 \\ T_1 \\ \vdots \\ u_n \\ h_n \\ T_n \end{pmatrix} \tag{2.31}$$

in which **N** is the shape function matrix, **a** is the degree of freedom vector, and u_i, h_i, T_i and N_i are the velocity, thickness, temperature and shape function values corresponding to node i. Some researchers have suggested that the order of interpolation of thickness should be one order less than that for velocity, in an analogy with the pressure field in a mixed formulation (Debbaut et al. 1995). This is not a direct analogy however, as the thickness in the continuity equation (Eq. 2.3), unlike the pressure, depends on the velocity as well as the gradient of the velocity.

The above discretization (Eq. 2.31) can be substituted into the field equations (Eqs. 2.26, 2.27 and 2.30), along with the constitutive law (Eq. 2.7), to yield the following finite element equations:

$$\begin{pmatrix} \mathbf{K}_{eqlb} \\ \mathbf{K}_{cont} \\ \mathbf{K}_{thrm} \end{pmatrix} \mathbf{a} = \begin{pmatrix} \mathbf{R}_{eqlb} \\ 0 \\ \mathbf{R}_{thrm} \end{pmatrix} \qquad \textbf{(2.32)}$$

$$\text{where,} \quad \begin{aligned} \mathbf{K}_{eqlb} &= \mathbf{K}_{grad} + \mathbf{K}_{inrt} \\ \mathbf{K}_{thrm} &= \mathbf{K}_{advt} + \mathbf{K}_{cond} + \mathbf{K}_{newt} \end{aligned}$$

in which $\mathbf{K}_{eqlb}$, $\mathbf{K}_{cont}$ and $\mathbf{K}_{thrm}$ are the stiffness matrices for equilibrium, continuity and the conservation of thermal energy; $\mathbf{K}_{grad}$ and $\mathbf{K}_{inrt}$ are the contributions to $\mathbf{K}_{eqlb}$ from the gradient of stress and from inertia; $\mathbf{K}_{advt}$, $\mathbf{K}_{cond}$ and $\mathbf{K}_{newt}$ refer to the contributions to $\mathbf{K}_{thrm}$ from advection, conduction and Newton's law of cooling; and $\mathbf{R}_{eqlb}$ and $\mathbf{R}_{thrm}$ are the load vectors for equilibrium and thermal energy. In these equations the stiffness matrices and $\mathbf{R}_{eqlb}$ are functions of the degree of freedom vector **a**. The stiffness matrices and load vectors are presented in full in Appendix B.1.

2.2.2 Derivation of the Tangential Stiffness Matrix

To solve the coupled system using the Newton-Raphson method, the notion of the residual vector ($\boldsymbol{\psi}$) is introduced, where

$$\boldsymbol{\psi} \equiv [\mathbf{K}_{eqlb} + \mathbf{K}_{cont} + \mathbf{K}_{thrm}]\cdot\mathbf{a} - \mathbf{R}_{eqlb} - \mathbf{R}_{thrm} \qquad \textbf{(2.33)}$$

For equilibrium $\boldsymbol{\psi} = \mathbf{0}$. In this equation the stiffness matrices, load vectors and the solution vector (**a**) are applied to the entire system, as opposed to a single element. The residual can be approximated using a first order Taylor's expansion about any nearby nonequilibrium solution $\mathbf{a}_n$,

$$\boldsymbol{\psi}(\mathbf{a}_{n+1}) = \boldsymbol{\psi}(\mathbf{a}_n) + \frac{d\boldsymbol{\psi}(\mathbf{a}_n)}{d\mathbf{a}_n}\Delta\mathbf{a}_n = \mathbf{0} \qquad \text{where } \mathbf{a}_{n+1} = \mathbf{a}_n + \Delta\mathbf{a}_n \qquad \textbf{(2.34)}$$

The tangential stiffness matrix ($\mathbf{K}_T$) is the derivative of the components of the residual load vector with respect to the degrees of freedom,

$$\boldsymbol{K}_T(\boldsymbol{a}) \equiv \frac{d\boldsymbol{\psi}}{d\boldsymbol{a}} \tag{2.35}$$

Appendix B.1 explains how the tangential stiffness matrix was calculated.

Once the global tangential stiffness matrix is found the change in the variables is determined by solving

$$\boldsymbol{K}_T^n \Delta\boldsymbol{a}_n = -\boldsymbol{\psi}(\boldsymbol{a}_n) \tag{2.36}$$

A new approximation to the solution vector is calculated by adding $\Delta\mathbf{a}_n$ to $\mathbf{a}_n$. This process continues until the relative change in the variables is less than some prescribed tolerance. The stopping criterion used for this study was,

$$Max\left(\frac{\|\Delta\boldsymbol{u}\|}{\|\boldsymbol{u}\|}, \frac{\|\Delta\boldsymbol{h}\|}{\|\boldsymbol{h}\|}, \frac{\|\Delta\boldsymbol{T}\|}{\|\boldsymbol{T}\|}\right) \le Tolerance, \quad where\ \|\boldsymbol{u}\| = \sqrt{\boldsymbol{u}\boldsymbol{u}^T}\ etc. \tag{2.37}$$

in which **u**, **h** and **T** are the current solutions found in **a** for velocity, thickness and temperature, while $\Delta\mathbf{u}$, $\Delta\mathbf{h}$, and $\Delta\mathbf{T}$ are the changes to these variables contained in $\Delta\mathbf{a}$. Unless stated otherwise, the tolerance used in the 1D study was 0.001.

For the Newton-Raphson method, convergence depends on a good initial estimate of the solution. Based on experience from the problems studied in this thesis a good initial guess for the velocity and thickness are their theoretical isothermal solutions, which are provided in Appendix A.1. A linear profile proved to be a good estimate for the temperature. Even with good initial estimates, the algorithm was found not to converge if the heat transfer coefficient was too high. In this case, the final solution was

found through progressively incrementing the heat transfer coefficient until it reached its full value.

2.2.3 Upwinding Finite Elements

Although the other stiffness matrices defined in section 2.2.1 can be evaluated using standard Gauss quadrature, caution is required when evaluating the advection stiffness matrix ($\mathbf{K}_{advt}$) in this manner. For heat transfer problems in which advection dominates, the standard Galerkin method can lead to spurious oscillations in the solution (Christies et al. 1976). One indication of whether this may be a problem is how large advection is relative to conduction, which is represented by the Peclet number (Pe),

$$Pe = \frac{u_1 L_{gap}}{\kappa} \qquad where\ \kappa = \frac{k}{\rho C} \tag{2.38}$$

Pe is smallest at the die, where typical values of the parameters are: u_{die} = 0.01 m/s, L_{gap} = 0.5 m, k = 0.2 W/(m K), ρ = 900 kg/m^3, and C = 2000 J/(kg K). For these values Pe is 4.5×10^4, which shows the importance of advection relative to conduction and that the standard Galerkin method could potentially cause problems. When advection dominates upwind finite element schemes can be used to alleviate the difficulties.

An Upwind Finite Element Scheme

Several approaches are available for 1D upwind finite elements, but one of the simplest is presented by Hughes (1979). In his method upwinding is accomplished for a 1D element by evaluating the advection stiffness matrix as

$$\boldsymbol{K}_{advt} = \rho C u_1(O^e) h(O^e) \boldsymbol{N}_T^T(\xi) \boldsymbol{B}_T(\xi) J(O^e) \overline{W} \tag{2.39}$$

where ξ is the optimum integration point, O^e is the origin of the isoparametric coordinates for the element, J is the determinant of the Jacobian of the isoparametric transformation and $\overline{W}$ is the weight factor, which is 2 for 1D problems. The optimum integration point (ξ) is defined as

$$\xi = \coth\left(\frac{Pe}{2}\right) - \frac{2}{Pe} \qquad \textbf{(2.40)}$$

Neglecting Upwinding for the Thermal Analysis of Film Casting

Upwinding was found unnecessary for the numerical simulation of the temperature distribution in a film, even though the Peclet number is high. The reason for this is that the proposed model circumvents the usual cause of trouble, which is unnaturally forcing an essentially 1D equation to satisfy two extreme boundary conditions. In Equation 2.9 the advection term is 1D and dominates the behaviour, but this equation is required to satisfy not one but two boundary conditions because of the conduction term. However, the thermal boundary conditions proposed in Section 2.2.1 have only one extreme boundary condition. The condition for zero thermal flux at the die does not place any extreme requirements on the solution. Therefore, the boundary conditions are in keeping with the essentially 1D nature of the governing equation and the source of trouble is bypassed.

As suggested by the previous paragraph, upwinding is generally required when two thermal boundary conditions are fixed. This is shown by considering the heat transfer in a sheet moving with a constant velocity, with the temperature specified at x = 0 and x = L. Carslaw and Jaeger (1959: 148) derived the closed-form solution for this

problem, which is reproduced in Appendix A.2. The parameters used were k = 0.2 W/(m K), ρ = 900 kg/m^3, C = 2000 J/(kg K), u_1 = 0.01 m/s, h = 0.001 m, L = 0.5 m, α = 2.0 W/(m^2 K), T_{air} = 0.0 °C, T_{die} = 180 °C, and T_{roll} = 100 °C. A comparison of the theoretical solution and the numerical solutions with and without upwinding (Figure 2.10) shows that upwinding is essential here. The upwinding solution has less than a 0.13 % relative error, while the standard Galerkin solution has a relative error exceeding 479 %, in addition to spurious oscillations.

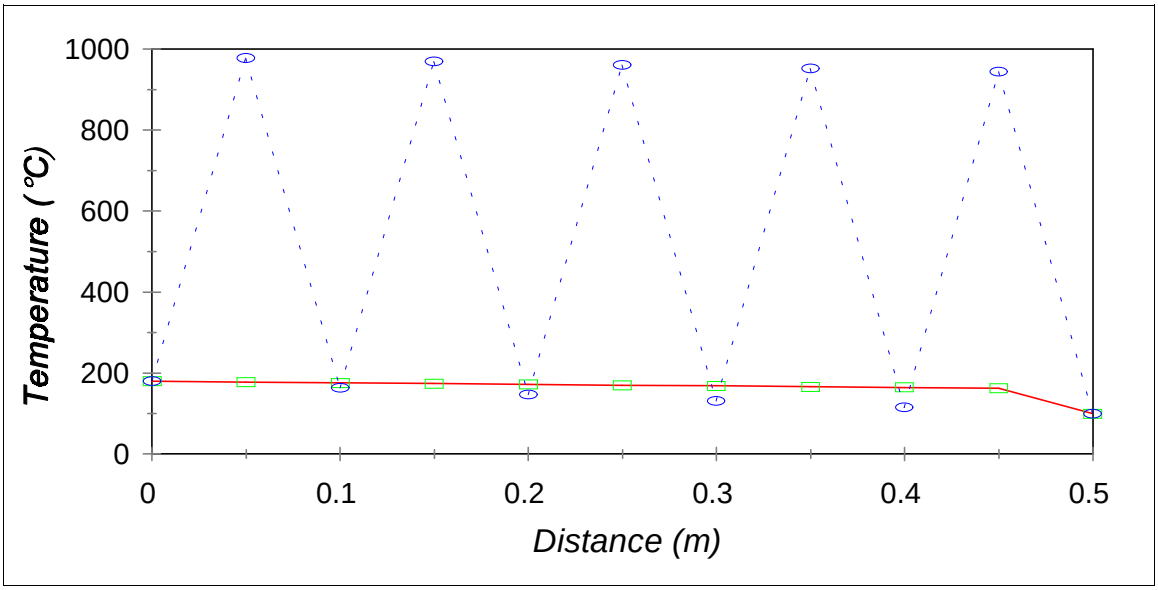

Figure 2.10 Temperature distributions for fixed boundary conditions at the die and at the roll for theory (–), upwinding (□) and no upwinding (--○--)

Film casting however, does not use a boundary condition at the roll like that of the previous example. In film casting, there is a zero thermal flux condition at the die, which allows the standard Galerkin method to make satisfactory temperature predictions. The theoretical solution used to illustrate this is that for a sheet with an infinite length in the machine direction. Carslaw and Jaeger (1959: 148) derive a closed-form solution for this

case, which is reproduced in Appendix A.2. Figure 2.11 shows the theoretical and numerical results over the first 0.5 m of the infinite length, using the same parameters as above, except that T_{roll} is no longer specified. These results show that the standard Galerkin method performs slightly better than the upwind finite elements (0.608 % maximum relative error versus 0.612%). In conclusion then, upwinding is not considered necessary for the heat transfer in the film casting problem.

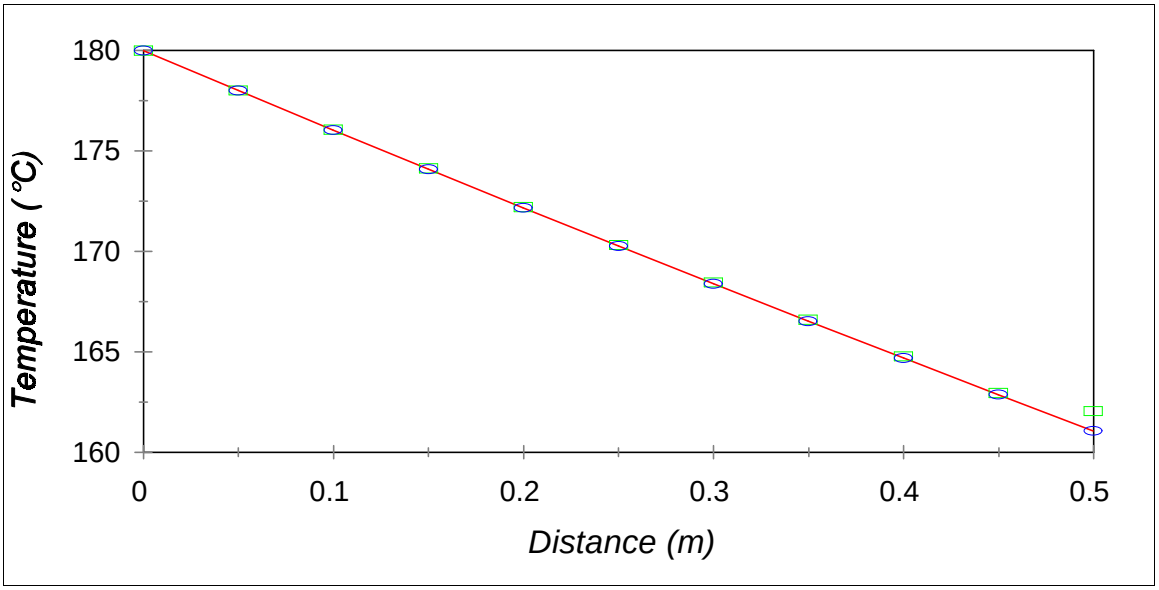

Figure 2.11 Temperature profiles for an infinite sheet for the theoretical (–), upwind (□) and standard Galerkin (○) solutions.

Upwinding for the Continuity Equation

Debbaut et al. (1995) use upwinding for the continuity equation (Eq. 2.3), but this was not considered necessary in this study. Upwinding is not included because the coefficients for the different order derivatives of velocity are approximately the same in the continuity equation. The coefficients for u_1 and du_1/dx_1, which are dh/dx_1 and h, respectively, have similar magnitudes.

2.3 Isothermal Simulations

Before investigating the effects of allowing the temperature to vary, the finite element program was tested against two closed-form isothermal solutions. One solution is for film casting, neglecting gravity and inertia, and the other is for a film falling under its own weight and includes gravity and inertia. These two different cases, along with other simulations, provide a basis for considering the influence of gravity and inertia on isothermal film casting.

2.3.1 Comparison to the Theoretical Isothermal Solution

The closed-form solution for 1D isothermal film casting, which assumes that the polymer's self-weight and inertia can be ignored, is derived in Baird and Collias (1995) and is reproduced in Appendix A.1. A comparison of the closed-form and numerical solutions for the dimensionless velocity and thickness (Figure 2.12), shows that the numerical solution is in excellent agreement with the closed-form solution. The maximum relative error for the velocity is 0.005 % and for the thickness is 0.1%. For the simulation 30 elements were used and the input data were as follows: u_{die} = 0.01 m/s, h_{die} = 0.001 m, Dr = 10, $\eta = 1.6\times10^5$ Pa·s, and L = 0.3 m. In the case of 15 elements the maximum relative errors increased to 0.01% and 1.7% for the velocity and thickness distributions, respectively.

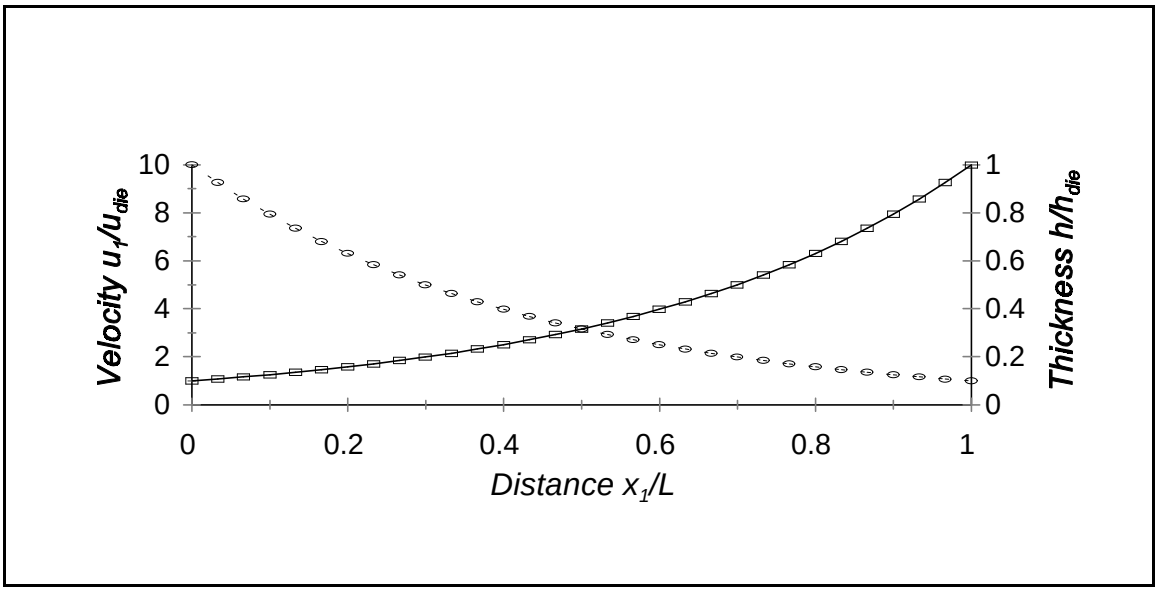

Figure 2.12 Isothermal drawn film solutions for the theoretical velocity (–) and thickness (···) and the numerical velocity (□) and thickness (○)

2.3.2 The Influence of the Film's Self Weight

A closed-form solution is also available for a sheet of viscous fluid falling vertically under its own weight. For this case, the self-weight is included because it drives the solution. Inertia is also included as Reynolds number is no longer small because in the following simulation a low viscosity and a large length were used. The closed-form solution, derived in Clarke (1966), is given in Appendix A.5. Clarke's solution is for $u_{die} = 0$, which is an impossible boundary condition for the numerical algorithm, since if $u_{die} = 0$ then u_1 is zero for all x_1, because continuity requires that $hu_1 = h_{die}u_{die}$. As a result, the numerical algorithm was started from a point where the velocity is known from the closed-form solution. For the initial guess, the velocity profile for a free falling body was used, $u_1 = \sqrt{2gx_1 + u_{die}^2}$. The input parameters were $\eta = 10^2$ Pa·s, ρ

= 900 kg/m^3, L_{gap} = 13.5 m and h_{die} = 0.001m. The numerical solution used 30 elements and u_{die} = 2.542 m/s at x_1 = 0.836 m. As shown in Figure 2.13, the numerical results are in excellent agreement with the theory. If the number of elements is decreased to 15 then essentially the same solution is found. The plot uses the dimensionless variables (U and X) defined in Brown (1961).

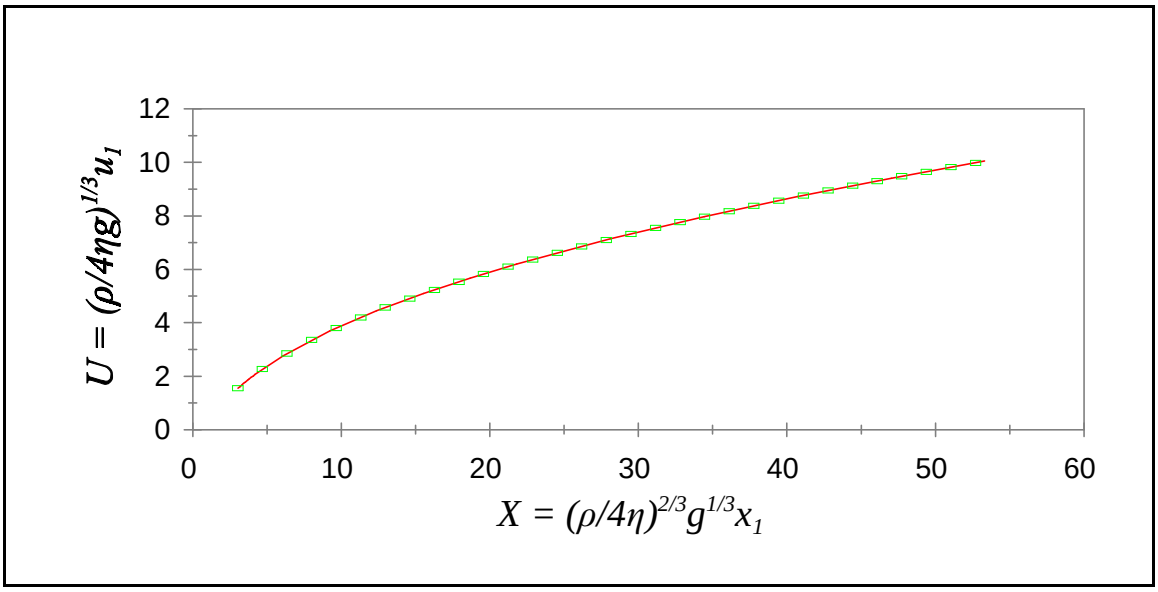

Figure 2.13 Curtain velocity versus distance for theory (–) and numerical simulation (□)

In film casting the effect of the self-weight of the polymer can be seen by increasing its influence with an associated decrease in the viscosity. Figure 2.14 shows how the velocity profile changes for a vertical film casting line as the viscosity decreases by factors of 10. The results agree with the assumption that the self-weight and inertia are not important for large viscosity values. For $\eta \geq 10^4$ Pa·s the solution is essentially identical to the theoretical solution neglecting self-weight and inertia, which does not depend on viscosity. For $\eta \leq 10^3$ Pa·s though, the self-weight has a notable influence. As

the viscosity decreases the self-weight of the polymer leads to a more rapidly increasing velocity (and associated decreasing thickness).

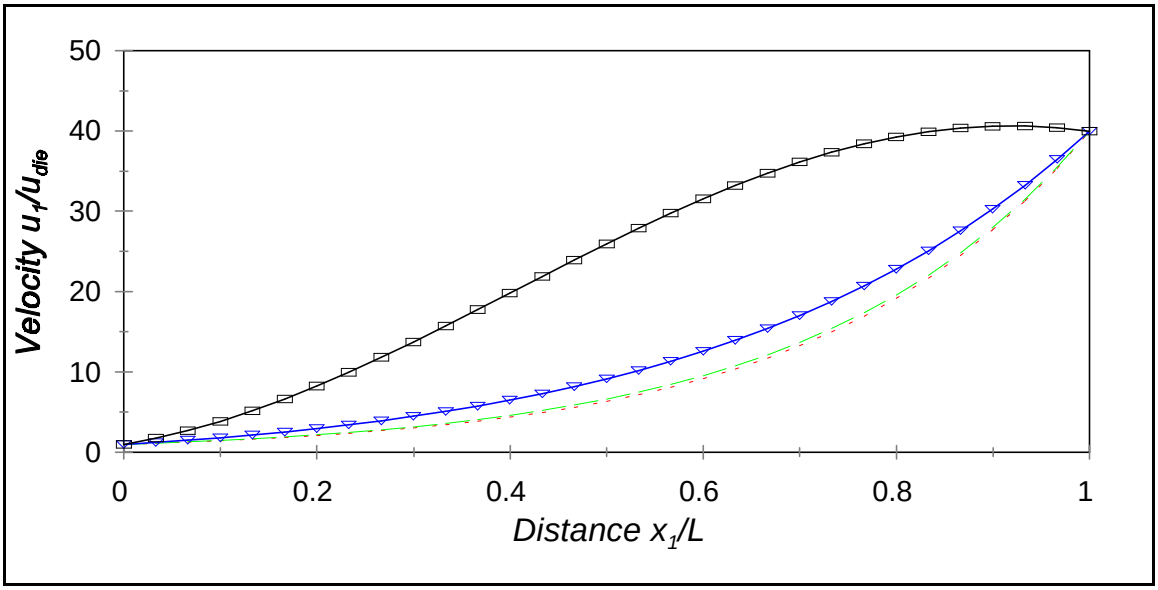

Figure 2.14 Velocity profiles for the cast film process with η values in Pa·s of 10^2 (□), 10^3 (▽), 10^4(---) and 10^5(·····)

2.4 Performance of the Nonisothermal Model

The previous section tested the numerical solution for the isothermal model. The next step, is to combine the mechanical and thermal models to see how they interact. This section investigates this interaction by varying the thermal parameters that are difficult to estimate; that is, heat transfer to the chill roll, heat transfer to the air, and the temperature dependence of the viscosity.

So that the simulations in this section could be compared with one another, they were all completed with the same grid, polymer, and processing conditions. The grid consisted of 30 elements and the polymer was LDPE (low density polyethylene), for

which ρ = 920 kg/m^3, k = 0.24 W/(m K), and C = 2300 J/(kg K) (Rauwendaal 1986: 218). For LDPE, the temperature dependence of the viscosity can be represented using Equation 2.14, with the following parameters: $\eta_o = 1.6\times10^5$ Pa·s, T_o = 180 °C, T_s = 95 °C, a = 0.214, c = 5.75 and d = 1.0 (Sidiropoulos 1995). Owing to the large viscosity, the effects of self-weight and inertia were neglected. For the simulations in this section, the processing conditions were defined as shown in Figure 2.15. This figure includes the heat transfer coefficients, which are derived in the following paragraphs.

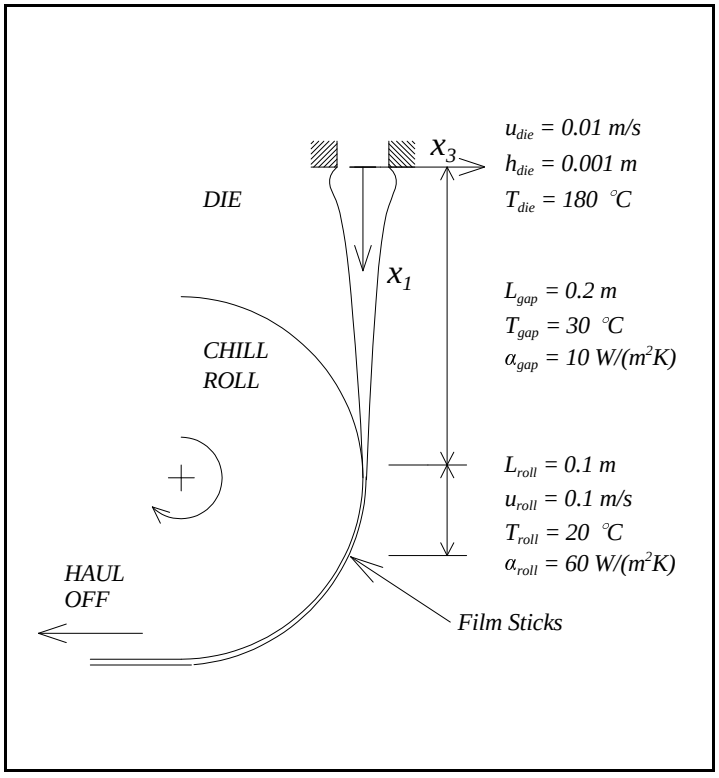

Figure 2.15 Processing conditions used as a basis of comparison in the parametric study of heat transfer

A reasonable value for α_{gap} can be found using the approach outlined in Section 2.1.2. If T_{air} is assumed as 30 °C then T_f = 105 °C and the air properties at a pressure of

one atmosphere are $k_{air} = 25\times10^{-3}$ W/(m K), $\eta_{air} = 18\times10^{-6}$ Pa·s, $\rho_{air} = 13\times10^{-1}$ kg/m^3 and Pr = 0.76 (Avenas et al. cited in Barq et al. 1992). For these data and a relative air speed of $u_{air} = 1.2$ m/s, Equations 2.10, 2.11 and 2.12 predict a heat transfer coefficient of approximately 10 W/(m^2 K). This value agrees with Michaeli and Menges (1982) and is of the same order of magnitude as those used by Barq et al. (1992), Cotto et al. (1989) and Duffo et al. (1991).

As explained in Section 2.1.2, α_{roll} is difficult to obtain from the theoretical equations of heat transfer. However, it is possible to provide a reasonable estimate, from the knowledge that the film freezes during contact with the chill roll. To take advantage of this knowledge use is made of an equation that is derived in the next section, Equation 2.41.

Equation 2.41, relates the temperature of the film to the heat transfer coefficient. For the polymer and processing conditions described above, this equation estimates $T(L_{gap}) \approx 154$ °C. Assuming that, over the length L_{roll}, the film's temperature drops from 154 °C to the solidification temperature, Equation 2.41 requires that $\alpha_{roll} \approx 60$ W/(m^2 K). This value likely underestimates the heat transfer coefficient because films often freeze over a distance shorter than L_{roll}.

If the alternative method of using a water bath were employed then the cooling would occur at a higher rate. With a water bath, the approach used for α_{gap} can be used, with water as the fluid instead of air. If T_{air} is assumed as 20 °C and T_p is assumed as 154 °C, then $T_f \approx 90$ °C. The water properties at T_f and a pressure of one atmosphere are as follows: $k_{water} = 0.67$ W/(m K), $\eta_{water} = 3.16\times10^{-4}$ Pa·s, $\rho_{water} = 965.3$ kg/m^3 and Pr = 1.98

(Bejan 1984: 462). If these values are substituted into Equations 2.10, 2.11 and 2.12, along with $u_{air} = u_{roll,}$ then the value of α_{roll} is about 990 W/(m^2 K).

In the simulations that follow, the value of 60 W/(m^2 K) is used as the basis for comparison. This value likely represents a conservative estimate for α_{roll}.

2.4.1 Effect of Heat Transfer to the Chill Roll

Over the air gap, the thermal response does not depend on the heat transfer at the roll. Although the chill roll rapidly cools the film, the poor thermal conductivity of the polymer means that this affects the upstream temperature very little. Temperature profiles for α_{roll} values of 30, 60, 90 and 120 W/(m^2 K), which are shown in Figure 2.16, have a maximum relative difference of only 0.1% in the air gap. The temperature profiles of Figure 2.16 consist of two distinct, approximately linear, segments. This figure also shows the temperature values predicted by solving the energy conservation equation neglecting conduction,

$$T = (T_{die} - T_{air})e^{\frac{-2\alpha}{\rho C u_1 h}x_1} + T_{air} \qquad \textbf{(2.41)}$$

This equation is derived in Appendix A.3. A solution for temperature can be found independent of the velocity and thickness profiles, because the solution depends only on the product of velocity and thickness, which is constant. Values from Equation 2.41 are in excellent agreement with the numerical predictions, with a maximum relative difference of only 0.1% between them. Clearly, the effects of thermal conductivity of the polymer can be ignored.

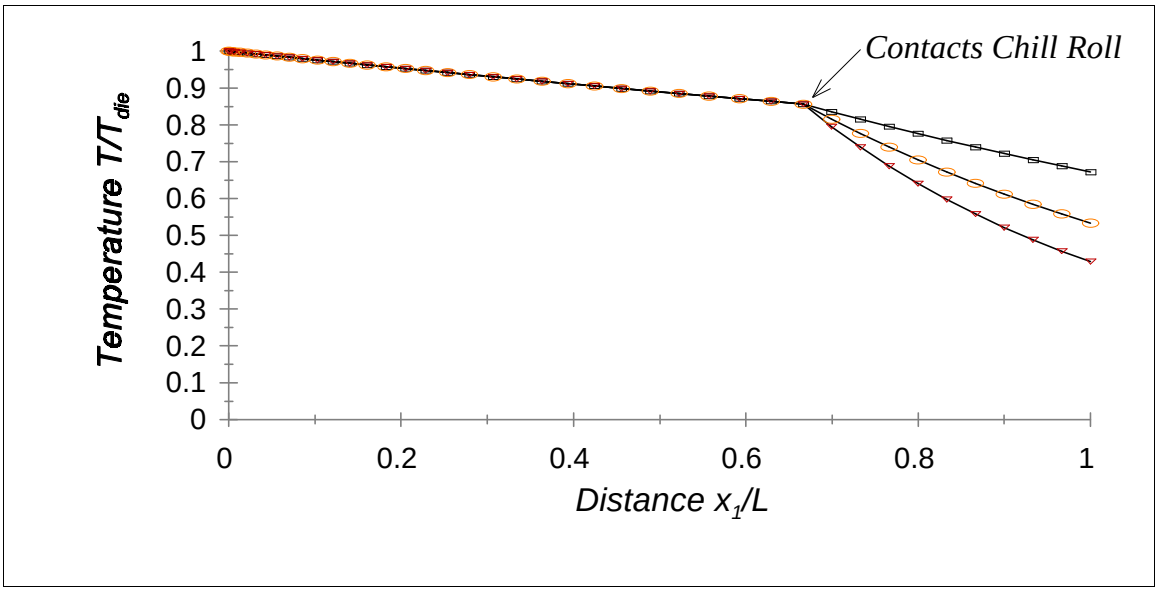

Figure 2.16 Numerical temperature profiles (–) and theoretical profiles for pure advection for α_{gap} = 10 W/(m^2 K) and α_{roll} = 30 (□), 60 (○) and 90 (▽) W/(m^2 K)

As a consequence of the insensitivity of the temperature in the air gap to the heat transfer at the chill roll, the mechanical variables of film casting are also essentially independent of α_{roll}. With α_{roll} values of 30, 60, 90 and 120 W/(m^2 K), the maximum relative difference among all of the simulated thickness distributions is less than 0.3%. Experimental observations support the conclusion that the film's thickness distribution is insensitive to changes in α_{roll}, as they show that the geometry of the film does not change once contact is made with the chill roll (Billon et al. 1991; Cotto et al. 1989). These numerical and experimental results indicate that it is not necessary to model the chill roll to predict the mechanical or thermal response of the film in the air gap.

2.4.2 Effect of Heat Transfer to the Air

To learn the influence of heat transfer to the air, the parameter α_{gap} is given values of 2.0, 10.0 and 20.0 W/(m^2 K). Simulated temperature profiles for these values are provided in Figure 2.17, along with profiles found using the following linear approximation:

$$T = T_{die} - \frac{2\alpha(T_{die} - T_{air})}{\rho C u_1 h} x_1 \qquad \textbf{(2.42)}$$

The slope for this equation comes from the derivative of Equation 2.41, which is constant as long as the exponential function is close to unity. Equation 2.42 has a maximum relative error of 7.1% compared with the numerical solution when α_{gap} = 20.0 W/(m^2 K) and x_1 equals L_{gap}. An increase in the error occurs because the assumption that the slope is constant, made by Equation 2.42, is not strictly valid over the entire range of x_1.

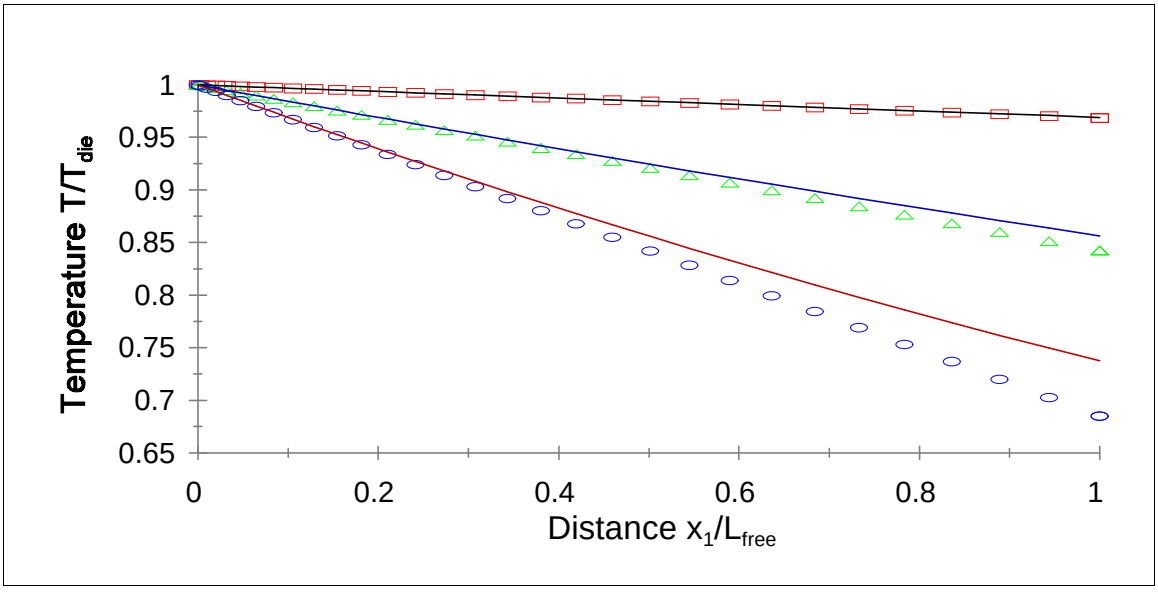

Figure 2.17 Temperature distributions for numerical simulations (–) and using Equation 2.42 with α_{gap} = 2.0 (□), 10.0 (∇), and 20.0 (○) W/(m^2 K)

For larger values of α_{gap} the linear approximation for temperature introduces error, but for smaller values it provides good results, as one might expect. Therefore, the linear temperature profile was used to find an approximate closed-form solution for the nonisothermal velocity (Appendix A.4):

$$u_1 = u_{die} Dr \left(\frac{1 - e^{-amx_1}}{1 - e^{-amL}} \right) \qquad where\ m = \frac{2\alpha_{gap}(T_{die} - T_{air})}{\rho C u_1 h} \qquad \textbf{(2.43)}$$

where "a" is the temperature sensitivity of the Arrhenius equation (Eq. 2.14). Equation 2.43 agrees very well with the numerical results (Figure 2.18), with a maximum relative error of 4.3%. The maximum error occurs for the curve with the highest heat transfer coefficient, because for the higher values of α_{gap} the assumption of a linear temperature profile begins to breaks down. Figure 2.18 shows that as the heat transfer coefficient increases the velocity increases more rapidly. This is a result of a higher α_{gap} leading to a more rapid decrease in T. This in turn causes a higher viscosity, which results in u_1 approaching u_{roll} faster for the same x_1.

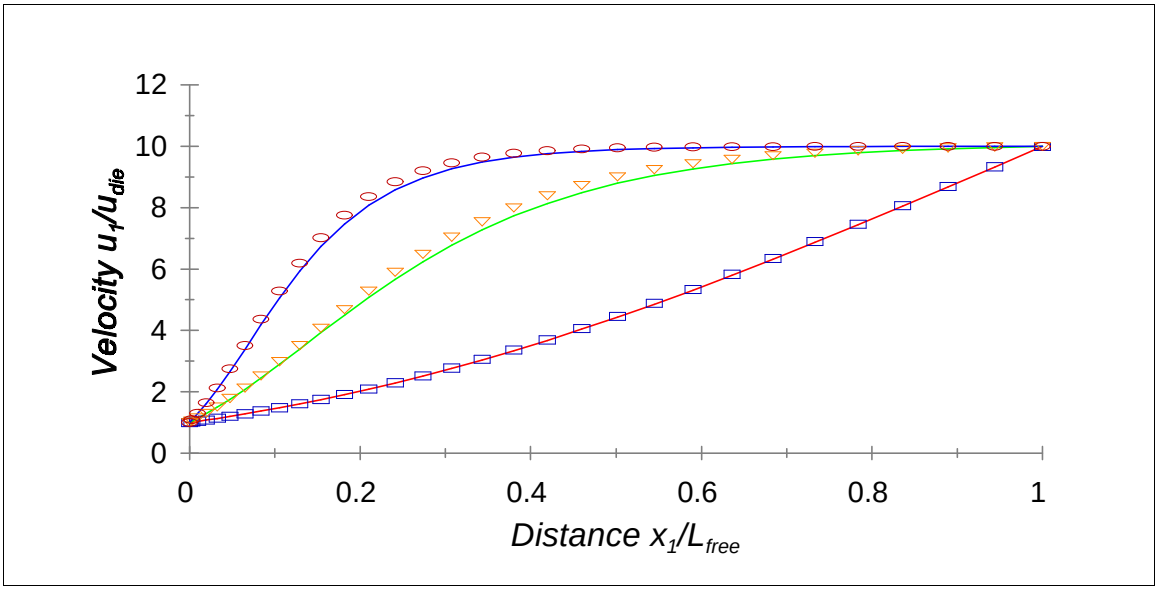

Figure 2.18 Velocity profiles for numerical simulations (–) and for Equation 2.43 with α_{gap} = 2.0 (□), 10.0 (∇) and 20.0 (○) W/(m^2 K)

2.4.3 Effect of the Temperature Sensitivity of the Viscosity

Up to this point in the analysis, the temperature dependence of the viscosity has been modelled using Equation 2.14. This equation has better agreement with viscosity-temperature data near the solidification point than the conventional Arrhenius relation, which is obtained when c equals zero. However, away from the solidification temperature the two relations are essentially the same. In film casting solidification does not occur in the air gap; hence, the more complex viscosity-temperature relation may not be necessary. After rerunning the simulations of section 2.4.2 with c = 0, instead of 5.75, it was found that the original results were reproduced. This suggests that c can be assumed equal to zero and the sensitivity study can focus on the "a" parameter alone.

To determine the influence of the "a" parameter on the film, it was given values on either side of its estimated value of 0.214. Velocity distributions for "a" equal to 0.1, 0.214 and 0.3 are plotted in Figure 2.19 using the numerically simulated results and Equation 2.43. Again the closed-form solution performs well, with a maximum relative difference of 4.7% between the solutions. A comparison of Figure 2.19 with Figure 2.18 shows that varying "a" has a similar effect to varying α_{gap}. Why this occurs is clear from Equation 2.43, which shows that m depends on the parameter "a" and 2α in an identical manner.

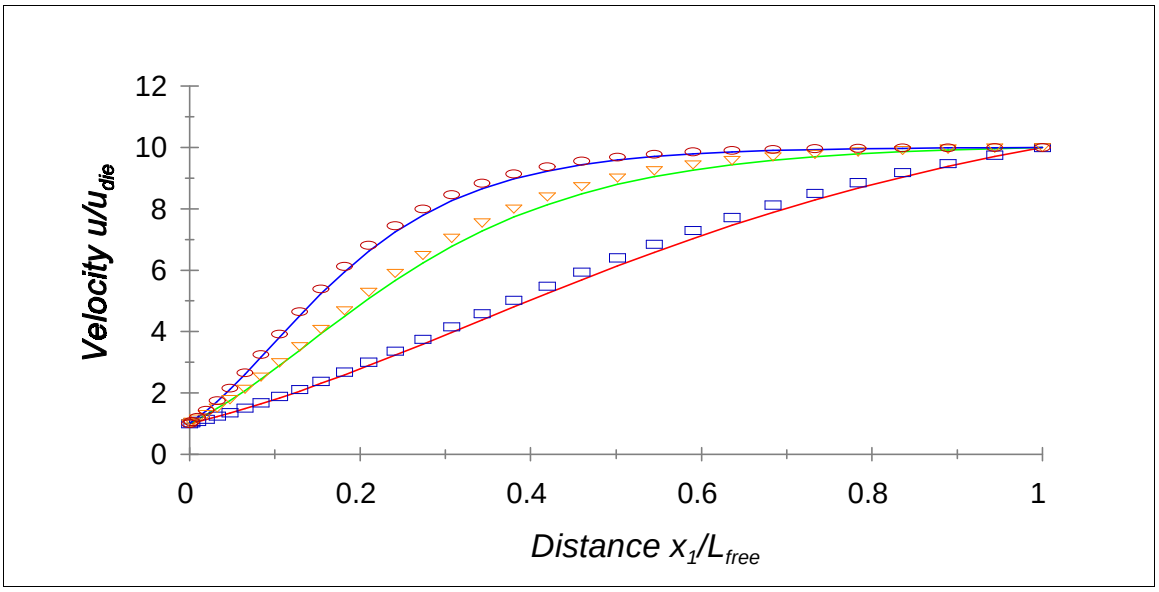

Figure 2.19 Velocity profiles for numerical simulations (–) and using Equation 2.43 with a = 0.1 (□), 0.214 (▽) and 0.3 (○)

2.5 Comparison to Published Experimental Data

Although little experimental data is available for comparison with the model developed in this chapter, Kase (1974) does contain a useful set of temperature and

thickness data for polypropylene (PP) film casting. In order to simulate Kase's experiments, the material properties and processing conditions were required. Unfortunately, Kase does not provide the material properties for the experiment, so they had to be estimated. From another experiment involving PP in the same paper, data are cited as $\rho = 830$ kg/m^3 and $C = 2931$ J/(kg K). An estimate for thermal conductivity (k) is 0.15 W/(m K) (Rauwendaal 1986: 218). For the viscosity-temperature dependence, Tanner (1985: 353) provides typical parameters that correspond to Equation 2.13, $E/R = 5.1\times10^3$ K, $T_o = 190$ °C and $\eta_o = 3.2\times10^3$ Pa·s. Although it is recognized that with this low value of η_o, inertia and gravity may be important, their effects are not included in the simulations that follow. This is done because the PP used by Kase (1974) could have had significantly larger viscosity value. The analysis of Kase supports this possibility because gravity and inertia are ignored. Moreover, the description of the experimental setup does not state whether the film line is vertical or at some other angle. As a result, the effect of gravity on the film is unclear.

Heat transfer properties for the simulations were found by calibration of the model with the temperature data provided by Kase (1974). Kase's experiment for measuring temperature used the following processing conditions: $T_{die} = 215$ °C, $L_{gap} = 0.95$ m, $L_{roll} = 0.242$ m, $u_{die} = 0.015$ m/s, $h_{die} = 990\times10^{-6}$ m and $u_{roll} = 0.5$ m/s. Values for T_{air} and T_{roll} are not provided, so in the simulations that follow they were assumed as 30 °C and 20 °C, respectively. With these processing conditions and Equation 2.41, the heat transfer coefficients were estimated as $\alpha_{gap} \approx 13.0$ W/(m^2 K) and $\alpha_{roll} \approx 52$ W/(m^2 K). Figure 2.20 shows that the experimental data points agree with the simulated results. As expected

from the preceding numerical analyses, the temperature profile is approximately a bilinear function with the sudden change in slope corresponding to contact with the chill roll. These results confirm that the experimental setup is nonisothermal.

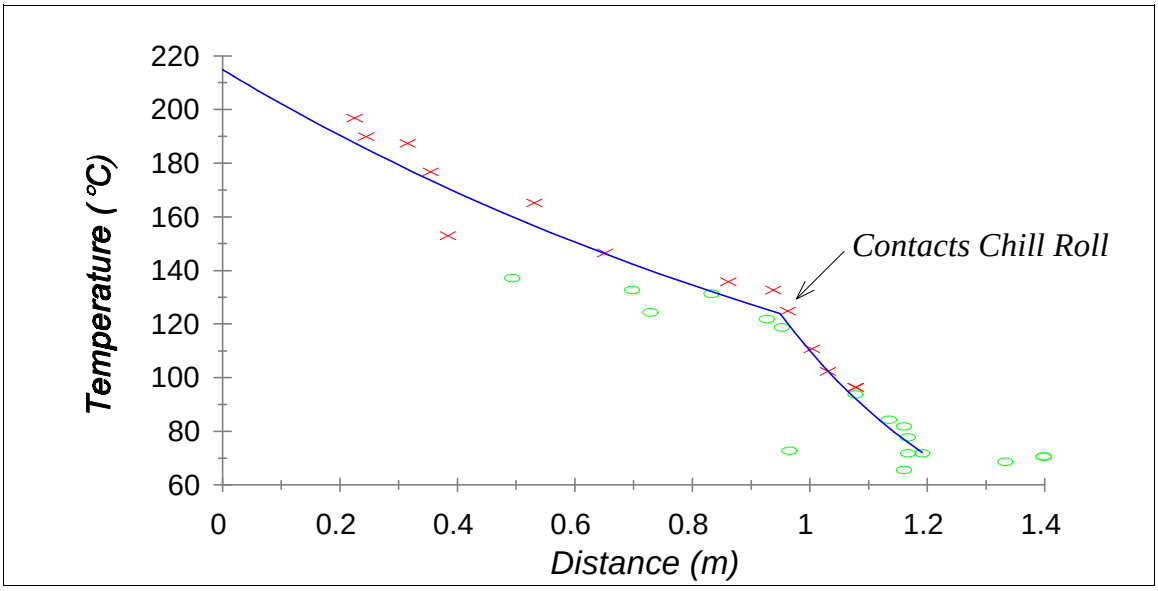

Figure 2.20 Experimental temperature data (x and ○) and numerical simulation results for α_{gap} = 13.0 W/(m^2 K) and α_{roll} = 52 W/(m^2 K) (–)

Once the estimates for the heat transfer coefficients had been established, simulations were completed to compare numerical and experimental thickness data. These data are for two experiments with the same draw ratio of 33, but with different film speeds at the roll. For the first experiment L_{gap} = 0.95 m, u_{die} = 0.0155 m/s, h_{die} = 660×10^{-6} m and u_{roll} = 0.341 m/s and for the second experiment L_{gap} = 0.95 m, u_{die} = 0.0364 m/s, h_{die} = 550×10^{-6} m and u_{roll} = 0.67 m/s. In this list of processing conditions the values for u_{die} and h_{die} are not actually the values at the die, but the values for the first data point past the zone of extrudate swell, as the numerical model neglects this phenomenon.

Figure 2.21, which uses a logarithmic axis for the thickness, shows that the experimental and numerical trends are similar, but the magnitudes differ. Several factors could contribute to the difference. First of all, the quality of the original data is unknown because no error estimates were published and data collection for film casting can be difficult. Secondly, the constitutive model developed in this chapter, which neglects elasticity, could be an important factor. Seyed and Papanastasiou (1991) favour this explanation and show that including viscoelasticity leads to better agreement with the data of Kase (1974). Finally, PP can have a large range of material properties and the properties assumed in this simulation could very well be different than the actual ones. For instance, if the viscosity of the actual polymer were less dependent on the temperature, then the simulated results for thickness would be in better agreement with the experimental data. This can be seen by considering how a reduction in temperature dependence would improve agreement with the experimental data; the simulated results would approach the isothermal solution, which would improve agreement because the isothermal solution is a straight line on a semi-logarithmic plot. This influence of the temperature dependence of viscosity explains why the higher roll speed is in better agreement with the experimental data than the lower speed. For the higher speed the temperature does not decrease as much, so the influence of the viscosity-temperature dependence is not as pronounced and the simulated results are closer to the approximately linear experimental data.

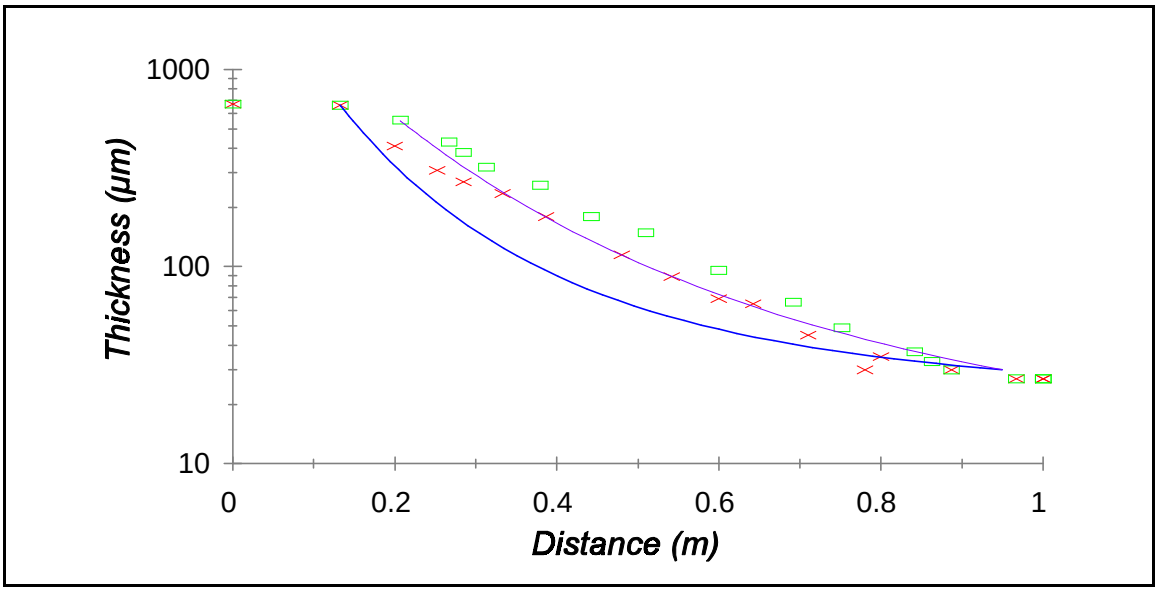

Figure 2.21 Comparison between experimental thickness profiles for u_{roll} = 0.34 m/s (x) and u_{roll} = 0.67 m/s (□) against the corresponding nonisothermal simulations, (–) and (---), respectively

2.6 Summary of Results

The governing mechanical and thermal equations for the cast film process, along with their associated boundary conditions, have been presented in this chapter. Also presented were the following physical requirements for the system: the film is thin; the thickness gradient is small; viscoelasticity can be ignored; a simple heat transfer model is adequate; viscous dissipation and surface tension can be ignored and self-weight and inertia are only important for low viscosity polymers. This chapter also detailed the solution technique for the coupled thermomechanical system, for which upwinding was found to be unnecessary. In addition, this chapter demonstrated that isothermal simulations reproduce the closed-form solutions for a viscous fluid including and excluding the influence of self-weight. For the nonisothermal simulations, it was

observed that the mechanical and thermal results are insensitive to the heat transfer over the roll. Therefore, modelling this part of the process is not necessary. The numerical results for the nonisothermal simulations also suggested a theoretical approximation for the temperature and velocity profiles. These approximate solutions agreed well with the numerical results. By considering the approximate solutions, it was seen that the temperature sensitivity of the viscosity and the heat transfer coefficient affect the velocity profile in the same way. Finally, this chapter compared the numerical results with some experimental data available in the literature. Although the thermal model agreed with the experimental data, the mechanical predictions were off. The discrepancy was accounted for by experimental error, uncertainty in the material parameters and the influence of viscoelasticity.

Chapter 3 Two-Dimensional Model

Although the 1D model of the previous chapter provides useful insight into film casting, a 2D model is necessary to capture the neck-in and edge bead phenomena. A 2D finite element model, which allows the thickness to vary in the transverse direction, is developed in this chapter for nonisothermal film casting of a viscous fluid. The model accommodates low viscosity polymers by including inertia and gravity. However, the sag of the film, the elasticity of the polymer and die swell are neglected. A Newton-Raphson algorithm is used to solve simultaneously for the velocity, thickness and temperature distributions, as well as for the width of the sheet.

Section 3.1 presents the governing thermomechanical equations and boundary conditions, while Section 3.2 presents the numerical algorithm used to solve the system of equations. Section 3.3 compares isothermal simulations with a closed-form solution and with published results. The nonisothermal finite element model is the subject of Section 3.4. In this section the influence of gravity on film casting is also investigated. Nontrivial boundary conditions, such as a nonconstant thickness at the die or localized cooling jets, are the topic of Section 3.5. Finally, Section 3.6 summarizes the results for the 2D simulations.

3.1 Governing Equations and Boundary Conditions

This section presents the two-dimensional model of the cast film process using the same physical requirements as discussed in Section 2.1.3; that is, the film is thin, the thickness gradient is small, elasticity is neglected, and a simple thermal model is considered adequate. The 2D setup is defined in Figure 3.1, in which the origin of the axes is centred between the die lips, L is the length of the air gap and $2w_{die}$ is the total width of the film at the inlet. In the simulations that follow, only half the width of the film (w_{die}) is modelled as the sheet is assumed to be symmetric.

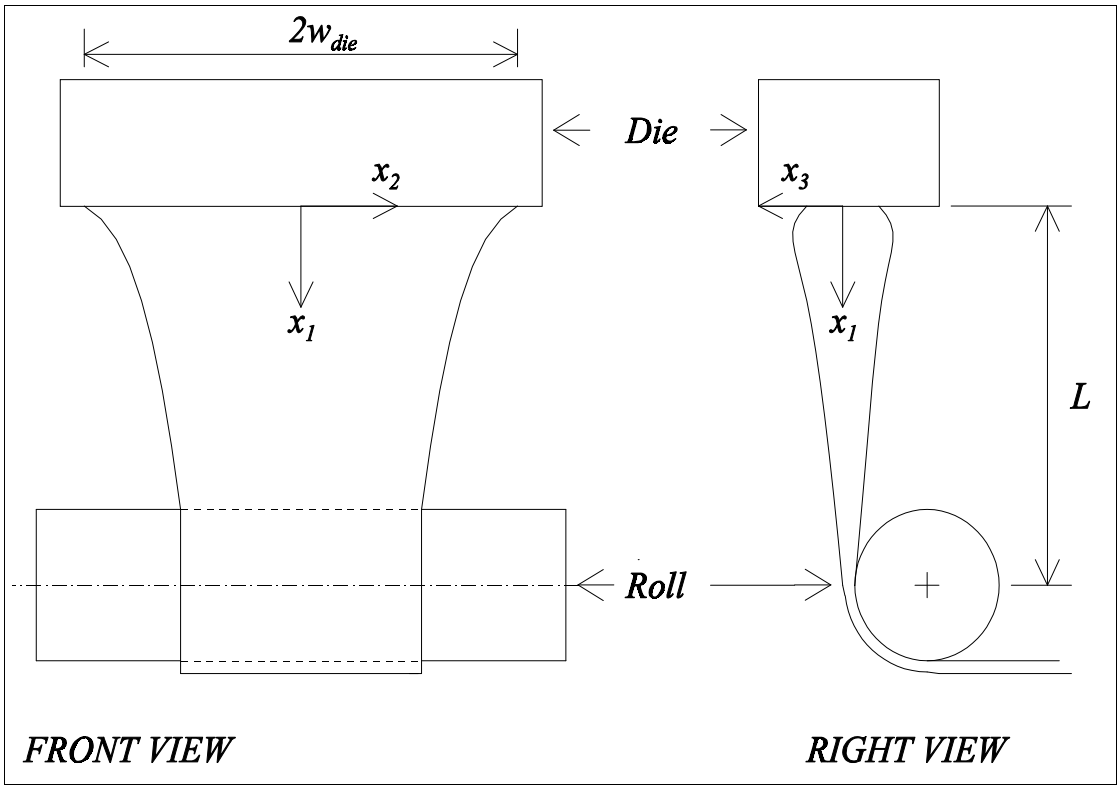

Figure 3.1 Setup for two-dimensional film casting

3.1.1 Mechanical Equations

To derive the momentum equation, the same approach as that used in Section 2.1.1 can be applied in two dimensions, to yield

$$\frac{\partial(h\sigma_{\alpha\beta})}{\partial x_\beta} + \rho h b_\alpha = \rho h u_\beta \frac{\partial u_\alpha}{\partial x_\beta} \qquad \textbf{(3.1)}$$

in which h is the thickness, $\sigma_{\alpha\beta}$ is the planar stress tensor, ρ is the density, b is the acceleration vector and u_α is the velocity vector. For the subscripts α and β, the Einstein summation convention is applied over the range of 1 to 2. If the film is vertical, then the acceleration vector has the components $b_1 = g$ and $b_2 = 0$.

The continuity equation can also be derived using an approach similar to that of Section 2.1.1, to find

$$\frac{\partial(hu_\alpha)}{\partial x_\alpha} = \frac{\partial h}{\partial x_\alpha} u_\alpha + h\frac{\partial u_\alpha}{\partial x_\alpha} = 0 \qquad \textbf{(3.2)}$$

To relate the stress to the rate of deformation, the Newtonian constitutive equation (Eq. 2.4) is used, along with the relation between the pressure (p) and the out-of-plane rate of deformation ($\partial u_3/\partial x_3$) (Eq. 2.5). Unlike in 1D, for the 2D case the rate of deformation in the transverse direction ($\partial u_2/\partial x_2$) is not zero; therefore, continuity requires

$$\frac{\partial u_3}{\partial x_3} = -\left(\frac{\partial u_1}{\partial x_1} + \frac{\partial u_2}{\partial x_2}\right) = -(\varepsilon_{11} + \varepsilon_{22}) = -\varepsilon_{\alpha\alpha} \qquad \textbf{(3.3)}$$

If Equations 2.5 and 3.3 are substituted into Equation 2.4, then the constitutive equation can be expressed as

$$\sigma_{\alpha\beta} = 2\eta(\varepsilon_{\alpha\beta} + \varepsilon_{\gamma\gamma}\delta_{\alpha\beta}) \qquad \textbf{(3.4)}$$

Figure 3.2 defines, for the domain Ω, the boundaries at the die, roll, line of symmetry and free surface as Γ_{die}, Γ_{roll}, Γ_{sym}, and Γ_{free}, respectively. At these surfaces the mechanical boundary conditions are as follows:

$$
\begin{aligned}
&\text{on } \Gamma_{die} && u_1 = u_{die};\ u_2 = 0;\ h = h_{die} \\
&\text{on } \Gamma_{roll} && u_1 = u_{roll};\ u_2 = 0 \\
&\text{on } \Gamma_{sym} && u_2 = 0;\ \sigma_{12} = 0 \\
&\text{on } \Gamma_{free} && \sigma_{\alpha\beta} n_\beta = 0;\ u_\alpha n_\alpha = 0 \\
&\text{on } \Gamma_{free} \cap \Gamma_{die} && w = w_{die}
\end{aligned}
\qquad \textbf{(3.5)}
$$

where n_α is the unit vector normal to the free surface and the last boundary condition applies at the intersection of the free surface and the die.

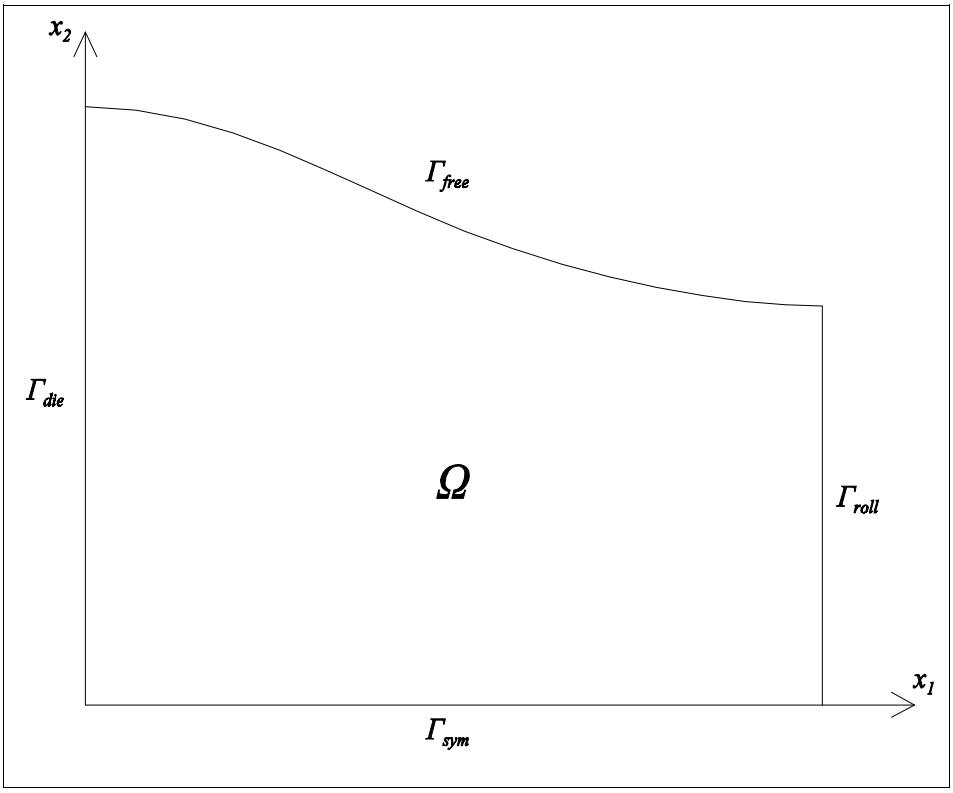

Figure 3.2 Boundaries for the two-dimensional domain

At the free surface, the boundary conditions are for zero traction and zero mass flux. The mass flux boundary condition can be used to find the free surface (w), where w is function of the distance along the machine direction:

$$w = w(x_1) \tag{3.6}$$

The normal to the free surface is the negative reciprocal of the slope of this equation. As the normal can be related to the free surface, the zero flux boundary condition can be used to find the free surface. This is done by setting the dot product of the velocity vector and the normal vector to zero; that is,

$$\begin{aligned} u_\alpha n_\alpha &= 0 \\ \therefore \frac{\partial w}{\partial x_1} u_1 - u_2 &= 0 \end{aligned} \tag{3.7}$$

3.1.2 Heat Transfer Equations

The 1D approach of Section 2.1.2 can be extended to two dimensions to find the conservation of thermal energy equation,

$$\rho C h u_\alpha \frac{\partial T}{\partial x_\alpha} + 2\alpha(T - T_{air}) - kh\frac{\partial^2 T}{\partial x_\alpha \partial x_\alpha} = 0 \tag{3.8}$$

Section 2.1.2 explained how to estimate α over the air gap. Furthermore, the parametric study of Section 2.4.1 showed that modelling the heat transfer over the chill roll is unnecessary, as the film's geometry does not change once the film contacts the roll. The equations for viscosity as a function of temperature are provided in Section 2.1.2. Based on the observations from the parametric study of the viscosity-temperature dependence of Section 2.4.3, the 2D model uses the simpler Arrhenius relation that does not include a sharp increase in viscosity near the solidification point; that is, c = 0 in Equation 2.14.

Thermal boundary conditions are defined, with reference to Figure 3.2, as follows:

$$\begin{aligned} &\text{on } \Gamma_{die} && T = T_{die} \\ &\text{on } \Gamma_{roll},\ \Gamma_{sym},\ \text{and } \Gamma_{free} && q_\alpha n_\alpha = 0 \end{aligned} \qquad \textbf{(3.9)}$$

where q_α is the thermal flux vector and n_α is the unit vector normal to the surfaces. Although the thermal flux normal to the free surface is not actually zero, it is assumed zero as the heat transfer over the edge is much smaller than that over the rest of the film's surface. At the roll the thermal flux is also assumed zero for the reasons discussed in Section 2.2.1.

3.2 Solution of the Coupled System

To solve the 2D thermomechanical system, the algorithm developed for the 1D case can be used, except that in 2D there is an additional velocity degree of freedom and an unknown free surface. This section presents the 2D finite element equations and coupled solution algorithm for finding the free surface and the velocity, thickness and temperature fields.

3.2.1 Finite Element Equations

The weak form of the equilibrium equation is found by multiplying Equation 3.1 by a virtual velocity vector (δu_α), integrating over the domain (Ω) and applying Gauss's theorem:

$$\int_\Omega \delta\varepsilon_{\alpha\beta}\sigma_{\alpha\beta} h d\Omega + \int_\Omega \delta u_\alpha \rho h u_\beta \frac{\partial u_\alpha}{\partial x_\beta} d\Omega = \int_\Gamma \delta u_\alpha \overline{T}_\alpha h d\Gamma + \int_\Omega \delta u_\alpha \rho h b_\alpha d\Omega \qquad \textbf{(3.10)}$$

in which $\delta\varepsilon_{\alpha\beta}$ is the virtual rate of deformation that is consistent with the virtual velocity vector and $\overline{T}_\alpha$ is the traction applied to the boundary. However, in the simulations that follow, the load-controlled boundary-valued problem is not solved, as the displacement-controlled problem is more representative of film casting.

For the continuity equation (Eq. 3.2), the integral equivalent is found by multiplying by a weighting function (δh) and integrating over the domain:

$$\int_\Omega \delta h\left(\frac{\partial h}{\partial x_\alpha} u_\alpha + h\frac{\partial u_\alpha}{\partial x_\alpha}\right) d\Omega = 0 \qquad \textbf{(3.11)}$$

Similarly, the weighted residual form of the conservation of thermal energy equation involves multiplication of Equation 3.8 by a virtual temperature (δT), integration over the domain and application of Gauss's theorem:

$$\int_\Omega \delta T \rho C h u_\alpha \frac{\partial T}{\partial x_\alpha} d\Omega + \int_\Omega \frac{\partial \delta T}{\partial x_\alpha} kh \frac{\partial T}{\partial x_\alpha} d\Omega + \int_\Omega \delta T \cdot 2\alpha T d\Omega = \int_\Omega \delta T \cdot 2\alpha T_{air} d\Omega \qquad \textbf{(3.12)}$$

In this equation the load due to the thermal flux at the free surface is not included as the thermal boundary conditions (Eq. 3.9) specify zero flux. When Equation 3.12 was solved upwinding was not introduced, as the results of Section 2.2.3 demonstrate that it is unnecessary.

Finally, the kinematic boundary condition for the free surface (Γ_{free}) can also be expressed in an integral equivalent form. Equation 3.7 is multiplied by a weighting function (δw) and integrated over the free surface to obtain

$$\int_{\Gamma_{free}} \delta w \frac{dw}{dx_1} u_1 d\Gamma_{free} = \int_{\Gamma_{free}} \delta w u_2 d\Gamma_{free} \qquad \textbf{(3.13)}$$

When $\frac{dw}{dx_1}$ is integrated over the free surface, the chain rule was used to express the derivative as $\frac{dw}{ds}\frac{ds}{dx_1}$, where s is the arc length along the free surface.

A solution for steady state film casting is found by satisfying Equations 3.4, 3.10, 3.11, and 3.12, with the boundary conditions of Equations 3.5, 3.9, and 3.13. To find this solution a finite element discretization was introduced, as shown in Figure 3.3. Over the film's surface three-noded triangular elements were used as they are simple, spatially isotropic elements. At the film's edge two-noded elements were used. For the triangular elements each node has four degrees of freedom: u_1, u_2, h and T. An additional degree of freedom was introduced for the linear elements, the film's width. The finite element equations were obtained by substitution of this discretization, with the appropriate shape functions and shape function derivatives, into the system of equations and boundary conditions. Appendix B.2 provides the details on the calculations of the stiffness matrices and load vectors for the solution of the boundary value problem.

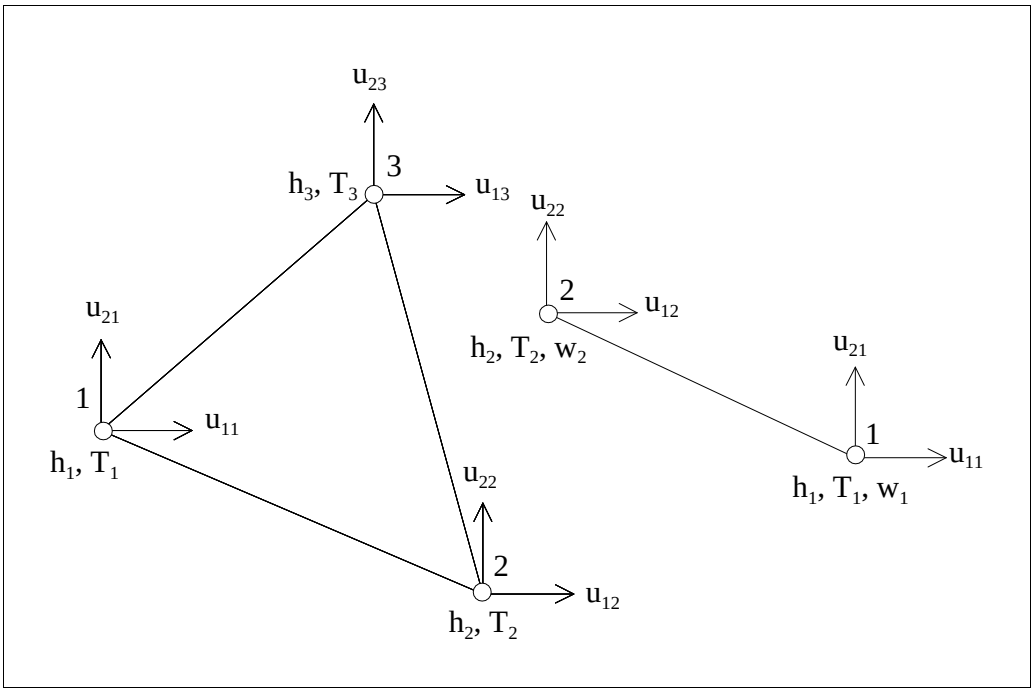

Figure 3.3 Surface element (three-noded) and edge element (two-noded) for finite element discretization of 2D film casting

3.2.2 Solution Algorithm

The overall solution algorithm can be summarized with a flowchart (Figure 3.4). This flowchart shows that, unlike in the 1D case, for convergence in 2D the final draw ratio (Dr) must be approached in an incremental fashion. This is necessary because for the 2D case the geometry is unknown at the outset. Since the draw ratio is incremented, the 2D algorithm did not require incrementing the heat transfer coefficient, as was done in the 1D case.

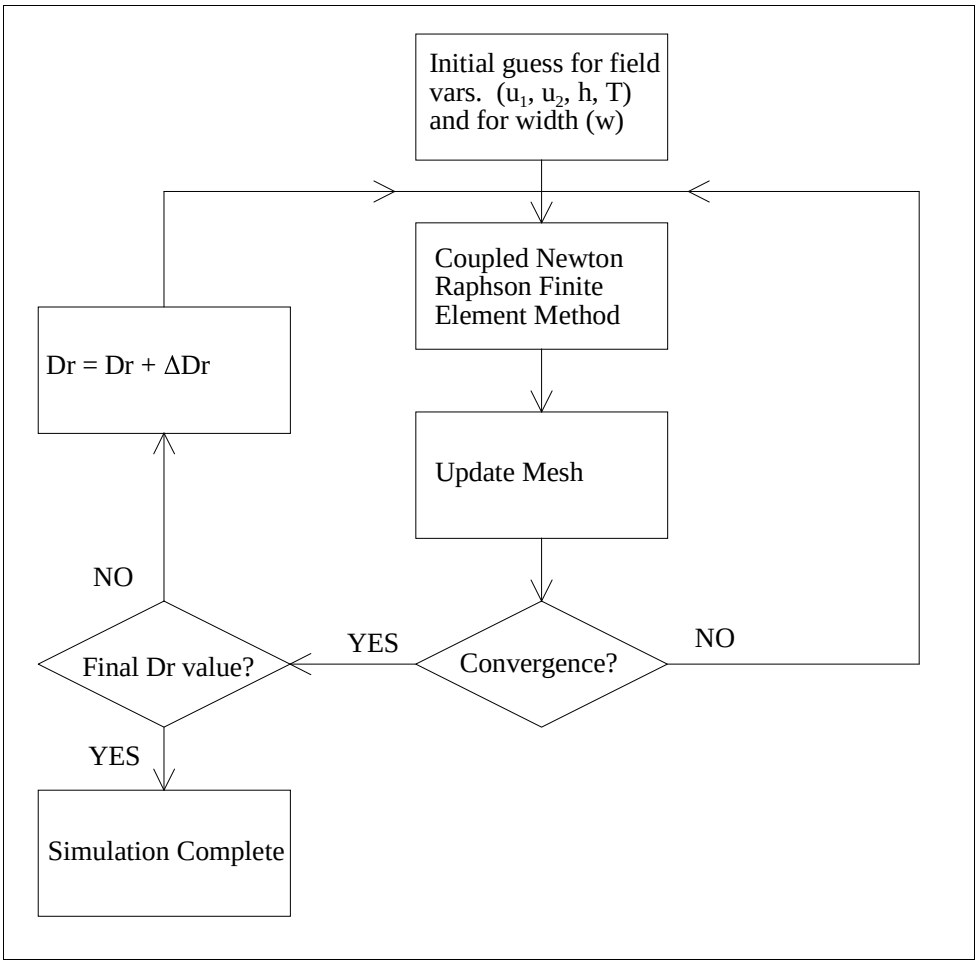

Figure 3.4 Flowchart of the algorithm used for the numerical simulation of 2D film casting

The initial guesses used for the field variables were the 1D closed-form solutions. For u_1, the isothermal solution (Appendix A.1) and the nonisothermal solution (Eq. 2.43) were used as appropriate. A value of zero was assumed as the initial guess for u_2, and h was found from the continuity requirement. Equation 2.42 was used for the initial estimate of the temperature. A rectangular domain was used for the initial geometry; that is, all of the width values were initially set equal to w_{die}.

Within each iteration the variables were updated using the finite element method. Section 2.2.2 describes how the Newton-Raphson method was used and Appendix B.2 details how the tangential stiffness matrices for the 2D system were derived. With each new estimate for the free surface, the mesh geometry was updated. This involved changing the x_2-coordinates of the nodes so that the new x_2 values maintained the same ratio to the new width as they had with the previous width.

The convergence criterion used in 2D was the same as that for the 1D case, except that the width variable was also considered:

$$Max\left(\frac{\|\Delta \boldsymbol{u}\|}{\|\boldsymbol{u}\|}, \frac{\|\Delta \boldsymbol{h}\|}{\|\boldsymbol{h}\|}, \frac{\|\Delta \boldsymbol{T}\|}{\|\boldsymbol{T}\|}, \frac{\|\Delta \boldsymbol{w}\|}{\|\boldsymbol{w}\|} \right) \leq Tolerance \qquad \text{where } \|\boldsymbol{u}\| = \sqrt{\boldsymbol{u}\boldsymbol{u}^T} \text{ etc.} \tag{3.14}$$

in which **u**, **h**, **T** and **w** are the current solutions for the velocity, thickness, temperature and width degrees of freedom, Δ represents the change in these variables and $\| \ \|$ represents the Euclidean norm of the vector. Unless stated otherwise, the 2D studies used a tolerance of 0.01.

3.3 Performance of the Isothermal Model

Before proceeding to nonisothermal problems, two comparisons are made involving isothermal simulations. One comparison is with a closed-form solution that assumes no edge bead, and the other is with published simulation results.

3.3.1 Comparison with a Closed-Form Solution that Assumes no Edge Bead

As mentioned in the literature review of Section 1.2.1, the 2D closed-form solution proposed by Sergent (1977) has been employed in many subsequent studies.

Sergent's model, which is summarized in Appendix A.6, cannot capture an edge bead because the model assumes that the thickness does not vary in the transverse direction. Since the current study does not make this assumption, the influence of an edge bead on the force, thickness and neck-in ratio can be observed by comparing the numerical solution of this study with Sergent's closed-form solution.

The closed-form solution of Sergent (1977) is presented in Avenas et al. (1986: 368) and Agassant et al. (1991: 249) through an example film casting problem. This example problem was used as the basis for the current comparison. For this problem the polymer has a viscosity of 3×10^4 Pa·s and processing conditions that are defined in Figure 3.5. The figure also shows the 2400 element mesh used for the simulation. A finer mesh was not required, as more than doubling the number of elements to 5408 resulted in little change in the variables. Similarly, a tolerance of 10^{-2} is adequate, as decreasing the tolerance to 10^{-6} also resulted in only minor changes to the variables.

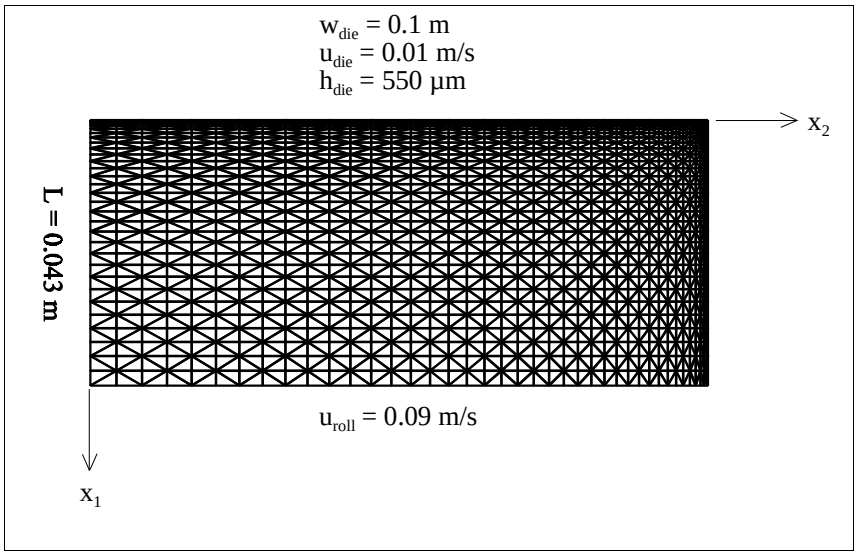

Figure 3.5 Processing conditions and mesh for comparison to the closed-form solution that assumes no edge bead

Figure 3.6 shows that the free surface found by the closed-form solution is linear, while the free surface found by the numerical algorithm is curved. The difference in the two solutions can be accounted for by Sergent's exclusion of the free surface boundary condition (Eq. 3.7). This boundary condition is responsible for the curved shape because it requires the free surface to have a zero slope at the die and roll. A zero slope is obtained at these locations as $u_2 = 0$ and $u_1 \neq 0$ and thus Equation 3.7 leads to $dw/dx_1 = 0$. Introduction of the free surface boundary condition leads to a more realistic simulation of the free surface, as the predicted curved shape is in better qualitative agreement with experimental evidence than the linear surface, which would have been obtained otherwise (d'Halewyu et al. 1990; Barq et al. 1992).

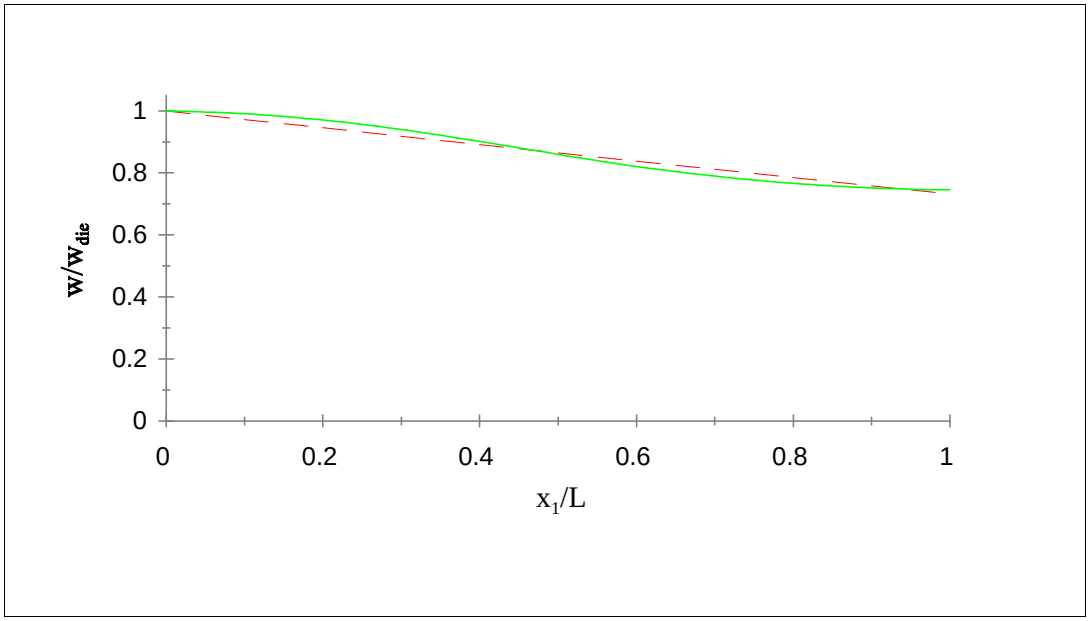

Figure 3.6 Free surface for the closed-form solution (---) and for the numerical simulation (–-)

A comparison of the thickness across different cross-sections of the film (Figure 3.7) shows that the numerical simulation does not agree with the closed-form solution's

assumption of constant thickness. In fact, the numerical solution shows a U-shape with a significant edge bead. This shape is qualitatively similar to the experimental data of Chambon et al. (1996) for a viscous polymer. However, the U-shaped profile does not compare well with typical industrial polymer casting, which shows a close to uniform thickness over the middle of the film and a rapid rise near the edge. Another feature of Figure 3.7 is several sharp oscillations in the slope of the thickness profile near the edge of the film. A possible explanation for these changes is that the assumption made in the model's derivation that the thickness gradient is small does not apply at the edge of the film.

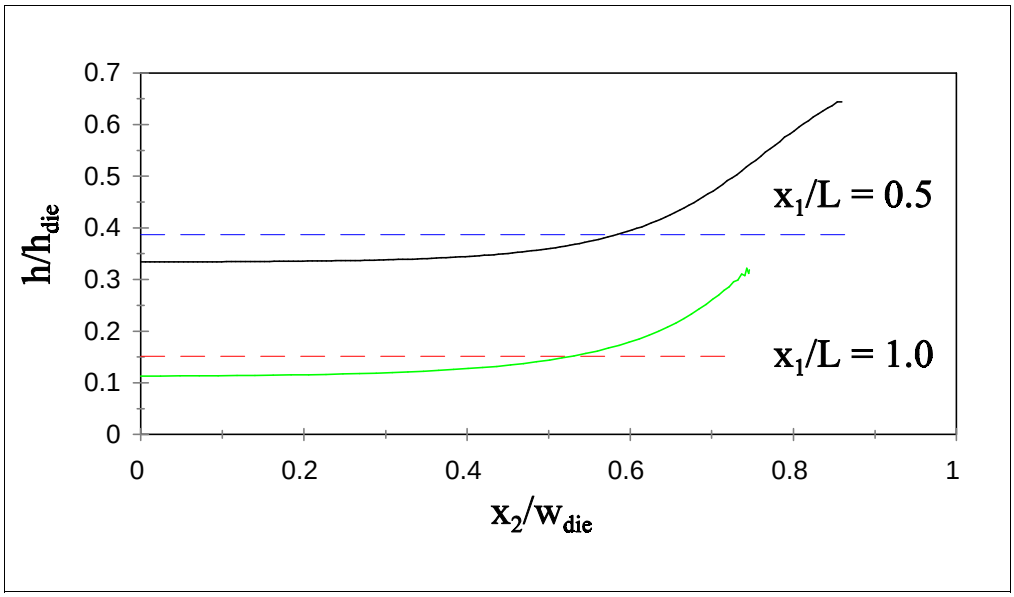

Figure 3.7 Thickness profiles across two cross-sections for the closed-form solution (---) and for the numerical simulation (–-)

The above comparisons between the closed-form and numerical solutions were made at one draw ratio; comparisons can also be made to see how the solutions change as the draw ratio is varied. Figure 3.8 shows the dependence of thickness, neck-in and force

on the draw ratio. In this figure, the thickness for the numerical simulation is taken as that at the line of symmetry and the force (F) is found from numerically integrating the following equation:

$$F = 2\int_{0}^{w_{roll}} h\sigma_{11}dx_2 \qquad \textbf{(3.15)}$$

in which w_{roll} is the film's half width at the roll. Figure 3.8 shows that the force agrees well between the two solutions. This agreement is a result of equilibrium requiring that the tensile force at the die and roll be equal. Both the closed-form and the numerical solutions should have a similar force at the roll, since both have similar responses at the die. For the thickness, the numerical solution follows the same trend as the closed-form solution, while remaining consistently below it. This behaviour is likely due to the edge beads, as thicker edges mean that, for a constant mass flux, less material is available to pass over the middle of the film. Finally, the width can be compared between the two solution techniques. Although a similar trend is observed, the numerical solution now lies above the closed-form one. This finding may again be related to the presence of an edge bead, as a thicker edge will likely resist neck-in more effectively. Moreover, if the finite element prediction for thickness is below the closed-form solution, then the reverse has to be true for the width values, or else the mass flux is not conserved.

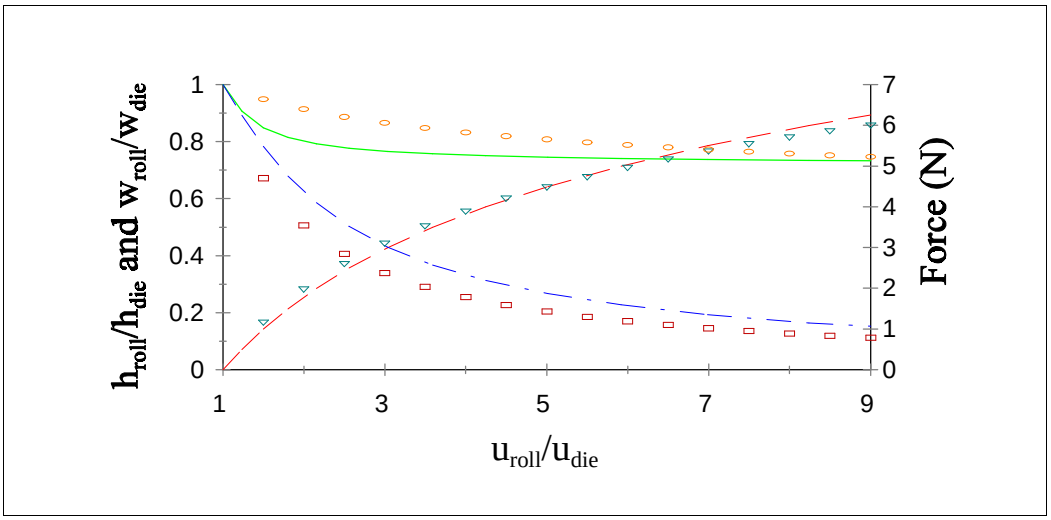

Figure 3.8 Force (∇), width (○) and thickness (□) variation for the closed-form solution and the corresponding numerical solutions (---, – –, and ·–·–, respectively)

3.3.2 Comparison with Published Results that Allow an Edge Bead

In the published film casting research two studies, namely d'Halewyu et al. (1990) and Sakaki et al. (1996), simulate the same problem, but obtain different thickness and neck-in results. The problem in question is defined as follows: w_{die} = 0.5 m, L = 0.2 m, u_{die} = 0.01 m/s, h_{die} = 0.001 m and Dr = 10. Figure 3.9 shows the thickness profile at the chill roll for both published studies, and for a simulation using the algorithm proposed in this study. This figure shows that the 3D formulation of Sakaki et al. (1996) has a greater neck-in than the 2D formulation of d'Halewyu et al (1990). The greater neck-in cannot, however, be accounted for by one study being 3D and the other 2D, as the current study is 2D and it supports the 3D results of Sakaki et al. (1996). One reason for the difference may be the method used by d'Halewyu et al. (1990) to relate the free surface and the normal vector, as the paper does not detail what approach is used. Another possible

explanation might be because the velocity and thickness are uncoupled in the numerical algorithm of d'Halewyu et al. (1990), and this causes convergence to a solution different from that of the other algorithms. As a final point, Figure 3.9 shows, at least for the simulation in question, that there is little reason for resorting to a 3D formulation over a 2D one.

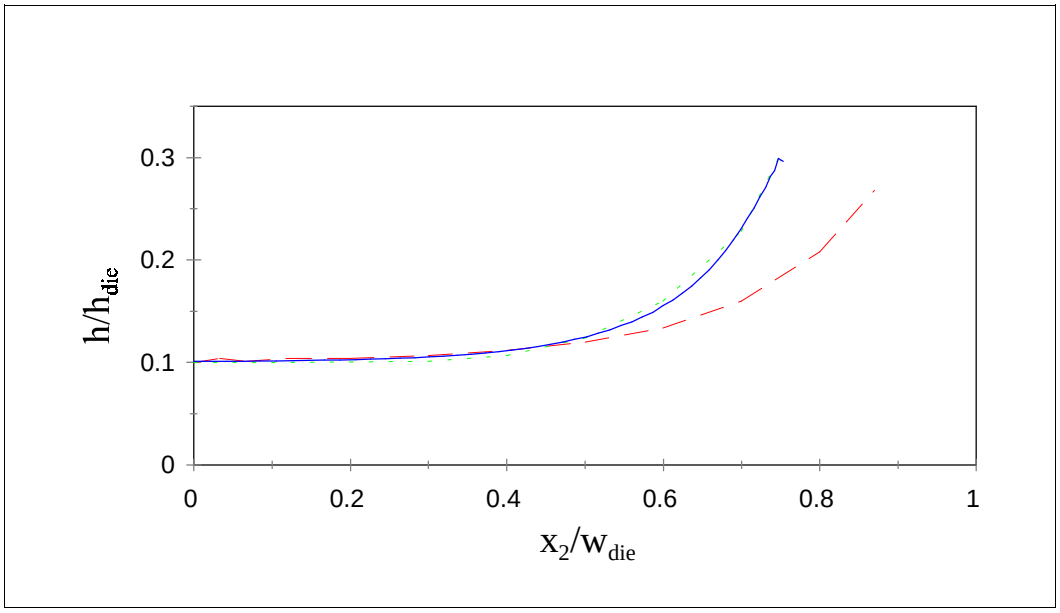

Figure 3.9 Thickness profile at the chill roll for d'Halewyu et al. (1990) (---), Sakaki et al. (1996) (···) and for the current study (–)

3.4 Performance of the Nonisothermal Model

In this section the influence of gravity on 2D nonisothermal film casting is investigated. In addition, a parametric study is conducted to examine the effects of heat transfer on the field variables and on the width of the film.

3.4.1 The Influence of Gravity on Film Casting

The study of Barq et al. (1992) provides a good context for investigating the influence of gravity on film casting, as this study deals with a low viscosity polymer. Although Barq et al. (1992) provides a good starting point for the investigation, a full comparison with their results cannot be made as some of their data were not published for proprietary reasons.

The polymer used by Barq et al. (1992) is polyethylene terephthalate (PET), for which they provide the following data: η_0 = 119 Pa·s, E/R = 6498 K, T_0 = 553 K, k = 0.25 W/(m K), ρ = 1340 kg/m^3 and C = 1991 J/(kg K). These data use Equation 2.13 for the viscosity-temperature dependence. The values of the other material parameters are approximated at a temperature of 278 °C. This temperature was chosen as a representative value as, according to the experimental data of Barq et al. (1992), this is the average temperature of the film midway between the die and roll.

In the simulations that follow, gravity and inertia have an influence because the viscosity of the polymer is low. To see the influence of self-weight one simulation was vertical and the other horizontal. For the horizontal simulation the sag of the film was neglected. The simulations assume the following processing conditions: w_{die} = 0.5 m, L = 0.2 m, u_{die} = 0.1 m/s, h_{die} = 0.001 m and Dr = 10. Regarding the thermal conditions, the temperature data presented by Barq et al. (1992) shows an approximately linear trend decreasing from T_{die} = 282 °C to 270 °C; therefore, using T_{air} = 30 °C and Equation 2.41, the heat transfer coefficient was estimated as 34.0 W/(m^2 K). In the numerical simulations a 5408-element mesh was used.

Before discussing the influence of gravity, the temperature dependence of the process is considered. The temperature field of the current simulation agrees with the linear trend found in the data of Barq et al. (1992). This is noteworthy, since Barq et al. (1992) use a much more complex thermal model than that adopted in the current study. Figure 3.10 shows that changes in temperature have little influence on the thickness profiles at the chill roll, as the isothermal and nonisothermal simulations are close to identical. This agrees with the conclusion of Barq et al. (1992) that a nonisothermal model is unnecessary for the PET in question under typical processing conditions.

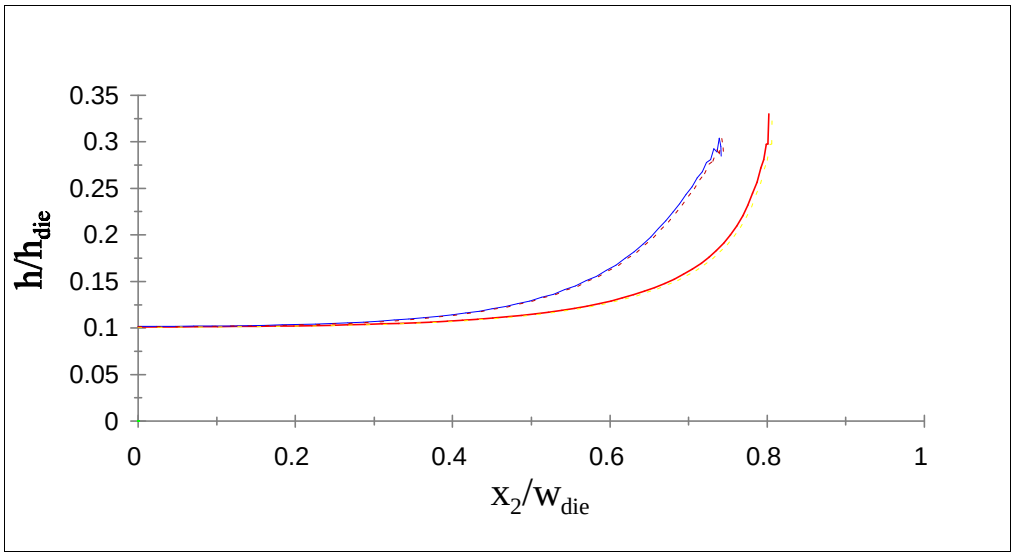

Figure 3.10 Thickness profile at the chill roll for nonisothermal simulations of vertical film casting (–) and horizontal film casting (--). Isothermal simulations (···) are also included.

Figure 3.10 shows that the influence of gravity for vertical simulations is to cause less neck-in and a larger edge bead than when the film is horizontal. This is because, with gravity, the thicker film at the edge falls more rapidly and thus reaches the roll sooner than when self-weight is not an issue. Figure 3.10 also shows that gravity aids in

promoting a more uniform thickness, which in turn leads to a larger edge bead, so that the continuity requirement can be met. The conclusion from this simulation then is that the self-weight of a polymer can be used to promote uniform thickness for low viscosity, low elasticity, low temperature dependence film casting. This influence would likely be increased if the speed at the die is decreased, as Equation 2.24 suggests that a decrease in u_{die} may lead to an increase in the relative contribution of self-weight over viscous forces.

To see how self-weight influences the thickness field, the thickness contours for vertical and horizontal film casting are compared in Figure 3.11. This figure shows the expected behaviour that the vertical casting draws the thickness down more rapidly, which is shown by the closer contour lines at the die. Figure 3.11 also demonstrates that the more pronounced edge bead for vertical casting, shown in Figure 3.10, is not limited to the chill roll. The thickness is more uniform for other film cross-sections as well. This manifests itself in the more pronounced bend in the vertical film's contours as the edge is approached.

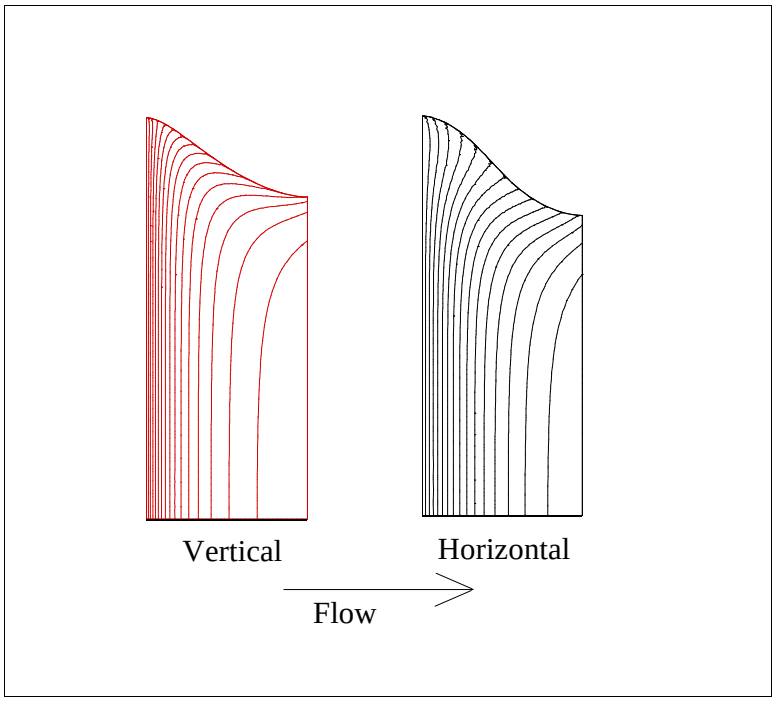

Figure 3.11 Thickness contours for vertical and horizontal film casting

3.4.2 Nonisothermal Effect on Edge Bead

To see the effect of heat transfer on film casting, simulations were conducted with heat transfer coefficients of 0, 5, 10, and 15 W/(m^2 K). These simulations were done with the LDPE material used in the 1D simulations of the previous chapter. For this polymer, with Equation 2.14 for the viscosity, the material parameters are as follows: $\eta_0 = 1.6\times10^5$ Pa·s, $T_0 = 180$ °C, a = 0.214, c = 0, $\rho = 920$ kg/m^3, k = 0.24 W/(m K), and C = 2300 J/(kg K). In these simulations, the processing conditions were assumed to be, $w_{die} = 0.5$ m, L = 0.2 m, $u_{die} = 0.01$ m/s, $h_{die} = 0.001$ m, $T_{die} = 180$ °C, and $T_{air} = 30$ °C.

The simulations show that, overall, higher heat transfer results in less neck-in. This is illustrated in Figure 3.12, which plots the dependence of w_{roll}/w_{die} on Dr for different heat transfer coefficients. Neck-in decreases as the heat transfer increases, due to the associated increase in viscosity and the corresponding increase in the film's resistance to changing geometry. An exception to this trend occurs at $\alpha = 5$ W/(m^2 K), for which the neck-in increases slightly compared with the isothermal simulation. The reason for this behaviour is unclear.

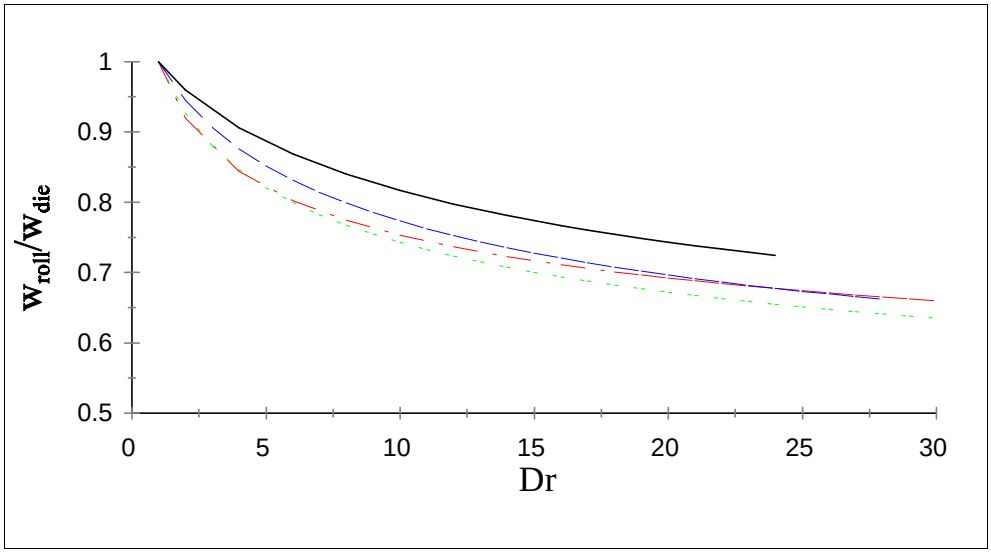

Figure 3.12 Neck-in ratio as a function of the draw ratio for $\alpha = 0$ (·–·), 5 (···), 10 (---), and 15 (––) W/(m^2 K)

The change in the velocity field as the heat transfer increases is seen from considering the streamlines at a draw ratio of 16 (Figure 3.13). With increasing α, there is a corresponding increase in the region in which u_1 is relatively independent of x_2, as shown by the parallel streamlines in Figure 3.13. Another observation from the streamline plots is that the free surface necks in more rapidly as the nonisothermal influence increases. This results because, as α increases the temperature decreases more

rapidly and there is an associated increase in viscosity for the same x_1 value. The increase in downstream viscosity results in the film changing geometry upstream, where the viscosity is relatively low.

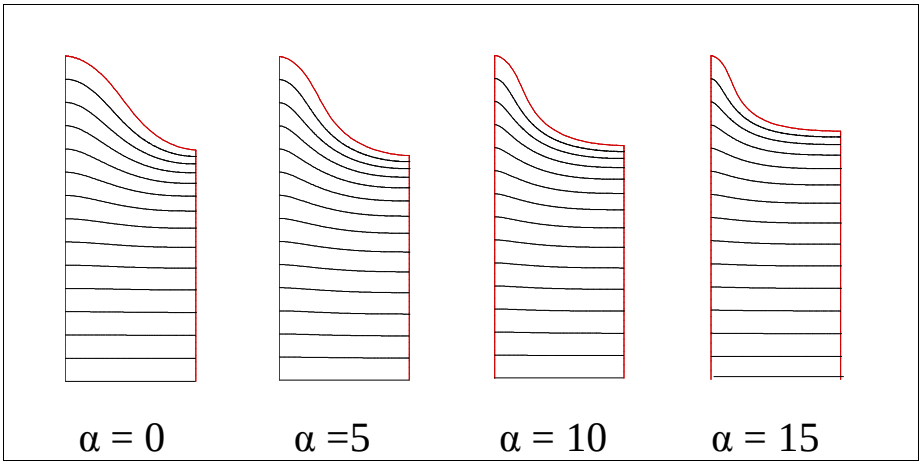

Figure 3.13 Streamlines for five values of the heat transfer coefficient with a draw ratio of 16

Figure 3.14 shows the thickness contours that correspond to the above streamlines. With larger heat transfer the thickness draws down more rapidly and the edge bead becomes more prominent. Once again this is due to the increase in resistance to changes in geometry as the viscosity increases. The thickness contour plots show that increases in heat transfer promote a more uniform thickness in the middle of the film. This is suggested by the overall straightness of the contours over the middle of the film and the sharp bend as the edge is approached.

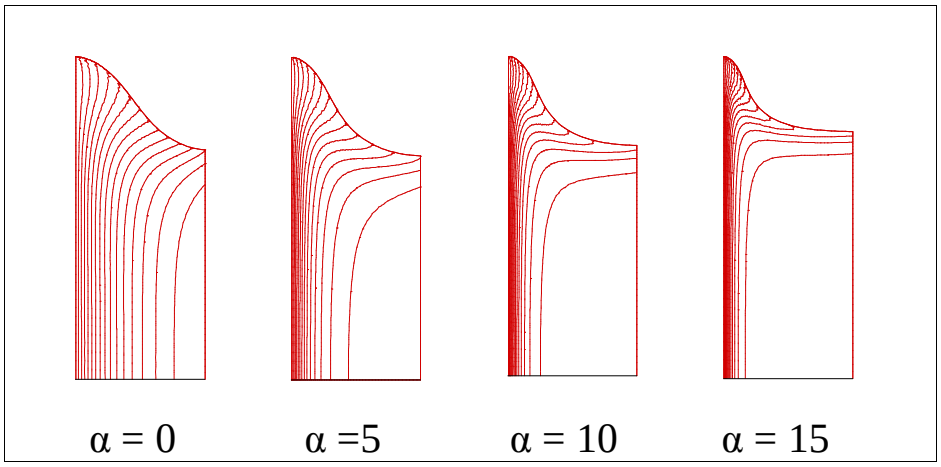

Figure 3.14 Thickness contours for five values of the heat transfer coefficient with a draw ratio of 16

Figure 3.14 suggests that the film has a more uniform thickness in the centre of the film when the heat transfer is greater. This is also shown by looking at the thickness profile at the chill roll, which is shown in Figure 3.15. For a draw ratio of 4 and 16, an increase in heat transfer extends the region of close to uniform thickness that exists in the middle of the sheet. The slope of the film's thickness profile also shows a change in sign at the edge. This edge effect has been observed in other studies (Debbaut et al. 1995).

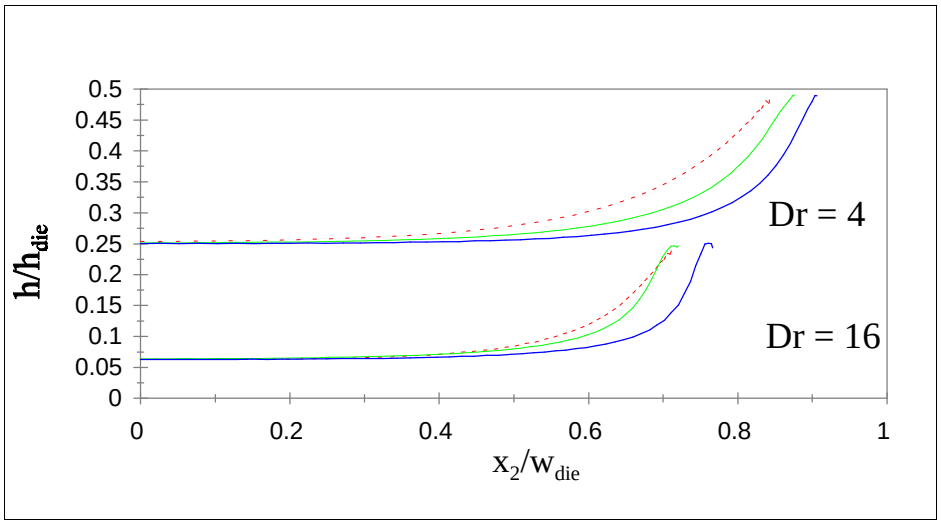

Figure 3.15 Thickness profiles at the chill roll for α = 0 (···), 10 (---), and 15 (–-) W/(m^2 K).

The thickness field of Figure 3.14 strongly influences the temperature field, for which contour lines are shown in Figure 3.16. This is shown by the correspondence of the temperature peak and the edge bead region. With the greater thickness here, heat transfer by advection increases relative to the surrounding film, and thus the temperature decreases less at the edge bead. Over the rest of the domain, the temperature follows an approximately linear trend from the die to the roll, as evident from the parallel, evenly spaced contour lines.

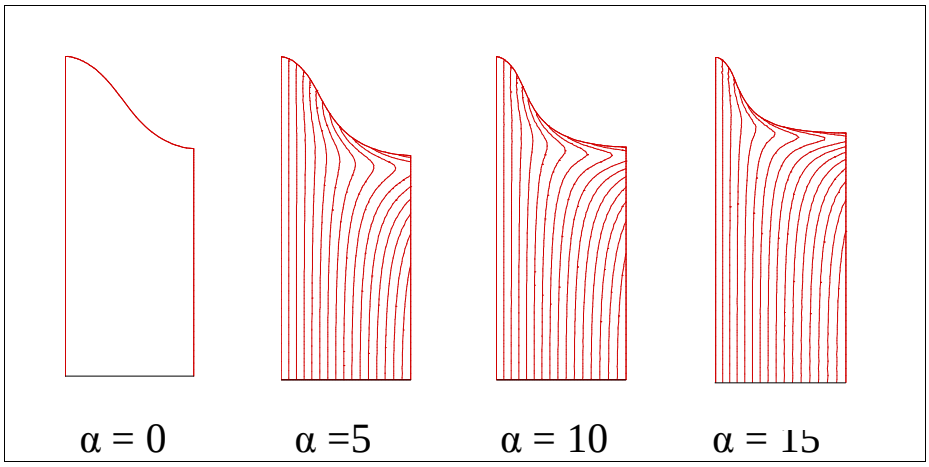

Figure 3.16 Temperature contours for five values of the heat transfer coefficient with a draw ratio of 16.

3.5 Performance of Model with Nontrivial Boundary Conditions and Heat Transfer

In the published research to date, the inlet conditions have been considered as constant along the die and the heat transfer coefficient has been assumed constant in the transverse direction. This section considers simulations that do not make these simplifying assumptions. The intention here is to demonstrate the usefulness of the numerical model for considering the possible effects associated with changing the manufacturing process.

3.5.1 Boundary Conditions at the Die

Although film casting dies are usually designed to extrude a uniform thickness, a nonconstant thickness is possible. This section briefly investigates how a nonuniform thickness at the die effects the thickness field. To do this, a simulation was conducted

excluding heat transfer, accommodating a nonuniform thickness at the die and retaining the remaining processing conditions of Section 3.4.2. The boundary condition for the thickness at the die was set using the following equation:

$$h_{die}(x_2) = h_{sym} - 0.002x_2^2 \quad \textbf{(3.16)}$$

in which h_{sym} is the thickness at the line of symmetry. In the simulation h_{sym} = 0.001 m, the value previously used across the entire width of the die. Equation 3.16 then, represents an inverse parabolic thickness profile that decreases to half the value of h_{sym} at the edge of the sheet. This profile was selected in an attempt to compensate for the tendency of the film, once outside the die, to increase in thickness as the edge is approached.

Figure 3.17 shows the thickness contours for the nonconstant thickness and for the corresponding constant thickness at a draw ratio of 16. The two show different behaviour near the die as anticipated, but the contours are similar as the roll is approached. However, the nonconstant thickness solution shows a smaller edge bead with a more rounded shape.

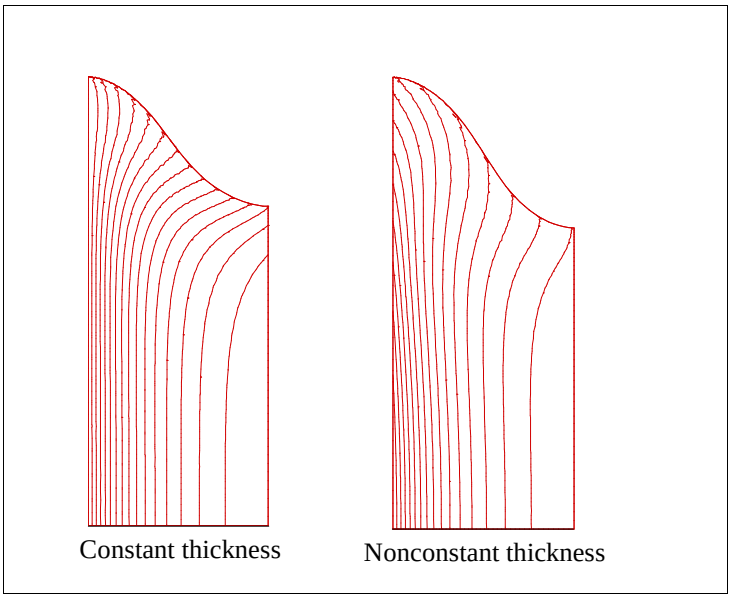

Figure 3.17 Thickness contours for nonconstant and constant thickness at the die with a draw ratio of 16

Although the nonconstant thickness boundary-valued problem changes the thickness field from the constant thickness problem, it is unclear at this time how this behaviour can be used to reduce neck-in and increase the region of uniform thickness. In fact, neck-in is slightly increased and the region of uniform thickness changes little between the two simulations. This is shown by considering the thickness profile at the die for the two cases (Figure 3.18). Neck-in is likely greater for the nonconstant thickness simulation because the edge bead is smaller and thus has less of a restraining influence. The more rounded edge bead for the nonconstant thickness simulation is also shown by Figure 3.18. It should be noted that differences in the two simulations could be attributed to the fact that the mass flux is less for the nonuniform thickness problem.

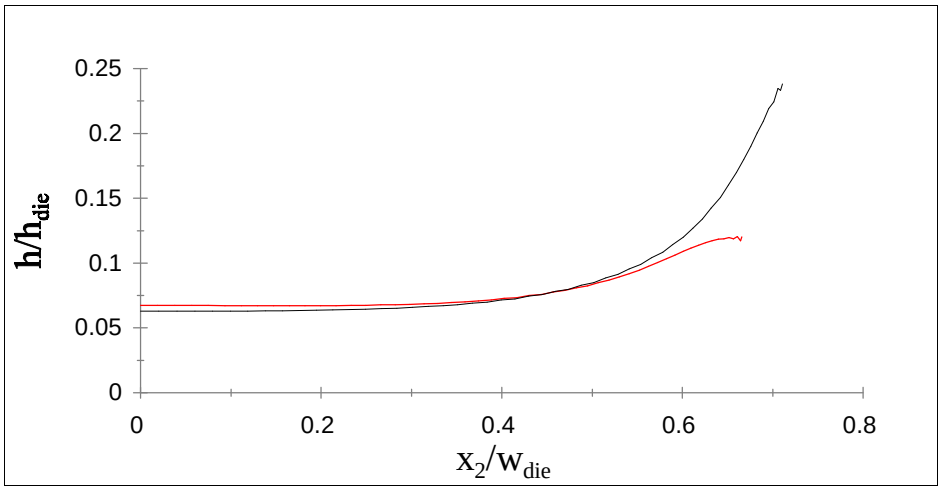

Figure 3.18 Thickness profiles at the chill roll for nonconstant (–-) and constant (---) thickness at the die with a draw ratio of 16

Although the observations may not be considered conclusive, as only one simulation was presented, it is possible that changing the die geometry could aid in reducing neck-in and promoting a more uniform thickness. To investigate this possibility a more comprehensive study should follow that addresses the effects of different die lip geometries, different mass fluxes, and nonisothermal conditions. These other factors are not considered here, as a more robust model that includes elasticity would make the results more meaningful.

3.5.2 Localized Cooling Jets

Often in film casting localized cooling jets are directed at the edges of the film to reduce tearing problems. To see the influence of these jets on the thickness field a simulation was performed using the processing conditions defined in Section 3.4.2, with

α = 10 W/(m^2 K) over the surface and α = 20 W/(m^2 K) over approximately 7 cm of the film's edge.

Localized cooling jets directed at the edge of the film significantly reduced neck-in, as shown by Figure 3.19. Moreover, the film did not neck-in as rapidly with increasing draw ratio when the jets were present. The neck-in was reduced because the cooling jets increase the viscosity at the edge of the sheet, thereby reinforcing it in the transverse direction.

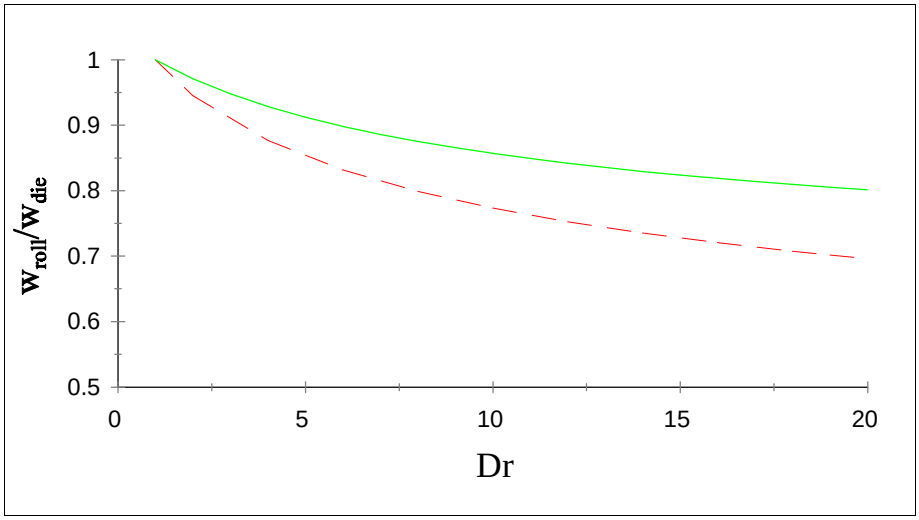

Figure 3.19 Neck-in ratio as a function of the draw ratio with localized cooling (––) and without (···).

Another advantage of a localized cooling jet is that it leads to a more uniform thickness in the centre of the film. This influence is demonstrated by the thickness profile at the chill roll shown in Figure 3.20. Therefore, localized cooling jets for LDPE film casting benefit the finished product by leading to a uniform thickness, resulting in less neck-in, and by reducing tearing problems.

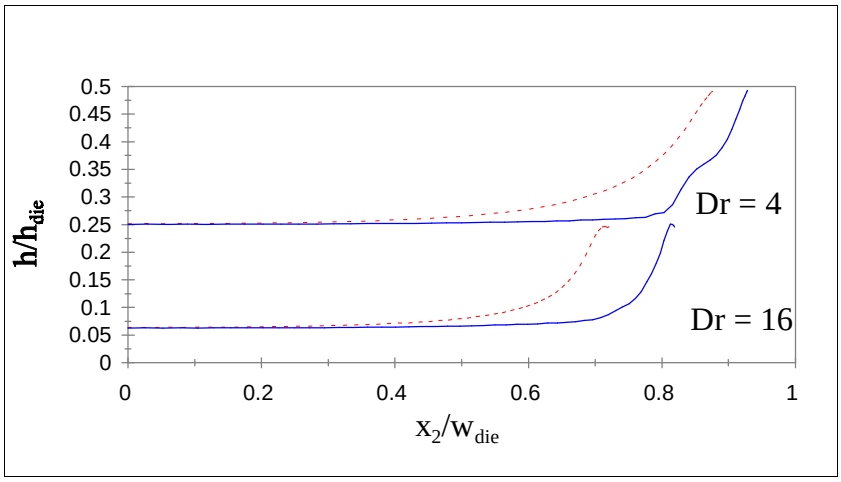

Figure 3.20 Thickness profile at the chill roll with localized cooling (—) and without (···).

3.6 Summary of Results

The 2D isothermal and nonisothermal simulations of this chapter have resulted in nine major findings:

i) The free surface found using the numerical algorithm developed in this research is curved, not linear as found by Sergent's closed-form solution.

ii) As the draw ratio is varied, the numerical solution agrees with the closed-form solution for force and follows the same trend for the neck-in ratio and the thickness reduction.

iii) Isothermal film casting simulations have a roughly U-shaped thickness profile across the film. An edge bead is present, but the cross-section does not show a region of uniform thickness in the middle of the sheet.

iv) The 2D isothermal simulations of this study agree well with the 3D simulation of Sakaki et al. (1996); however this study does not agree with the 2D simulation of d'Halewyu et al. (1990).

v) In the current study, a constant heat transfer was applied to both sides of the film. This leads to similar average temperature predictions as the more complex model of Barq et al. (1992).

vi) For low viscosity polymers the self-weight of the sheet can be used to promote a uniform thickness in the middle of the film. In addition, self-weight can reduce neck-in.

vii) Higher heat transfer can reduce neck-in and increase the zone of constant thickness at the centre of the film.

viii) Although a nonuniform thickness profile at the die alters the flow field, how this can be used to reduce neck-in and increase the uniformity of the final film thickness is unclear.

ix) The introduction of local cooling jets dramatically reduces neck-in and increases the region of uniform thickness.

For efficient film casting, neck-in should be limited and the region of uniform thickness should extend over most of the width of the sheet. The simulations of this chapter suggest that both goals can be promoted by the self-weight of the film, nonisothermal conditions, localized cooling jets and nonuniform boundary conditions at the die.

Chapter 4 Conclusions and Recommendations

This thesis presented finite element models for 1D and 2D nonisothermal film casting of a viscous fluid. The models neglect sag and die swell, but are capable of including the effects of gravity and inertia. For the 2D case, the model allows the thickness to vary in the transverse direction. A numerical solution to the finite element equations is obtained by using a fully coupled Newton-Raphson approach. Solutions were found for different polymers and processing conditions to determine how neck-in and edge beads were affected by the following factors: nonisothermal conditions; the self-weight of the film; and nonconstant boundary conditions at the die. Also of interest was determining whether the geometry of a film changes after it makes contact with the chill roll.

The conclusions made from the 1D and 2D film casting simulations of Chapters 2 and 3, respectively, are summarized in Section 4.1. Section 4.2 provides recommendations for future work that include, collecting more experimental data; improving the mathematical model; enhancing the numerical algorithm and shifting focus from analysis to design. A concluding statement is provided in Section 4.3.

4.1 Conclusions

From the 1D simulations and the discussion of Chapter 2 the following conclusions were made:

i) Inertia and gravity are only important for low viscosity polymers.

ii) Upwinding is not necessary for predicting the temperature distribution of the film.

iii) Once contact is made with the chill roll, the geometry of the film remains essentially unchanged; therefore, a model of the film casting process does not have to extend onto the roll.

iv) As the heat transfer coefficient increases, the temperature decreases more rapidly, and thus the viscosity increases at a quicker rate. This results in the velocity and thickness more rapidly approaching their final values.

v) The temperature of the film in the air gap is well approximated by a linear function.

vi) A closed-form solution for the nonisothermal velocity distribution, based on the assumption of a linear temperature profile, compares well against simulated results.

vii) The influence of the temperature sensitivity parameter in the temperature-viscosity relation is similar to that of the heat transfer coefficient. Furthermore, the solution changes very little when the temperature-viscosity relation is modified to account for an increase in viscosity as the solidification temperature is approached.

viii) Simulated results for temperature compared well with the experimental data of Kase (1974).

ix) Simulated results for thickness did not compare as well with the experimental data of Kase (1974), possibly because of experimental error in the data, uncertainty in the material parameters or the influence of viscoelasticity, which is neglected in the current model.

The above conclusions, made from the 1D simulations, led to several decisions when proceeding to the 2D case, such as, only modelling the film in the air gap; excluding upwinding; not using the more complex viscosity-temperature relationship; and using the closed-form 1D solutions as an initial guess for the 2D field variables. The 2D simulations in turn led to several conclusions:

i) When comparing the numerical results with the closed-form solution of Sergent (1977) several observations were made: the free surface was found to be curved, not linear; the thickness profile was U-shaped, not uniform; the forces were approximately equal; a greater decrease occurred in the thickness; and a lesser decrease occurred in the width at the roll.

ii) A simulated thickness profile at the chill roll using the approach of this study agreed with the results of Sakaki et al. (1996), but neither the current study nor Sakaki et al. (1996) agreed with d'Halewyu et al. (1990).

iii) The self-weight of the polymer for low viscosity fluids contributes to reducing neck-in and increasing the region of uniform thickness in the centre of the sheet.

iv) For some combinations of polymer and processing conditions, such as that described by Barq et al. (1992) for PET, the isothermal and nonisothermal results are essentially identical.

v) A simple thermal model with a constant heat transfer coefficient seems to predict the temperature distribution as well as a more complex model.

vi) For those processes that are temperature dependent, an increase in heat transfer was found to reduce neck-in and enlarge the region of uniform thickness.

vii) Although a nonuniform thickness at the die influences the final film geometry, it is unclear at this time how this can be used to reduce neck-in and to decrease the width of the edge bead.

viii) Localized cooling jets can be used to reduce neck-in and promote a uniform thickness in the centre of the sheet.

Cast film line designers attempt to waste as little material as possible. This is reflected in the goals of limiting neck-in and in reducing the amount of edge bead that has to be trimmed. It has been found that polymers that are more elastic tend to towards these goals (Debbaut et al. 1995; Christodoulou 1996). However, elasticity is not helpful for some polymers, such as PET, which behave viscously. The simulations of this study suggest that other phenomena can contribute to the above design goals. For one, cooling the film may reduce neck-in and increase the uniform thickness zone, especially if localized cooling is employed. Another factor that can be helpful, when the viscosity of the polymer is not overly temperature dependent, is the self-weight of the polymer. For

low viscosity polymers the self-weight of the film can contribute to reducing the quantity of wasted material by reducing neck-in and promoting a uniform thickness.

4.2 Recommendations for Future Work

Although useful insights into the film casting process can be gained from the model developed in this thesis, future work is required to increase the robustness of the model and improve its quantitative predictive power. This section details some potential approaches for continuing the cast film research.

4.2.1 More Experimental Data

Currently, little experimental data are available for testing and calibrating numerical simulations. This is shown by the limited number of studies listed in Section 1.2.3. These studies cover only a small portion of the wide range of polymers and processing conditions used in industrial film casting. Moreover, they only include data for a few variables. Data are needed for a wide range of polymers and processing conditions. The polymers should have different rheological properties, especially viscosities and relaxation times, and the processing conditions should have different heat transfers, mass fluxes, draw ratios, air gap lengths, die widths etc. From the experiments, the data of primary interest would be the thickness and temperature fields, heat transfer coefficients, the rheological characteristics of the material, and a complete description of the boundary conditions. Once more data are available, cast film research will be better able to relate finished film properties to the material and to the processing conditions employed.

4.2.2 Improve Mathematical Model

To improve the mathematical model of the film casting process the assumptions made in the derivations of the governing equations could be altered. For example, die swell, sag, surface tension and air drag could be added to the model. In addition, the heat transfer mechanism could be improved to accommodate radiation, crystallization, local heat transfer, and different rates of heat transfer from each side of the film. The most significant assumption that could be removed is the simple constitutive law currently used. As a first step toward addressing more realistic polymer behaviour a power-law model for viscosity could be implemented. A more ambitious goal would be to use a viscoelastic constitutive equation. In selecting a specific constitutive law many types of differential and integral laws are available, but Tanner (1985: 223) suggests that for mainly extensional flows, like film casting, the K-BKZ integral constitutive equation (Bernstein et al. 1963) performs best.

4.2.3 Enhance Numerical Algorithm

Three recommendations can be made for enhancing the numerical algorithm:

i) Increase the order of interpolation used by the finite elements from linear to quartic. If 15-noded elements are used instead of the 3-noded elements then the large number of elements needed could be reduced. However, this would involve a tradeoff in that the local stiffness matrix size would be increased.

ii) Although the numerical algorithm presented in this thesis converges to a solution, the possibility exists that it is a nonunique solution. This possibility is highlighted by the different solutions found by the current study and by d'Halewyu et al.

(1990). To investigate whether the solution is nonunique, the algorithm could be modified to use a pseudo-time stepping algorithm to approach the steady-state solution gradually.

iii) If the mathematical model is modified to include viscoelasticity then the numerical algorithm should be changed to accommodate this. Methods of handling viscoelasticity have been proposed for differential constitutive equations (Lou and Tanner 1986; Marchal and Crochet 1987; Sun et al. 1996) and for integral constitutive equations (Dupont et al. 1985; Lou and Tanner 1986; Lou and Mitsoulis 1990). All these methods use an Eulerian or spatial framework, like that adopted in the current study. An alternative approach, which would allow easier handling of the constitutive law, would be to adopt a Lagrangian or material description of the motion. Another option is Arbitrary Lagrangian-Eulerian (ALE) finite elements, which have been used for other studies of continuous media (Liu et al. 1988; Huétink and van der Helm 1992).

4.2.4 Change of Focus from Analysis to Design

The current study has focused on analyzing a given film casting problem. For the future, a shift in focus to design would be helpful. A computer program would be a powerful tool if it could provide an optimal film line design, given a set of objectives and the appropriate data. This would certainly involve optimization algorithms, which would quantify the trade-offs between edge-bead size and neck-in. Furthermore, a knowledge base of design heuristics would be required. This could possibly be handled by using an

expert system. If a package such as this could be created then theoretical modelling would take a large step toward being integrated into the design process for film lines.

4.3 Concluding Statement

This thesis provided several insights into some special cases of film casting, such as the casting of low elasticity melts. Moreover, this thesis has provided a framework for building a more robust model, one that can handle a larger range of polymers and processing conditions. In building on the current research, a more robust model would benefit from future film casting studies that increase the experimental data, improve the mathematical model, enhance the numerical algorithm and shift the focus from analysis to design. These future research contributions will move theoretical modelling closer to being an integrated part of the film line design process. In addition, the theoretical tools could aid in diagnosing problems as they occur on film lines. As the theory becomes more advanced, cast film line designers will be able to produce more efficient designs, in less time and using less material, which means the economic and environmental benefits outlined at the start of this thesis could eventually be realized.

References

Acierno, D., La Mantia, F. P. and Titomanlio, G., (1976), Model Analysis of Uniaxial and Biaxial Stretching of Polymer Melts, *Rheologica Acta*, 15: pp642-647.

Adachi, K., Aoki, T., Nishida, S. and Nakamura, R., (1988), A Hydrodynamic Investigation of a Falling Liquid Film for Curtain Coating and Sheet Casting, *Xth International Congress on Rheology*, Australian Society of Rheology, Sydney: pp122-124.

Agassant, J. F., Avenas, P., Sergent, J. P. and Carreau, P. J., (1991), *Polymer Processing. Principles and Modeling*, Hanser Publishers, Munich; Vienna and New York.

Aird, G. R. and Yeow, Y. L., (1983), Stability of Film Casting of Power-Law Liquids, *Industrial Engineering Chemical Fundamentals*, 22: pp7-10.

Alaie, S. M. and Papanastasiou, T. C., (1991), Film Casting of Viscoelastic Liquid, *Polymer Engineering and Science*, 31, 2: pp67-75.

Anturkar, N. R. and Co, A., (1988), Draw Resonance in Film Casting of Viscoelastic Fluids: a Linear Stability Analysis, *Journal of Non-Newtonian Fluid Mechanics*, 28: pp287-307.

Avenas, P., Agassant, J. F. and Sergent, J. Ph., (1986), *La mise en forme des matières plastiques. Technique et Documentation*, 2 ed., Lavoisier, Paris.

Baird, D. G. and Collias, D. I., (1995), *Postdie Processing in Polymer Processing: Principles and Design*, Butterworth-Heinemann, Boston.

Barq, P., Haudin, J. M., Agassant, J. F., Roth, H. and Bourgin, P., (1990), Instability Phenomena in Film Casting Process, *International Polymer Processing*, V, 4: pp264-271.

Barq, P., Haudin, J. M. and Agassant, J. F., (1992), Isothermal and Anisothermal Models for Cast Film Extrusion, *International Polymer Processing*, VII, 4: pp334-349.

Bejan, A., (1984), *Convection Heat Transfer*, John Wiley & Sons, New York.

Bergonzoni, A. and DiCresce, A. J., (1966), The Phenomenon of Draw Resonance in Polymeric Melts, *Polymer Engineering and Science*, January: pp45-59.

Bernstein, B., Kearsley, E. A. and Zapas, L. J., (1963), A Study of Stress Relaxation with Finite Strain, *Transactions of the Society of Rheology*, VII: pp391-410.

Billon, N., Barq, P. and Haudin, J. M., (1991), Modelling of the Cooling of Semi-crystalline Polymers during their Processing, *International Polymer Processing*, VI, 4: pp348-355.

Brown, D. R., (1961), A Study of the Behaviour of a Thin Sheet of Moving Liquid, *Journal of Fluid Mechanics*, 10: pp297-305.

Carslaw, H. S. and Jaeger, J. C., (1959), *Conduction of Heat in Solids*, Clarendon Press, Oxford.

Chambon, F., Ohlsson, S. and Silagy, D., (1996), Validation of a Model for the Cast-Film Process, *First Joint Topical Conference on Processing, Structure and Properties of Polymeric Materials, Conference Preprint*, American Institute of Chemical Engineers, New York, New York: pp39-42.

Christie, I., Griffiths, D. F., Mitchell, A. R. and Zienkiewicz, O. C., (1976), Finite Element Methods for Second Order Differential Equations with Significant First Derivatives, *International Journal for Numerical Methods in Engineering*, 10: pp1389-1396.

Christodoulou, K. N., (1996), Finite Element Analysis of Thickness Nonuniformity, Instabilities, and Orientation Development in Casting and Stretching of Viscoelastic Films, *First Joint Topical Conference on Processing, Structure and Properties of Polymeric Materials, Conference Preprint*, American Institute of Chemical Engineers, New York, New York: pp43-45.

Clarke, N. S., (1966), A Differential Equation in Fluid Mechanics, *Mathematika*, 12: pp51-53.

Conte, S. D. and deBoor, C., (1980), *Elementary Numerical Analysis An Algorithmic Approach*, 3 ed., McGraw-Hill Book Company, New York.

Cotto, D., Duffo, P. and Haudin, J. M., (1989), Cast Film Extrusion of Polypropylene Films, *International Polymer Processing*, IV, 2: pp103-113.

Cotto, D. and Haudin, J. M., (1988), Étude de la Cristallisation dans la Mise en Forme des Polymères Application à l'extrusion de films de polypropylène, *Matériaux et Techniques*, 6: pp9-16.

d'Halewyu, S., Agassant, J. F. and Demay, Y., (1990), Numerical Simulation of the Cast Film Process, *Polymer Engineering and Science*, 20, 6: pp335-340.

Debbaut, B. and Marchal, J. M., (1995), Viscoelastic effects in film casting in *Zeitschrift fur Angewandte Mathematik und Physick Special Issue*, Casey J. and Crochet M. J. (eds.), Birkhäuser Verlag, Boston, 46: ppS679-S698.

deGroot, J. A., Doughty, A. T. and Stewart, K. B., (1993), Effects of Cast Film Fabrication Variables on Key Stretch Film Properties, *Tappi Journal*, 76, 6: pp161-166.

Denn, M. M., (1980), Continuous Drawing of Liquids to Form Fibers, *Annual Review of Fluid Mechanics*, 12: pp365-387.

Dobroth, T. and Erwin, L., (1986), Causes of Edge Beads in Cast Films, *Polymer Engineering and Science*, 26, 7: pp462-467.

Duffo, P., Monasse, B. and Haudin, J. M., (1991), Cast Film Extrusion of Polypropylene. Themomechanical and Physical Aspects, *Journal of Polymer Engineering*, 10, 1-3: pp151-228.

Dupont, S., Marchal, J. M. and Crochet, M. J., (1985), Finite Element Simulation of Viscoelastic Fluids of the Integral Type, *Journal of Non-Newtonian Fluid Mechanics*, 17: pp157-183.

Flanagan, J. L., (1993), Better Die Design and Equipment Enhance the Cast Film Process, *Modern Plastics*, 70, Feb: pp53+.

Gabriele, M. C., (1996), Systems Innovation Helps Drive Cast Film Growth, *Modern Plastics*, 73, Sept: pp62-63+.

Huétink, J. and van der Helm, P. N., (1992), On Euler-Lagrange Finite Element Formulation in Forming and Fluid Problems, *International Conference on Numerical Methods in Industrial Forming Processes, 4th*, Chenot, Wood & Zienkiewicz (eds.), Balkema, Rotterdam. pp45-54.

Hughes, T. J. R., (1978), A Simple Scheme for Developing 'Upwind' Finite Elements, *International Journal for Numerical Methods in Engineering*, 12: pp1359-1365.

Incropera, F. P. and DeWitt, D. P., (1985), *Fundamentals of Heat and Mass*

Transfer, 2 ed., John Wiley & Sons, United States.

Iyengar, V. R. and Co, A., (1993), Film Casting of a Modified Giesekus Fluid: a Steady-State Analysis, *Journal of Non-Newtonian Fluid Mechanics*, 48: pp1-20.

Iyengar, V. R. and Co, A., (1996), Film Casting of a Modified Giesekus Fluid: Stability Analysis, *Chemical Engineering Science*, 51, 9: pp1417-1430.

Kase, S., (1974), Studies on Melt Spinning. IV. On the Stability of Melt Spinning, *Journal of Applied Polymer Science*, 18: pp3279-3304.

Keller, R., (1989), Comparing the Cast Film and Blown Film Processes, *Plastics Engineering*, 45, Aug: pp31-34.

Kistler, S. F. and Scriven, L. E., (1983), Coating Flows in *Computational Analysis of Polymer Processing*, J. R. A. Pearson and S. M. Richardson (eds), Applied Science Publishers Ltd., London and New York, pp243-297.

Kreisher, K. R., (1993), Downstream Innovations Increase Cast-Film Speed, *Modern Plastics*, 70, May: pp48-49+.

Lee, W. K., (1984), A Slit Die Design for Stable Film Extrusion, *Advances in Rheology*, International Congress on Rheology Mexico, Elsevier Science Publishing Company, New York, New York: pp473-481.

Liu, W. K., Chang, H., Chen, J., and Belytschko T., (1988), Arbitrary Lagrangian-Eulerian Petrov-Galerkin Finite Elements for Nonlinear Continua, *Computer Methods in Applied Mechanics and Engineering*, 68, pp259-310.

Luo, X. L. and Mitsoulis, E., (1990), An Efficient Algorithm for Strain History Tracking in Finite Element Computations of Non-Newtonian Fluids with Integral Constitutive Equations, *International Journal for Numerical Methods in Fluids*, 11: pp1015-1031.

Luo, X. L. and Tanner, R. I., (1986), A Streamline Element Scheme for Solving Viscoelastic Flow Problems. Part I. Differential Constitutive Equations, *Journal of Non-Newtonian Fluid Mechanics*, 21: pp179-199.

Luo, X. L. and Tanner, R. I., (1986), A Streamline Element Scheme for Solving Viscoelastic Flow Problems Part II: Integral Constitutive Equations, *Journal of Non-Newtonian Fluid Mechanics*, 22: pp61-89.

Marchal, J. M. and Crochet, M. J., (1987), A New Mixed Finite Element for Calculating Viscoelastic Flow, *Journal of Non-Newtonian Fluid Mechanics*, 26: pp77-114.

Mewis, J. and Petrie, C. J. S., (1986), Chapter 4 Hydrodynamics of Spinning Polymers in *Encyclopedia of Fluid Mechanics*, Volume 6, N. P. Cheremisinoff (ed.), Gulf Publishing, Houston, pp111-139.

Michaeli, W. and Menges, G., (1982), Calculation of Cooling Processes in Extrusion, *Polymer Engineering Reviews*, 2, 2: pp99-121.

Miller, R. K., (1987), *Introduction to Differential Equations*, Prentice-Hall, Inc., Englewood Cliffs, New Jersey.

Minoshima, W. and White, J. L., (1983), Stability of Continuous Film Extrusion Processes, *Polymer Engineering Reviews*, 2, 3: pp211-226.

Papanastasiou, T. C., Malamataris, N. and Ellwood, K., (1992), A New Outflow Boundary Condition, *International Journal for Numerical Methods in Fluids*, 14: pp587-608.

Park, C. W., (1991), A Study on Bicomponent Two-Layer Slot Cast Coextrusion, *Polymer Engineering and Science*, 31, 3: pp197-203.

Pearson, J. R. A., (1985), *Mechanics of Polymer Processing*, Elsevier Applied Science, London.

Pis-Lopez, M. E. and Co, A., (1996a), Multilayer Film Casting of Modified Giesekus fluids Part 1. Steady-state analysis, *Journal of Non-Newtonian Fluid Mechanics*, 66: pp71-93.

Pis-Lopez, M. E. and Co, A., (1996b), Multilayer Film Casting of Modified Giesekus fluids Part 2. Linear stability analysis, *Journal of Non-Newtonian Fluid Mechanics*, 66: pp95-114.

Rauwendaal, C., (1986), *Polymer Extrusion*, Macmillan Publishing Company, Inc., New York.

Sakaki, K., Katsumoto, R., Kajiwara, T. and Funatsu, K., (1996), Three-Dimensional Flow Simulation of a Film-Casting Process, *Polymer Engineering and Science*, 36, 3: pp1821-1831.

Sergent, J. P., (1977), *Etude de deux Procédés de Fabrication de Films. Le Soufflage de Gaine. L'extrusion de Film à Plat*, Thesis, Université Louis Pasteur, Strasbourg.

Sidiropoulos, V., (1995), *Comparison of Experiments with a Model of the Blown Film Process*, M. Eng. Thesis, McMaster University, Hamilton, ON.

Sidiropoulos, V., Tian, J. J. and Vlachopoulos, J., (1996), Computer Simulation of Film Blowing, *Tappi Journal*, 79, 8: pp113-118.

Silagy, D., Demay, Y. and Agassant, J. F., (1996a), Study of the Stability of the Film Casting Process, *Polymer Engineering and Science*, 36, 21: pp2614-2625.

Silagy, D., Demay, Y. and Agassant, J. F., (1996b), Étude de la stabilité linéaire de l'étirage d'un film newtonien, *Comptes Rendus de l'académie des Sciences*, 322, Série IIb, 4: pp283-289.

Sun, J., Phan-Thien, N. and Tanner, R. I., (1996), An Adaptive Viscoelastic Stress Splitting Scheme and its Applications: AVSS/SI and AVSS/SUPG, *Journal of Non-Newtonian Fluid Mechanics*, 65: pp75-91.

Tanner, R. I., (1985), *Engineering Rheology*, 2 ed., Clarendon Press, Oxford.

White, J. L., (1975), Theoretical Considerations of Biaxial Stretching of Viscoelastic Fluid Sheets with Application to Plastic Sheet Forming, *Rheologica Acta*, 14: pp600-611.

Wilder, R. V., (1991), Cast film or cast sheet? Machines can now do both, *Modern Plastics*, 68, Nov: pp54+.

Wineman, A. S., (1976), Large Axisymmetric Inflation of a Nonlinear Viscoelastic Membrane by Lateral Pressure, *Transactions of the Society of Rheology*, 20, 2: pp203-225.

Yeow, Y. L., (1974), On the Stability of Extending Films: a Model for the Film Casting Process, *Journal of Fluid Mechanics*, 66, part 3: pp613-622.

Appendix A Closed-Form Solutions

A.1 Derivation of the Solution for 1D Isothermal Film Casting Neglecting Gravity

The governing equations from Section 2.1.1 are as follows:

$$\begin{aligned} \frac{d(h\sigma_{11})}{dx_1} &= 0 \\ \frac{d(hu_1)}{dx_1} &= 0 \\ \sigma_{11} &= 4\eta\frac{du_1}{dx_1} \end{aligned} \qquad \textbf{(A.1)}$$

The associated boundary conditions are:

$$\begin{aligned} &At\ x_1 = 0 \qquad u_1 = u_{die}\ and\ h = h_{die} \\ &At\ x_1 = L \qquad u_1 = u_{roll} \end{aligned} \qquad \textbf{(A.2)}$$

Integration of Equations A.1a and A.1b yields

$$\begin{aligned} h\sigma_{11} &= F \\ hu_1 &= Q \end{aligned} \qquad \textbf{(A.3)}$$

Where F represents the force per unit width and Q is the volume flux per unit width.

Now Equations A.1c and A.3b are substituted into Equation A.3a:

$$4\eta\frac{Q}{u_1}\frac{du_1}{dx_1} = F$$
$$\frac{1}{u_1}\frac{du_1}{dx_1} = \frac{F}{4\eta Q} = C_1 \qquad \textbf{(A.4)}$$
$$\frac{du_1}{u_1} = C_1 dx_1$$

Now both sides of the resulting equation are integrated as follows:

$$\int_{u_{die}}^{u_1}\frac{d\hat{u}_1}{\hat{u}_1} = \int_0^{x_1} C_1 d\hat{x}_1$$
$$\ln u_1 - \ln u_{die} = C_1 x_1 \qquad \textbf{(A.5)}$$
$$\frac{u_1}{u_{die}} = e^{C_1 x_1}$$

Applying the boundary condition for velocity at $x_1 = L$, the theoretical velocity profile is found:

$$\frac{u_{roll}}{u_{die}} = e^{C_1 L} = Dr$$
$$\therefore \quad u_1 = u_{die} e^{C_1 L \frac{x_1}{L}} = u_{die} Dr^{\frac{x_1}{L}} \qquad \textbf{(A.6)}$$

Substituting this result into Equation A.3b, the theoretical thickness profile is found:

$$h = h_{die} Dr^{-\frac{x_1}{L}} \qquad \textbf{(A.7)}$$

The gradients of velocity and thickness can be found from Equations A.6 and A.7, respectively:

$$\frac{du_1}{dx_1} = \frac{u_{die}}{L}\ln(Dr) Dr^{\frac{x_1}{L}}$$
$$\frac{dh}{dx_1} = -\frac{h_{die}}{L}\ln(Dr) Dr^{-\frac{x_1}{L}} \qquad \textbf{(A.8)}$$

A.2 Temperature Distribution in a Moving Sheet

The differential equation describing the thermal energy conservation for a sheet moving with a constant velocity (u_1), which is losing heat by Newton's law of cooling into a medium with a temperature of zero is:

$$\kappa \frac{d^2T}{dx_1^2} - u_1 \frac{dT}{dx_1} - \theta T = 0 \qquad where\ \kappa = \frac{k}{\rho C}\ and\ \theta = \frac{2\alpha}{\rho C h} \qquad \textbf{(A.9)}$$

Where κ is the thermal diffusivity, T is the temperature, k is the thermal conductivity, ρ is the density, C is the specific heat capacity, α is the one sided heat transfer coefficient and h is the thickness. The solution to this differential equation is found in Carslaw and Jaeger (1959: 148) for two different boundary conditions:

i) For an infinite sheet in the x_1-direction with $T = T_{die}$ at $x_1 = 0$

$$T = T_{die} \exp\left(\frac{u_1 - \sqrt{(u_1^2 + 4\kappa\theta)}}{2\kappa} x_1 \right) \qquad \textbf{(A.10)}$$

ii) For an infinite sheet in the x_1-direction with $T = T_{die}$ at $x_1 = 0$ and $T = T_{roll}$ at $x_1 = L$

$$T = \frac{T_{roll} e^{\frac{-u_1(L-x_1)}{2\kappa}} \sinh(\xi x_1) + T_{die} e^{\frac{u_1 x_1}{2\kappa}} \sinh(\xi(L-x_1))}{\sinh(\xi L)} \qquad \textbf{(A.11)}$$

$$where\ \xi = \sqrt{\frac{u_1^2}{4\kappa^2} + \frac{2\alpha}{hk}}$$

A.3 Temperature Profile in a Moving Sheet without Conduction

The differential equation and boundary condition for energy conservation in a moving sheet with a thermal conductivity of zero are:

$$\rho C u_1 h \frac{dT}{dx_1} + 2\alpha(T - T_{air}) = 0 \qquad and\ T(0) = T_{die} \tag{A.12}$$

If the following substitution is used:

$$\begin{aligned} \hat{T} &= T - T_{air} \\ \frac{d\hat{T}}{dx_1} &= \frac{dT}{dx_1} \end{aligned} \tag{A.13}$$

then

$$\frac{d\hat{T}}{dx_1} = \frac{-2\alpha}{\rho C u_1 h}\hat{T} \qquad and\ \hat{T}(0) = \hat{T}_{die} = T_{die} - T_{air} \tag{A.14}$$

The solution of this differential equation using separation of variables is

$$\begin{aligned} \hat{T} &= \hat{T}_{die} e^{\frac{-2\alpha}{\rho C u_1 h} x_1} \\ T &= (T_{die} - T_{air}) e^{\frac{-2\alpha}{\rho C u_1 h} x_1} + T_{air} \end{aligned} \tag{A.15}$$

A.4 Velocity and Thickness Profiles assuming a Linear Temperature Distribution

The governing equations are:

$$\begin{aligned} \frac{d(h\sigma_{11})}{dx_1} &= 0 \\ \frac{d(hu_1)}{dx_1} &= 0 \\ \sigma_{11} &= 4\eta\frac{du_1}{dx_1} \\ \eta &= \eta_o e^{-a(T-T_o)} \\ T &= T_{die} - \frac{2\alpha(T_{die}-T_{air})}{\rho C u_1 h}x_1 \\ &= T_{die} - mx_1 \end{aligned} \qquad \textbf{(A.16)}$$

The associated boundary conditions are:

$$\begin{aligned} &At\ x_1 = 0 \qquad u_1 = u_{die}\ and\ h = h_{die} \\ &At\ x_1 = L \qquad u_1 = u_{roll} \end{aligned} \qquad \textbf{(A.17)}$$

Equations A.16a and A.16b are integrated to find the following:

$$\begin{aligned} h\sigma_{11} &= F \\ hu_1 &= Q \end{aligned} \qquad \textbf{(A.18)}$$

where F represents the force per unit width and Q is the volume flux per unit width. Now Equation A.16c and A.18b are substituted into Equation A.18a.

$$\begin{aligned} 4\eta\frac{Q}{u_1}\frac{du_1}{dx_1} &= F \\ \frac{du_1}{u_1} &= \frac{Fdx_1}{4\eta Q} \end{aligned} \qquad \textbf{(A.19)}$$

If the relations for viscosity and temperature are substituted into the above equation then

$$\frac{du_1}{u_1} = \frac{Fdx_1}{4\eta_o Qe^{-a(T_{die}-mx_1-T_o)}} = \frac{Fe^{a(T_{die}-T_o)}}{4\eta_o Q}e^{-amx_1}dx_1 = C_1 e^{-amx_1}dx_1 \quad \textbf{(A.20)}$$

where C_1 is a constant that simplifies the expression. Now both sides of the previous equation can be integrated to obtain

$$\begin{aligned} \int_{u_{die}}^{u_1} \frac{d\hat{u}_1}{\hat{u}_1} &= \int_0^{x_1} C_1 e^{-am\hat{x}_1} d\hat{x}_1 \\ \ln u_1 - \ln u_{die} &= \frac{C_1}{am}(1 - e^{-amx_1}) \\ \ln\left(\frac{u_1}{u_{die}}\right) &= C_2(1 - e^{-amx_1}) \end{aligned} \quad \textbf{(A.21)}$$

where $C_2 = C_1/am$. Applying the exponential function to both sides of the equation yields:

$$u_1 = u_{die}\exp(C_2(1 - e^{-amx_1}) \quad \textbf{(A.22)}$$

For $x_1 = L$

$$\begin{aligned} \frac{u_{roll}}{u_{die}} &= \exp(C_2(1 - e^{-amL})) = Dr \\ \therefore \quad \ln\left(\frac{u_{roll}}{u_{die}}\right) &= \ln Dr = C_2(1 - e^{-amL}) \\ \therefore \quad C_2 &= \frac{\ln Dr}{1 - e^{-amL}} \end{aligned} \quad \textbf{(A.23)}$$

C_2 can be substituted into Equation A.22 for the solution:

$$\begin{aligned} u_1 &= u_{die}\exp\left(\ln Dr \frac{1 - e^{-amx_1}}{1 - e^{-amL}}\right) \\ u_1 &= u_{die} Dr^{\left(\frac{1 - e^{-amx_1}}{1 - e^{-amL}}\right)} \end{aligned} \quad \textbf{(A.24)}$$

The above solution approaches the isothermal solution as “am” approaches zero. Substituting the velocity into Equation A.18b and using the boundary condition that Q = $u_{die}h_{die}$, the theoretical thickness profile is found:

$$h = h_{die}Dr^{-\left(\frac{1-e^{-amx_1}}{1-e^{-amL}}\right)} \qquad \textbf{(A.25)}$$

A.5 Velocity Profile for a Viscous Fluid Falling from Rest under its Own Weight

Brown (1961) derives a non-dimensional differential equation for the velocity of a thin film of viscous liquid falling under its own self weight:

$$\frac{d}{dX}\left(\frac{1}{U}\frac{dU}{dX}\right) + \frac{1}{U} - \frac{dU}{dX} = 0 \qquad \textbf{(A.26)}$$

Where U is the dimensionless velocity and X is the dimensionless distance along the direction of flow. The actual velocity (u_1) and distance (x_1) are related to the dimensionless values by:

$$u_1 = \left(\frac{4\eta g}{\rho}\right)^{\frac{1}{3}} U, \qquad x_1 = \left(\frac{4\eta}{\rho}\right)^{\frac{2}{3}} g^{-\frac{1}{3}} X \qquad \textbf{(A.27)}$$

Where η is the shear viscosity, g is the acceleration due to gravity and ρ is the density of the fluid.

The solution to this differential equation is found in Clarke (1966) for the boundary condition that U = 0 at X = 0:

$$U = \frac{2^{-\frac{1}{3}}(Ai(r))^2}{\left(\frac{dAi(r)}{dr}\right)^2 - r(Ai(r))^2} \qquad \textbf{(A.28)}$$

$$\text{where } r = 2^{-\frac{1}{3}}(X + k_o) \text{ and } k_o \simeq -2.94583$$

Where Ai is the Airy function, which is defined as (Miller 1987: 246, 249):

$$Ai(r) = C_1 y_1 - C_2 y_2 \qquad where\ C_1 \simeq 0.355028,\ C_2 \simeq 0.258819,$$

$$y_1(r) = 1 + \sum_{n=1}^{\infty} \frac{1 \cdot 4 \cdots (3n-2)}{(3n)!} r^{3n},\ and \tag{A.29}$$

$$y_2(r) = r + \sum_{n=1}^{\infty} \frac{1 \cdot 2 \cdots (3n-1)}{(3n+1)!} r^{3n+1}$$

A.6 Solution for 2D Film Casting when Thickness does not Vary Across the Width

Given the drawing force (F) in the film, Avenas et al. (1986: 359-369) and Agassant et al. (1991: 239-250) present relations to find the following variables: the draw ratio (u_{roll}/u_{die}), the neck-in (w_{roll}/w_{die}) and the thickness change (h_{roll}/h_{die}). The theoretical relations assume that the process is isothermal and that the fluid is Newtonian. Also, restrictions are made on the admissible velocity field: $u_1 = u_1(x_1)$, $u_2 = u_2(x_1, x_2)$ and $u_3 = u_3(x_1, x_3)$. This means that the film maintains a rectangular shape from the die to the roll, as the thickness does not vary in the transverse direction.

The neck-in at the roll is calculated from the following transcendental equation:

$$-4AL = (z_{roll} - z_{die}) + \ln\frac{z_{roll}-1}{z_{die}-1}$$
$$\text{where } A = \frac{F}{12\eta Q},\ Q = u_{die}h_{die}w_{die}, \qquad \textbf{(A.30)}$$
$$z_{roll} = \sqrt{1 + 8A^2w_{roll}^2},\ \text{and}\ z_{die} = \sqrt{1 + 8A^2w_{die}^2}$$

Once w_{roll}/w_{die} is known the following relation is used to solve for h_{roll}/h_{die}:

$$\ln\frac{w_{roll}}{w_{die}} + 2\ln\frac{h_{roll}}{h_{die}} = -6AL \qquad \textbf{(A.31)}$$

The continuity equation can then be used to determine the draw ratio (Dr):

$$Dr = \frac{u_{roll}}{u_{die}} = \frac{w_{die}h_{die}}{w_{roll}h_{roll}} \qquad \textbf{(A.32)}$$

In addition to the above relations, Avenas et al. (1986) and Agassant et al. (1991) present the theoretical limit for the neck-in:

$$\frac{w_{roll}}{w_{die}} = 1 - \sqrt{2}\frac{L}{w_{die}} \qquad \textbf{(A.33)}$$

Appendix B Derivation of the Tangential Stiffness Matrices

B.1 Derivation of the 1D Tangential Stiffness Matrix

This derivation is for a n-noded 1D element that has the same order of interpolation for all of the unknowns (u_1, h, and T). The finite element discretization is summarized as follows:

$$
\begin{aligned}
u_1 &= \boldsymbol{N}_u \boldsymbol{a},\ h = \boldsymbol{N}_h \boldsymbol{a},\ T = \boldsymbol{N}_T \boldsymbol{a}, \\
\frac{du_1}{dx_1} &= \boldsymbol{B}_u \boldsymbol{a},\ \frac{dh}{dx_1} = \boldsymbol{B}_h \boldsymbol{a},\ \frac{dT}{dx_1} = \boldsymbol{B}_T \boldsymbol{a} \\
\text{where } \boldsymbol{a} &= \left\langle u_{11}\ h_1\ T_1\ \cdots\ u_{1n}\ h_n\ T_n \right\rangle^T, \\
\boldsymbol{N}_u &= \left[N_1\ 0\ 0\ \cdots\ N_n\ 0\ 0 \right], \\
\boldsymbol{N}_h &= \left[0\ N_1\ 0\ \cdots\ 0\ N_n\ 0 \right], \\
\boldsymbol{N}_T &= \left[0\ 0\ N_1\ \cdots\ 0\ 0\ N_n \right], \\
\text{and } \boldsymbol{B}_u &= \frac{d\boldsymbol{N}_u}{dx_1},\ \boldsymbol{B}_h = \frac{d\boldsymbol{N}_h}{dx_1},\ \boldsymbol{B}_T = \frac{d\boldsymbol{N}_T}{dx_1}
\end{aligned}
\tag{B.1}
$$

where n is the number of degrees of freedom and u_{1i}, h_i, T_i and N_i are the velocity, thickness, temperature and shape function values for node i.

The finite element equations for equilibrium, continuity and the conservation of thermal energy can be expressed concisely as:

$$\begin{pmatrix} \mathbf{K}_{eqlb} \\ \mathbf{K}_{cont} \\ \mathbf{K}_{thrm} \end{pmatrix} \mathbf{a} = \begin{pmatrix} \mathbf{R}_{eqlb} \\ \mathbf{0} \\ \mathbf{R}_{thrm} \end{pmatrix} \qquad \textbf{(B.2)}$$

$$\text{where} \quad \begin{aligned} \mathbf{K}_{eqlb} &= \mathbf{K}_{grad} + \mathbf{K}_{inrt} \\ \mathbf{K}_{thrm} &= \mathbf{K}_{advt} + \mathbf{K}_{cond} + \mathbf{K}_{newt} \end{aligned}$$

in which $\mathbf{K}_{eqlb}$, $\mathbf{K}_{cont}$ and $\mathbf{K}_{thrm}$ are the stiffness matrices for equilibrium, continuity and the conservation of thermal energy; $\mathbf{K}_{grad}$ and $\mathbf{K}_{inrt}$ are the contributions to $\mathbf{K}_{eqlb}$ from the gradient of stress and from inertia; $\mathbf{K}_{advt}$, $\mathbf{K}_{cond}$ and $\mathbf{K}_{newt}$ refer to the contributions to $\mathbf{K}_{thrm}$ from advection, conduction and Newton's law of cooling; and $\mathbf{R}_{eqlb}$ and $\mathbf{R}_{thrm}$ are the load vectors for equilibrium and thermal energy. In these equations the stiffness matrices and $\mathbf{R}_{eqlb}$ are functions of the degree of freedom vector **a**.

The expanded form of the stiffness matrices and load vectors is found by substitution of the discretization (Eq. B.1) into the weighted residual forms of the governing equations (Eq. 2.26, Eq. 2.27 and Eq. 2.30). The results are as follows:

$$\begin{aligned} \mathbf{K}_{grad} &= \int_0^{le} h\mathbf{B}_u^T 4\eta \mathbf{B}_u dx_1 & \mathbf{K}_{advt} &= \rho C \int_0^{le} \mathbf{N}_T^T u_1 h \mathbf{B}_T dx_1 \\ \mathbf{K}_{inrt} &= \int_0^{le} \mathbf{N}_u^T \rho h u_1 \mathbf{B}_u dx_1 & \mathbf{K}_{cond} &= k \int_0^{le} \mathbf{B}_T^T h \mathbf{B}_T dx_1 \\ \mathbf{K}_{cont} &= \int_0^{le} \mathbf{N}_h^T \left(u_1 \mathbf{B}_h + \frac{du_1}{dx_1} \mathbf{N}_h \right) dx_1 & \mathbf{K}_{newt} &= 2\alpha \int_0^{le} \mathbf{N}_T^T \mathbf{N}_T dx_1 \end{aligned} \qquad \textbf{(B.3)}$$

$$\begin{aligned} \mathbf{R}_{eqlb} &= \rho g \int_0^{le} h \mathbf{N}_u^T dx_1 + \langle F(le) 0 \ldots - F(0) \ldots 0 \rangle^T \\ \mathbf{R}_{thrm} &= 2\alpha \int_0^{le} \mathbf{N}_T^T dx_1 \end{aligned}$$

where le is the element length.

The stiffness matrices and load vectors can be evaluated using standard Gauss quadrature, with the possible exception of $\mathbf{K}_{advt}$. If upwinding is used then the advection stiffness matrix is evaluated as:

$$\boldsymbol{K}_{advt} = \rho C u_1(O^e) h(O^e) \boldsymbol{N}_T^T(\xi) \boldsymbol{B}_T(\xi) J(O^e) \overline{W} \tag{B.4}$$

Where ξ is the optimum integration point, O^e is the origin of the isoparametric coordinates for the element, J is the Jacobian determinant of the isoparametric transformation and $\overline{W}$ is the weight factor, which is two for 1D problems.

For an element the residual is defined as:

$$\boldsymbol{\psi} \equiv [\boldsymbol{K}_{eqlb} + \boldsymbol{K}_{cont} + \boldsymbol{K}_{thrm}] \cdot \boldsymbol{a} - \boldsymbol{R}_{eqlb} - \boldsymbol{R}_{thrm} = \boldsymbol{0} \tag{B.5}$$

The tangential stiffness matrix is the derivative of each component of the residual load vector with respect to each degree of freedom:

$$\boldsymbol{K}_T(\boldsymbol{a}) \equiv \frac{d\boldsymbol{\psi}}{d\boldsymbol{a}} \tag{B.6}$$

To evaluate $\mathbf{K}_T$, the pattern in the rows of the residual load vector is used:

$$\boldsymbol{\psi} = \begin{pmatrix} \psi_{eqlb1} \\ \psi_{cont1} \\ \psi_{thrm1} \\ \psi_{eqlb2} \\ \psi_{cont2} \\ \psi_{thrm2} \end{pmatrix} = \begin{pmatrix} \psi_{eqlb1} \\ 0 \\ 0 \\ \psi_{eqlb2} \\ 0 \\ 0 \end{pmatrix} + \begin{pmatrix} 0 \\ \psi_{cont1} \\ 0 \\ 0 \\ \psi_{cont2} \\ 0 \end{pmatrix} + \begin{pmatrix} 0 \\ 0 \\ \psi_{thrm1} \\ 0 \\ 0 \\ \psi_{thrm2} \end{pmatrix} \tag{B.7}$$

or:

$$\boldsymbol{\psi} = \boldsymbol{\psi}_{eqlb} + \boldsymbol{\psi}_{cont} + \boldsymbol{\psi}_{thrm}$$

$$\therefore \frac{d\boldsymbol{\psi}}{d\boldsymbol{a}} = \frac{d\boldsymbol{\psi}_{eqlb}}{d\boldsymbol{a}} + \frac{d\boldsymbol{\psi}_{cont}}{d\boldsymbol{a}} + \frac{d\boldsymbol{\psi}_{thrm}}{d\boldsymbol{a}} \qquad \textbf{(B.8)}$$

where:

$$\begin{aligned} \boldsymbol{\psi}_{eqlb} &= \boldsymbol{K}_{eqlb}\boldsymbol{a} - \boldsymbol{R}_{eqlb} \\ \boldsymbol{\psi}_{cont} &= \boldsymbol{K}_{cont}\boldsymbol{a} \\ \boldsymbol{\psi}_{thrm} &= \boldsymbol{K}_{thrm}\boldsymbol{a} - \boldsymbol{R}_{thrm} \end{aligned} \qquad \textbf{(B.9)}$$

Equation B.9 shows that the stiffness matrices and load vectors correspond to specific rows of the residual vector. This occurs because of the first matrix in the calculation of each of the terms in Equations B.3. The matrices $\mathbf{N}_u^T$ and $\mathbf{B}_u^T$, for example, when multiplied with another matrix will result in nonzero entries only in the first and fourth rows. The result then, is that these rows correspond to the equilibrium residual ($\boldsymbol{\Psi}_{eqlb}$). A similar pattern is observed for the other two finite element equations and their associated residual load vectors ($\boldsymbol{\Psi}_{cont}$ and $\boldsymbol{\Psi}_{thrm}$).

To simplify the derivation of the tangential stiffness matrix further, the derivative with respect to the degree of freedom vector (**a**) is broken down into three steps:

$$\frac{d}{d\boldsymbol{a}} = \frac{d}{d\boldsymbol{a}_u} + \frac{d}{d\boldsymbol{a}_h} + \frac{d}{d\boldsymbol{a}_T}$$

$$\begin{aligned} \text{where } \boldsymbol{a}_u &= \langle u_{11}\ 0\ 0\ \ldots\ u_{1n}\ 0\ 0\rangle^T \\ \boldsymbol{a}_h &= \langle 0\ h_1\ 0\ \ldots\ 0\ h_n\ 0\rangle^T \\ \boldsymbol{a}_T &= \langle 0\ 0\ T_1\ \ldots\ 0\ 0\ T_n\rangle^T \end{aligned} \qquad \textbf{(B.10)}$$

The derivatives with respect to $\mathbf{a}_u$, $\mathbf{a}_h$ and $\mathbf{a}_T$ provides the columns of $\mathbf{K}_T$ that are associated with the u_1, h and T degrees of freedom, respectively. The idea then, is to

arrange the matrices that make up the residual so that the derivatives with respect to $\mathbf{a}_u$, $\mathbf{a}_h$ and $\mathbf{a}_T$ are obvious. Where possible this is done by arranging the matrix so that the terms within the integral are not a function of the degrees of freedom in question; for example, the derivative of $\mathbf{K}\mathbf{a}_u$ with respect to $\mathbf{a}_u$ is straightforward if $\mathbf{K}$ is not a function of $\mathbf{a}_u$. The vectors $\mathbf{a}_u$, $\mathbf{a}_h$ and $\mathbf{a}_T$ can be used in place of $\mathbf{a}$ when the only non-zero matrix multiplications are associated with the u_1, h and T degrees of freedom, respectively.

The derivatives are taken systematically below, for each residual, each of their components and with respect to each of the three degree of freedom vectors. For the advection stiffness matrix the derivation is shown both with and without upwinding.

1) Equilibrium Residual, $\dfrac{d\psi_{eqlb}}{d\boldsymbol{a}} = \dfrac{d}{d\boldsymbol{a}}\left(\boldsymbol{K}_{grad}\boldsymbol{a} + \boldsymbol{K}_{inrt}\boldsymbol{a} - \boldsymbol{R}_{eqlb}\right)$

a) Stress Gradient Residual, $\dfrac{d\boldsymbol{K}_{grad}\boldsymbol{a}}{d\boldsymbol{a}} = \dfrac{d\boldsymbol{K}_{grad}\boldsymbol{a}}{d\boldsymbol{a}_u} + \dfrac{d\boldsymbol{K}_{grad}\boldsymbol{a}}{d\boldsymbol{a}_h} + \dfrac{d\boldsymbol{K}_{grad}\boldsymbol{a}}{d\boldsymbol{a}_T}$

i) $\dfrac{d\boldsymbol{K}_{grad}\boldsymbol{a}}{d\boldsymbol{a}_u} = \dfrac{d}{d\boldsymbol{a}_u}\left(\int_0^{le}\boldsymbol{B}_u^T\cdot 4\eta h\boldsymbol{B}_u dx_1\,\boldsymbol{a}_u\right) = \int_0^{le}\boldsymbol{B}_u^T\cdot 4\eta h\boldsymbol{B}_u dx_1$

ii) $\dfrac{d\boldsymbol{K}_{grad}\boldsymbol{a}}{d\boldsymbol{a}_h} = \dfrac{d}{d\boldsymbol{a}_h}\left(\int_0^{le}\boldsymbol{B}_u^T\cdot\sigma_{11}\boldsymbol{N}_h dx_1\,\boldsymbol{a}_h\right) = \int_0^{le}\boldsymbol{B}_u^T\cdot\sigma_{11}\boldsymbol{N}_h dx_1$

iii) $$\frac{d\boldsymbol{K}_{grad}\boldsymbol{a}}{d\boldsymbol{a}_T} = \frac{d}{d\boldsymbol{a}_T}\int_0^{le} h\boldsymbol{B}_u^T \cdot 4\eta \frac{du_1}{dx_1} dx_1$$

$$= \int_0^{le} h\boldsymbol{B}_u^T \cdot 4 \frac{du_1}{dx_1} \frac{d\eta}{d\boldsymbol{a}_T} dx_1$$

$$= \int_0^{le} h\boldsymbol{B}_u^T \cdot 4 \frac{du_1}{dx_1} \frac{d\eta}{dT} \frac{dT}{d\boldsymbol{a}_T} dx_1$$

$$= \int_0^{le} h\boldsymbol{B}_u^T \cdot 4 \frac{du_1}{dx_1} \frac{d\eta}{dT} \frac{d\boldsymbol{N}_T\boldsymbol{a}_T}{d\boldsymbol{a}_T} dx_1 = \int_0^{le} h\boldsymbol{B}_u^T \cdot 4 \frac{du_1}{dx_1} \frac{d\eta}{dT} \boldsymbol{N}_T dx_1$$

b) Inertia Term Residual $$\frac{d\boldsymbol{K}_{inrt}\boldsymbol{a}}{d\boldsymbol{a}} = \frac{d\boldsymbol{K}_{inrt}\boldsymbol{a}}{d\boldsymbol{a}_u} + \frac{d\boldsymbol{K}_{inrt}\boldsymbol{a}}{d\boldsymbol{a}_h} + \frac{d\boldsymbol{K}_{inrt}\boldsymbol{a}}{d\boldsymbol{a}_T}$$

i) $$\frac{d\boldsymbol{K}_{inrt}\boldsymbol{a}}{d\boldsymbol{a}_u} = \frac{d}{d\boldsymbol{a}_u}\left(\int_0^{le} \boldsymbol{N}_u^T \rho h u_1 \boldsymbol{B}_u dx_1 \, \boldsymbol{a}_u \right)$$

$$= \int_0^{le} \boldsymbol{N}_u^T \rho h u_1 \boldsymbol{B}_u dx_1 + \int_0^{le} \boldsymbol{N}_u^T \rho h \frac{du_1}{d\boldsymbol{a}_u} \boldsymbol{B}_u dx_1 \, \boldsymbol{a}_u$$

$$= \int_0^{le} \boldsymbol{N}_u^T \rho h u_1 \boldsymbol{B}_u dx_1 + \int_0^{le} \boldsymbol{N}_u^T \rho h \frac{d\boldsymbol{N}_u\boldsymbol{a}_u}{d\boldsymbol{a}_u} \frac{du_1}{dx_1} dx_1$$

$$= \int_0^{le} \boldsymbol{N}_u^T \rho h u_1 \boldsymbol{B}_u dx_1 + \int_0^{le} \boldsymbol{N}_u^T \rho h \frac{du_1}{dx_1} \boldsymbol{N}_u dx_1$$

ii) $$\frac{d\boldsymbol{K}_{inrt}\boldsymbol{a}}{d\boldsymbol{a}_h} = \frac{d}{d\boldsymbol{a}_h}\left(\int_0^{le} \boldsymbol{N}_u^T \rho \frac{du_1}{dx_1} \boldsymbol{N}_h dx_1 \, \boldsymbol{a}_h \right) = \int_0^{le} \boldsymbol{N}_u^T \rho \frac{du_1}{dx_1} \boldsymbol{N}_h dx_1$$

iii) $$\frac{d\boldsymbol{K}_{inrt}\boldsymbol{a}}{d\boldsymbol{a}_T} = 0$$

c) Body Force Load Vector $\frac{d\boldsymbol{R}_{eqlb}}{d\boldsymbol{a}} = \frac{d\boldsymbol{R}_{eqlb}}{d\boldsymbol{a}_u} + \frac{d\boldsymbol{R}_{eqlb}}{d\boldsymbol{a}_h} + \frac{d\boldsymbol{R}_{eqlb}}{d\boldsymbol{a}_T}$

i) $\frac{d\boldsymbol{R}_{eqlb}}{d\boldsymbol{a}_u} = 0$

ii) $\frac{d\boldsymbol{R}_{eqlb}}{d\boldsymbol{a}_h} = \frac{d}{d\boldsymbol{a}_h}\int_0^{le} \boldsymbol{N}_u^T \rho g h dx_1 = \int_0^{le} \boldsymbol{N}_u^T \rho g \frac{d\boldsymbol{N}_h \boldsymbol{a}_h}{d\boldsymbol{a}_h} dx_1 = \int_0^{le} \boldsymbol{N}_u^T \rho g \boldsymbol{N}_h dx_1$

iii) $\frac{d\boldsymbol{R}_{eqlb}}{d\boldsymbol{a}_T} = 0$

2) Continuity Residual $\frac{d\boldsymbol{\psi}_{cont}}{d\boldsymbol{a}} = \frac{d}{d\boldsymbol{a}}\left(\boldsymbol{K}_{cont}\boldsymbol{a}\right)$

i) $\frac{d\boldsymbol{K}_{cont}\boldsymbol{a}}{d\boldsymbol{a}_u} = \frac{d}{d\boldsymbol{a}_u}\left(\int_0^{le} \boldsymbol{N}_h^T\left(\frac{dh}{dx_1}\boldsymbol{N}_u + h\boldsymbol{B}_u\right) dx_1 \boldsymbol{a}_u\right) = \int_0^{le} \boldsymbol{N}_h^T\left(\frac{dh}{dx_1}\boldsymbol{N}_u + h\boldsymbol{B}_u\right) dx_1$

ii) $\frac{d\boldsymbol{K}_{cont}\boldsymbol{a}}{d\boldsymbol{a}_h} = \frac{d}{d\boldsymbol{a}_h}\left(\int_0^{le} \boldsymbol{N}_h^T\left(\frac{du_1}{dx_1}\boldsymbol{N}_h + u_1\boldsymbol{B}_h\right) dx_1 \boldsymbol{a}_h\right) = \int_0^{le} \boldsymbol{N}_h^T\left(\frac{du_1}{dx_1}\boldsymbol{N}_h + u_1\boldsymbol{B}_h\right) dx_1$

iii) $\frac{d\boldsymbol{K}_{cont}\boldsymbol{a}}{d\boldsymbol{a}_T} = 0$

3) Thermal Energy Residual $\frac{d\boldsymbol{\psi}_{thrm}}{d\boldsymbol{a}} = \frac{d}{d\boldsymbol{a}}\left(\boldsymbol{K}_{advt}\boldsymbol{a} + \boldsymbol{K}_{cond}\boldsymbol{a} + \boldsymbol{K}_{newt}\boldsymbol{a} - \boldsymbol{R}_{thrm}\right)$

a) Advection with upwinding, $\frac{d\boldsymbol{K}_{advt}\boldsymbol{a}}{d\boldsymbol{a}} = \frac{d\boldsymbol{K}_{advt}\boldsymbol{a}}{d\boldsymbol{a}_u} + \frac{d\boldsymbol{K}_{advt}\boldsymbol{a}}{d\boldsymbol{a}_h} + \frac{d\boldsymbol{K}_{advt}\boldsymbol{a}}{d\boldsymbol{a}_T}$

i) $$\frac{d\boldsymbol{K}_{advt}\boldsymbol{a}}{d\boldsymbol{a}_u} = \frac{d}{d\boldsymbol{a}_u}\left(\boldsymbol{N}_T^T(\xi)\rho C u_1(O^e)h(O^e)\frac{dT}{dx_1}\cdot J(O^e)\cdot 2\right)$$

$$= \boldsymbol{N}_T^T(\xi)\rho C\frac{d\boldsymbol{N}_u(O^e)\boldsymbol{a}_u}{d\boldsymbol{a}_u}h(O^e)\frac{dT}{dx_1}\cdot J(O^e)\cdot 2$$

$$= \boldsymbol{N}_T^T(\xi)\rho C\,\boldsymbol{N}_u(O^e)h(O^e)\frac{dT}{dx_1}\cdot J(O^e)\cdot 2$$

ii) $$\frac{d\boldsymbol{K}_{advt}\boldsymbol{a}}{d\boldsymbol{a}_h} = \frac{d}{d\boldsymbol{a}_h}\left(\boldsymbol{N}_T^T(\xi)\rho C u_1(O^e)h(O^e)\frac{dT}{dx_1}\cdot J(O^e)\cdot 2\right)$$

$$= \boldsymbol{N}_T^T(\xi)\rho C\frac{d\boldsymbol{N}_h(O^e)\boldsymbol{a}_h}{d\boldsymbol{a}_h}u_1(O^e)\frac{dT}{dx_1}\cdot J(O^e)\cdot 2$$

$$= \boldsymbol{N}_T^T(\xi)\rho C\,\boldsymbol{N}_h(O^e)u_1(O^e)\frac{dT}{dx_1}\cdot J(O^e)\cdot 2$$

iii) $$\frac{d\boldsymbol{K}_{advt}\boldsymbol{a}}{d\boldsymbol{a}_T} = \frac{d}{d\boldsymbol{a}_T}\left(\boldsymbol{N}_T^T(\xi)\rho C u_1(O^e)h(O^e)\cdot J(O^e)\cdot 2\boldsymbol{B}_T(\xi)\,\boldsymbol{a}_T\right)$$

$$= \boldsymbol{N}_T^T(\xi)\rho C u_1(O^e)h(O^e)J(O^e)\cdot 2\boldsymbol{B}_T(\xi)$$

b) Advection standard, $$\frac{d\boldsymbol{K}_{advt}\boldsymbol{a}}{d\boldsymbol{a}} = \frac{d\boldsymbol{K}_{advt}\boldsymbol{a}}{d\boldsymbol{a}_u} + \frac{d\boldsymbol{K}_{advt}\boldsymbol{a}}{d\boldsymbol{a}_h} + \frac{d\boldsymbol{K}_{advt}\boldsymbol{a}}{d\boldsymbol{a}_T}$$

i) $$\frac{d\boldsymbol{K}_{advt}\boldsymbol{a}}{d\boldsymbol{a}_u} = \frac{d}{d\boldsymbol{a}_u}\left(\int_0^{le}\boldsymbol{N}_T^T\rho Ch\frac{dT}{dx_1}\boldsymbol{N}_u dx_1\,\boldsymbol{a}_u\right) = \int_0^{le}\boldsymbol{N}_T^T\rho Ch\frac{dT}{dx_1}\boldsymbol{N}_u dx_1$$

ii) $$\frac{d\boldsymbol{K}_{advt}\boldsymbol{a}}{d\boldsymbol{a}_h} = \frac{d}{d\boldsymbol{a}_h}\left(\int_0^{le}\boldsymbol{N}_T^T\rho Cu\frac{dT}{dx_1}\boldsymbol{N}_h dx_1\,\boldsymbol{a}_h\right) = \int_0^{le}\boldsymbol{N}_T^T\rho Cu_1\frac{dT}{dx_1}\boldsymbol{N}_h dx_1$$

iii) $$\frac{d\boldsymbol{K}_{advt}\boldsymbol{a}}{d\boldsymbol{a}_T} = \frac{d}{d\boldsymbol{a}_T}\left(\int_0^{le}\boldsymbol{N}_T^T\rho Cu_1 h\boldsymbol{B}_T dx_1\,\boldsymbol{a}_T\right) = \int_0^{le}\boldsymbol{N}_T^T\rho Cu_1 h\boldsymbol{B}_T dx_1$$

c) Conduction Residual $$\frac{d\boldsymbol{K}_{cond}\boldsymbol{a}}{d\boldsymbol{a}} = \frac{d\boldsymbol{K}_{cond}\boldsymbol{a}}{d\boldsymbol{a}_u} + \frac{d\boldsymbol{K}_{cond}\boldsymbol{a}}{d\boldsymbol{a}_h} + \frac{d\boldsymbol{K}_{cond}\boldsymbol{a}}{d\boldsymbol{a}_T}$$

i) $$\frac{d\mathbf{K}_{cond}\mathbf{a}}{d\mathbf{a}_u} = 0$$

ii) $$\frac{d\mathbf{K}_{cond}\mathbf{a}}{d\mathbf{a}_h} = \frac{d}{d\mathbf{a}_h}\left(\int_0^{le}\mathbf{B}_T^T k\frac{dT}{dx_1}\mathbf{N}_h dx_1\,\mathbf{a}_h\right) = \int_0^{le}\mathbf{B}_T^T k\frac{dT}{dx_1}\mathbf{N}_h dx_1$$

iii) $$\frac{d\mathbf{K}_{cond}\mathbf{a}}{d\mathbf{a}_T} = \frac{d}{d\mathbf{a}_T}\left(\int_0^{le}\mathbf{B}_T^T kh\mathbf{B}_T dx_1\,\mathbf{a}_T\right) = \int_0^{le}\mathbf{B}_T^T kh\mathbf{B}_T dx_1$$

d) Newton's Law of Cooling $$\frac{d\mathbf{K}_{newt}\mathbf{a}}{d\mathbf{a}} = \frac{d\mathbf{K}_{newt}\mathbf{a}}{d\mathbf{a}_u} + \frac{d\mathbf{K}_{newt}\mathbf{a}}{d\mathbf{a}_h} + \frac{d\mathbf{K}_{newt}\mathbf{a}}{d\mathbf{a}_T}$$

i) $$\frac{d\mathbf{K}_{newt}\mathbf{a}}{d\mathbf{a}_u} = 0$$

ii) $$\frac{d\mathbf{K}_{newt}\mathbf{a}}{d\mathbf{a}_h} = 0$$

iii) $$\frac{d\mathbf{K}_{newt}\mathbf{a}}{d\mathbf{a}_T} = \frac{d}{d\mathbf{a}_T}\left(\int_0^{le}\mathbf{N}_T^T\cdot 2\alpha\mathbf{N}_T dx_1\,\mathbf{a}_T\right) = \int_0^{le}\mathbf{N}_T^T\cdot 2\alpha\mathbf{N}_T dx_1$$

e) Thermal Load Vector $$\frac{d\mathbf{R}_{thrm}}{d\mathbf{a}} = \frac{d\mathbf{R}_{thrm}}{d\mathbf{a}_u} + \frac{d\mathbf{R}_{thrm}}{d\mathbf{a}_h} + \frac{d\mathbf{R}_{thrm}}{d\mathbf{a}_T}$$

The thermal load vector does not depend on any of the degrees of freedom; therefore, it does not contribute to the tangential stiffness matrix.

Now that all of the contributions to $\mathbf{K}_T$ have been found, the results can be summarized. The tangential stiffness matrix is best expressed as the assemblage of submatrices based on the terms derived above:

$$\boldsymbol{K}_T^e = \begin{bmatrix} \boldsymbol{K}_{eqlb_{u_{11}}} & \boldsymbol{K}_{eqlb_{h_{11}}} & \boldsymbol{K}_{eqlb_{T_{11}}} & \boldsymbol{K}_{eqlb_{u_{12}}} & \boldsymbol{K}_{eqlb_{h_{12}}} & \boldsymbol{K}_{eqlb_{T_{12}}} \\ \boldsymbol{K}_{cont_{u_{11}}} & \boldsymbol{K}_{cont_{h_{11}}} & \cdots & \cdots & \cdots & \boldsymbol{K}_{cont_{T_{12}}} \\ \boldsymbol{K}_{thrm_{u_{11}}} & & & & & \vdots \\ \boldsymbol{K}_{eqlb_{u_{21}}} & & & & & \vdots \\ \boldsymbol{K}_{cont_{u_{21}}} & & & & & \vdots \\ \boldsymbol{K}_{thrm_{u_{21}}} & \cdots & \cdots & \cdots & \cdots & \boldsymbol{K}_{thrm_{T_{22}}} \end{bmatrix} \quad \textbf{(B.19)}$$

Where the submatrices are:

$$\begin{aligned}
\boldsymbol{K}_{eqlb_u} &= \int_0^{le} \boldsymbol{B}^T \cdot 4\eta h \boldsymbol{B} dx_1 + \int_0^{le} \boldsymbol{N}^T \rho h u_1 \boldsymbol{B} dx_1 + \int_0^{le} \boldsymbol{N}^T \rho h \frac{du_1}{dx_1} \boldsymbol{N} dx_1 \\
\boldsymbol{K}_{eqlb_h} &= \int_0^{le} \boldsymbol{B}^T \sigma_{11} \boldsymbol{N} dx_1 + \int_0^{le} \boldsymbol{N}^T \rho \frac{du_1}{dx_1} \boldsymbol{N} dx_1 - \rho g \int_0^{le} \boldsymbol{N}^T \boldsymbol{N} dx_1 \\
\boldsymbol{K}_{eqlb_T} &= \int_0^{le} \boldsymbol{B}^T \cdot 4h \frac{du_1}{dx_1} \frac{d\eta}{dx_1} \boldsymbol{N} dx_1 \\
\boldsymbol{K}_{cont_u} &= \int_0^{le} \boldsymbol{N}^T \left(\frac{dh}{dx_1} \boldsymbol{N} + h \boldsymbol{B} \right) dx_1 \\
\boldsymbol{K}_{cont_h} &= \int_0^{le} \boldsymbol{N}^T \left(u_1 \boldsymbol{B} + \frac{du_1}{dx_1} \boldsymbol{N} \right) dx_1; \quad \boldsymbol{K}_{cont_T} = 0 \\
\boldsymbol{K}_{thrm_u} &= \rho C h(O^e) J(O^e) \cdot 2 \frac{dT}{dx_1} \boldsymbol{N}^T(\xi) \boldsymbol{N}(O^e) \\
\boldsymbol{K}_{thrm_h} &= \rho C u_1(O^e) J(O^e) \cdot 2 \frac{dT}{dx_1} \boldsymbol{N}^T(\xi) \boldsymbol{N}(O^e) + \int_0^{le} \boldsymbol{B}^T \boldsymbol{N} k \frac{dT}{dx_1} dx_1 \\
\boldsymbol{K}_{thrm_T} &= 2\rho C u_1(O^e) h(O^e) \boldsymbol{N}^T(\xi) \boldsymbol{B}(\xi) J(O^e) + \int_0^{le} \boldsymbol{B}^T h k \boldsymbol{B} dx_1 + 2\alpha \int_0^{le} \boldsymbol{N}^T \boldsymbol{N} dx_1
\end{aligned} \quad \textbf{(B.20)}$$

$$where: \boldsymbol{N} = [N_1 \ \cdots \ N_n], \ \boldsymbol{B} = \begin{bmatrix} \frac{dN_1}{dx_1} & \cdots & \frac{dN_n}{dx_1} \end{bmatrix}$$

If upwinding is not included then:

$$\boldsymbol{K}_{thrm_u} = \int_0^{le} \rho Ch \frac{dT}{dx_1} \boldsymbol{N}^T \boldsymbol{N} dx_1$$

$$\boldsymbol{K}_{thrm_h} = \int_0^{le} \rho Cu_1 \frac{dT}{dx_1} \boldsymbol{N}^T \boldsymbol{N} dx_1 + \int_0^{le} \boldsymbol{B}^T \boldsymbol{N} k \frac{dT}{dx_1} dx_1$$

$$\boldsymbol{K}_{thrm_T} = \int_0^{le} \rho Cu_1 h \boldsymbol{N}^T \boldsymbol{B} dx_1 + \int_0^{le} \boldsymbol{B}^T hk \boldsymbol{B} dx_1 + 2\alpha \int_0^{le} \boldsymbol{N}^T \boldsymbol{N} dx_1$$

B.2 Derivation of 2D Tangential Stiffness Matrices

The derivation of the 2D tangential stiffness matrices follows the same approach as for the 1D matrix. However, the 2D case involves the additional complexities of a second velocity degree of freedom and an unknown free surface. To simplify the presentation, the stiffness matrices for the field variables and for the free surface are derived separately.

Local Tangential Stiffness Matrix for the Field Variables

To express the governing equations in finite element form involves a change of notation; therefore, the first part of this presentation details the 2D finite element notation. For three-noded constant stress triangular (CST) elements the velocity vector (**u** ~ u_α), thickness (h) and temperature (T) are expressed in terms of the degree of freedom vectors (**a**, $\mathbf{a}_u$, $\mathbf{a}_h$, $\mathbf{a}_T$) and the shape functions (N_1, N_2, N_3):

$$
\begin{aligned}
\boldsymbol{a} &= \langle u_{11}\ u_{21}\ h_1\ T_1\ u_{12}\ u_{22}\ h_2\ T_2\ u_{13}\ u_{23}\ h_3\ T_3\rangle^T \\
\boldsymbol{a}_u &= \langle u_{11}\ u_{21}\ 0\ 0\ u_{12}\ u_{22}\ 0\ 0\ u_{13}\ u_{23}\ 0\ 0\rangle^T \\
\boldsymbol{a}_h &= \langle 0\ 0\ h_1\ 0\ 0\ 0\ h_2\ 0\ 0\ 0\ h_3\ 0\rangle^T \\
\boldsymbol{a}_T &= \langle 0\ 0\ 0\ T_1\ 0\ 0\ 0\ T_2\ 0\ 0\ 0\ T_3\rangle^T \\
\boldsymbol{u} &= \langle u_1\ u_2\rangle^T = \boldsymbol{N}_u\boldsymbol{a} \\
h &= \boldsymbol{N}_h\boldsymbol{a} \\
T &= \boldsymbol{N}_T\boldsymbol{a} \\
\boldsymbol{N}_u &= \begin{bmatrix} N_1\ 0\ 0\ 0\ N_2\ 0\ 0\ 0\ N_3\ 0\ 0\ 0 \\ 0\ N_1\ 0\ 0\ 0\ N_2\ 0\ 0\ 0\ N_3\ 0\ 0 \end{bmatrix} \\
\boldsymbol{N}_h &= [0\ 0\ N_1\ 0\ 0\ 0\ N_2\ 0\ 0\ 0\ N_3\ 0] \\
\boldsymbol{N}_T &= [0\ 0\ 0\ N_1\ 0\ 0\ 0\ N_2\ 0\ 0\ 0\ N_3]
\end{aligned}
\qquad \textbf{(B.22)}
$$

For CST elements the shape functions are equal to the area coordinates (L_1, L_2, L_3); that is, $N_i = L_i$, where i equals 1 to 3.

The rest of finite element notation is introduced in the context of the constitutive equation, momentum equation, continuity equation and conservation of energy equation. Each of these equations is considered in turn by converting the index notation expression into a finite element notation equivalent.

i) Constitutive Equation

$$\sigma_{\alpha\beta} = 2\eta(\varepsilon_{\alpha\beta} + \varepsilon_{\gamma\gamma}\delta_{\alpha\beta}) \tag{B.23}$$

The stress and strain vectors are defined as follows:

$$\boldsymbol{\sigma} = \begin{pmatrix} \sigma_{11} \\ \sigma_{22} \\ \sigma_{12} \end{pmatrix} \sim \sigma_{\alpha\beta}; \qquad \boldsymbol{\varepsilon} = \begin{pmatrix} \varepsilon_{11} \\ \varepsilon_{22} \\ \gamma_{12} \end{pmatrix} \sim \varepsilon_{\alpha\beta};\ \gamma_{12} = 2\varepsilon_{12} \tag{B.24}$$

The strain vector in terms of the degree of freedom vector is expressed as

$$\boldsymbol{\varepsilon} = \boldsymbol{L}\boldsymbol{u}, \text{ where } \boldsymbol{L} = \begin{bmatrix} \frac{\partial}{\partial x_1} & 0 \\ 0 & \frac{\partial}{\partial x_2} \\ \frac{\partial}{\partial x_2} & \frac{\partial}{\partial x_1} \end{bmatrix} \tag{B.25}$$

$$\therefore \boldsymbol{\varepsilon} = \boldsymbol{B}_u\boldsymbol{a}, \text{ where } \boldsymbol{B}_u = \boldsymbol{L}\boldsymbol{N}_u$$

To relate the stress to the strain a constitutive matrix is introduced as follows:

$$\boldsymbol{\sigma} = \boldsymbol{D\varepsilon}, \text{ where } \boldsymbol{D} = \eta \begin{bmatrix} 4 & 2 & 0 \\ 2 & 4 & 0 \\ 0 & 0 & 1 \end{bmatrix} \tag{B.26}$$

ii) Momentum Equation

$$\int_{\Omega} \delta \varepsilon_{\alpha\beta} \sigma_{\alpha\beta} h d\Omega + \int_{\Omega} \delta u_{\alpha} \rho h u_{\beta} \frac{\partial u_{\alpha}}{\partial x_{\beta}} d\Omega = \int_{\Omega} \delta u_{\alpha} \rho h b_{\alpha} d\Omega \tag{B.27}$$

To express this equation in a finite element notation a gradient operator is introduced:

$$\nabla = \begin{pmatrix} \dfrac{\partial}{\partial x_1} \\ \dfrac{\partial}{\partial x_2} \end{pmatrix} \tag{B.28}$$

This operator is used to express the gradient of the velocity vector:

$$\frac{\partial u_{\alpha}}{\partial x_{\beta}} \sim (\nabla \boldsymbol{u}^{T})^{T} = \begin{bmatrix} \dfrac{\partial u_1}{\partial x_1} & \dfrac{\partial u_1}{\partial x_2} \\ \dfrac{\partial u_2}{\partial x_1} & \dfrac{\partial u_2}{\partial x_2} \end{bmatrix} \tag{B.29}$$

To express this matrix in terms of the degree of freedom vector the following matrix expansion is introduced:

$$\begin{aligned}\begin{bmatrix} \frac{\partial u_1}{\partial x_1} & \frac{\partial u_1}{\partial x_2} \\ \frac{\partial u_2}{\partial x_1} & \frac{\partial u_2}{\partial x_2} \end{bmatrix} &= \begin{bmatrix} \frac{\partial}{\partial x_1} & 0 \\ 0 & \frac{\partial}{\partial x_1} \end{bmatrix} \begin{pmatrix} u_1 \\ u_2 \end{pmatrix} [1\ 0] + \begin{bmatrix} \frac{\partial}{\partial x_2} & 0 \\ 0 & \frac{\partial}{\partial x_2} \end{bmatrix} \begin{pmatrix} u_1 \\ u_2 \end{pmatrix} [0\ 1] \\ &= \boldsymbol{L}_{x_1} \boldsymbol{u} [1\ 0] + \boldsymbol{L}_{x_2} \boldsymbol{u} [0\ 1] \\ &= \boldsymbol{L}_{x_1} \boldsymbol{N}_u \boldsymbol{a} [1\ 0] + \boldsymbol{L}_{x_2} \boldsymbol{N}_u \boldsymbol{a} [0\ 1] \\ &= \boldsymbol{B}_{x_1} \boldsymbol{a} [1\ 0] + \boldsymbol{B}_{x_2} \boldsymbol{a} [0\ 1] \end{aligned} \quad \textbf{(B.30)}$$

Finally, a vector is introduced for expressing the acceleration vector:

$$\boldsymbol{b} = \langle g_{x_1}\ 0 \rangle^T \quad \textbf{(B.31)}$$

in which g_{x1} is the component of the acceleration due to gravity in the x_1 direction.

iii) Continuity Equation

$$\int_\Omega \delta h \left(\frac{\partial h}{\partial x_\alpha} u_\alpha + h \frac{\partial u_\alpha}{\partial x_\alpha} \right) d\Omega = 0 \quad \textbf{(B.32)}$$

The gradient operator can be used to express the thickness and velocity gradients as follows:

$$\begin{aligned} \frac{\partial h}{\partial x_\alpha} &\sim \nabla h = \boldsymbol{B}_{hh} \boldsymbol{a}, \text{ where } \boldsymbol{B}_{hh} = \nabla \boldsymbol{N}_h \\ \frac{\partial u_\alpha}{\partial x_\alpha} &\sim \nabla^T \boldsymbol{u} = \boldsymbol{B}_{hu} \boldsymbol{a}, \text{ where } \boldsymbol{B}_{hu} = \nabla^T \boldsymbol{N}_u \end{aligned} \quad \textbf{(B.33)}$$

iv) Conservation of Thermal Energy Equation

$$\int_\Omega \delta T \rho C h u_\alpha \frac{\partial T}{\partial x_\alpha} d\Omega + \int_\Omega \frac{\partial \delta T}{\partial x_\alpha} k h \frac{\partial T}{\partial x_\alpha} d\Omega + \int_\Omega \delta T \cdot 2\alpha T d\Omega = \int_\Omega \delta T \cdot 2\alpha T_{air} d\Omega \quad \textbf{(B.34)}$$

Once again the gradient operator is used, this time for the temperature gradient:

$$\frac{\partial T}{\partial x_\alpha} \sim \nabla T = \boldsymbol{B}_T \boldsymbol{a}, \text{ where } \boldsymbol{B}_T = \nabla \boldsymbol{N}_T \qquad \textbf{(B.35)}$$

With the notation defined, it is now possible to proceed with the derivation of the tangential stiffness matrix. This derivation follows the same approach as that outlined above for the 1D case; that is, the derivatives are taken for each residual, each of their components and with respect to each of the three degree of freedom vectors.

1) Equilibrium Residual, $\frac{d\boldsymbol{\psi}_{eqlb}}{d\boldsymbol{a}} = \frac{d}{d\boldsymbol{a}}\left(\boldsymbol{K}_{grad}\boldsymbol{a} + \boldsymbol{K}_{inrt}\boldsymbol{a} - \boldsymbol{R}_{eqlb}\right)$

a) Stress Gradient Residual, $\frac{d\boldsymbol{K}_{grad}\boldsymbol{a}}{d\boldsymbol{a}} = \frac{d\boldsymbol{K}_{grad}\boldsymbol{a}}{d\boldsymbol{a}_u} + \frac{d\boldsymbol{K}_{grad}\boldsymbol{a}}{d\boldsymbol{a}_h} + \frac{d\boldsymbol{K}_{grad}\boldsymbol{a}}{d\boldsymbol{a}_T}$

i) $\frac{d\boldsymbol{K}_{grad}\boldsymbol{a}}{d\boldsymbol{a}_u} = \frac{d}{d\boldsymbol{a}_u}\left(\int_\Omega \boldsymbol{B}_u^T \boldsymbol{D}\boldsymbol{B}_u h d\Omega\, \boldsymbol{a}_u\right) = \int_\Omega \boldsymbol{B}_u^T \boldsymbol{D}\boldsymbol{B}_u h d\Omega$

ii) $\frac{d\boldsymbol{K}_{grad}\boldsymbol{a}}{d\boldsymbol{a}_h} = \frac{d}{d\boldsymbol{a}_h}\left(\int_\Omega \boldsymbol{B}_u^T \boldsymbol{\sigma}\boldsymbol{N}_h d\Omega\, \boldsymbol{a}_h\right) = \int_\Omega \boldsymbol{B}_u^T \boldsymbol{\sigma}\boldsymbol{N}_h d\Omega$

iii) $\frac{d\boldsymbol{K}_{grad}\boldsymbol{a}}{d\boldsymbol{a}_T} = \frac{d}{d\boldsymbol{a}_T}\int_\Omega \boldsymbol{B}_u^T \eta \hat{\boldsymbol{D}}\boldsymbol{\varepsilon} h d\Omega$, *where* $\hat{\boldsymbol{D}} = \frac{1}{\eta}\boldsymbol{D}$

$$= \int_\Omega \boldsymbol{B}_u^T \hat{\boldsymbol{D}}\boldsymbol{\varepsilon} h \frac{d\eta}{d\boldsymbol{a}_T} d\Omega$$

$$= \int_\Omega \boldsymbol{B}_u^T \hat{\boldsymbol{D}}\boldsymbol{\varepsilon} h \frac{d\eta}{dT}\frac{dT}{d\boldsymbol{a}_T} d\Omega$$

$$= \int_\Omega \boldsymbol{B}_u^T \hat{\boldsymbol{D}}\boldsymbol{\varepsilon} h \frac{d\eta}{dT}\frac{d\boldsymbol{N}_T\boldsymbol{a}_T}{d\boldsymbol{a}_T} d\Omega = \int_\Omega \boldsymbol{B}_u^T \hat{\boldsymbol{D}}\boldsymbol{\varepsilon} h \frac{d\eta}{dT}\boldsymbol{N}_T d\Omega$$

b) Inertia Term Residual $\frac{d\boldsymbol{K}_{inrt}\boldsymbol{a}}{d\boldsymbol{a}} = \frac{d\boldsymbol{K}_{inrt}\boldsymbol{a}}{d\boldsymbol{a}_u} + \frac{d\boldsymbol{K}_{inrt}\boldsymbol{a}}{d\boldsymbol{a}_h} + \frac{d\boldsymbol{K}_{inrt}\boldsymbol{a}}{d\boldsymbol{a}_T}$

i) $\frac{d\boldsymbol{K}_{inrt}\boldsymbol{a}}{d\boldsymbol{a}_u} = \frac{d}{d\boldsymbol{a}_u}\left(\int_\Omega \boldsymbol{N}_u^T \rho h (\nabla \boldsymbol{u}^T)^T \boldsymbol{N}_u d\Omega\, \boldsymbol{a}_u\right)$

$$= \int_\Omega \boldsymbol{N}_u^T \rho h (\nabla \boldsymbol{u}^T)^T \boldsymbol{N}_u d\Omega + \frac{d}{d\boldsymbol{a}_u}\int_\Omega \boldsymbol{N}_u^T \rho h (\nabla \boldsymbol{u}^T)^T \boldsymbol{u} d\Omega$$

$$= \int_\Omega \boldsymbol{N}_u^T \rho h (\nabla \boldsymbol{u}^T)^T \boldsymbol{N}_u d\Omega + \frac{d}{d\boldsymbol{a}_u}\int_\Omega \boldsymbol{N}_u^T \rho h (\boldsymbol{B}_{x_1}\boldsymbol{a}_u[1\ 0] + \boldsymbol{B}_{x_2}\boldsymbol{a}_u[0\ 1])\boldsymbol{u} d\Omega$$

$$= \int_\Omega \boldsymbol{N}_u^T \rho h (\nabla \boldsymbol{u}^T)^T \boldsymbol{N}_u d\Omega + \frac{d}{d\boldsymbol{a}_u}\int_\Omega \boldsymbol{N}_u^T \rho h (\boldsymbol{B}_{x_1}u_1 + \boldsymbol{B}_{x_2}u_2) d\Omega \boldsymbol{a}_u$$

$$= \int_\Omega \boldsymbol{N}_u^T \rho h (\nabla \boldsymbol{u}^T)^T \boldsymbol{N}_u d\Omega + \int_\Omega \boldsymbol{N}_u^T \rho h (\boldsymbol{B}_{x_1}u_1 + \boldsymbol{B}_{x_2}u_2) d\Omega$$

ii) $\frac{d\boldsymbol{K}_{inrt}\boldsymbol{a}}{d\boldsymbol{a}_h} = \frac{d}{d\boldsymbol{a}_h}\left(\int_\Omega \boldsymbol{N}_u^T \rho (\nabla \boldsymbol{u}^T)^T \boldsymbol{u}\boldsymbol{N}_h d\Omega\, \boldsymbol{a}_h\right) = \int_\Omega \boldsymbol{N}_u^T \rho (\nabla \boldsymbol{u}^T)^T \boldsymbol{u}\boldsymbol{N}_h d\Omega$

iii) $\frac{d\boldsymbol{K}_{inrt}\boldsymbol{a}}{d\boldsymbol{a}_T} = 0$

c) Body Force Load Vector $\frac{d\boldsymbol{R}_{eqlb}}{d\boldsymbol{a}} = \frac{d\boldsymbol{R}_{eqlb}}{d\boldsymbol{a}_u} + \frac{d\boldsymbol{R}_{eqlb}}{d\boldsymbol{a}_h} + \frac{d\boldsymbol{R}_{eqlb}}{d\boldsymbol{a}_T}$

i) $\frac{d\boldsymbol{R}_{eqlb}}{d\boldsymbol{a}_u} = 0$

ii) $\frac{d\boldsymbol{R}_{eqlb}}{d\boldsymbol{a}_h} = \frac{d}{d\boldsymbol{a}_h}\int_\Omega \boldsymbol{N}_u^T \boldsymbol{b}\rho \boldsymbol{N}_h d\Omega \boldsymbol{a}_h = \int_\Omega \boldsymbol{N}_u^T \boldsymbol{b}\rho \boldsymbol{N}_h d\Omega$

iii) $\frac{d\boldsymbol{R}_{eqlb}}{d\boldsymbol{a}_T} = 0$

2) Continuity Residual $\frac{d\boldsymbol{\psi}_{cont}}{d\boldsymbol{a}} = \frac{d}{d\boldsymbol{a}}\left(\boldsymbol{K}_{cont}\boldsymbol{a}\right)$

i) $\frac{d\boldsymbol{K}_{cont}\boldsymbol{a}}{d\boldsymbol{a}_u} = \frac{d}{d\boldsymbol{a}_u}\left(\int_\Omega \boldsymbol{N}_h^T\left((\nabla h)^T\boldsymbol{N}_u + h\boldsymbol{B}_{hu}\right)d\Omega\,\boldsymbol{a}_u\right) = \int_\Omega \boldsymbol{N}_h^T\left((\nabla h)^T\boldsymbol{N}_u + h\boldsymbol{B}_{hu}\right)d\Omega$

ii) $\frac{d\boldsymbol{K}_{cont}\boldsymbol{a}}{d\boldsymbol{a}_h} = \frac{d}{d\boldsymbol{a}_h}\left(\int_\Omega \boldsymbol{N}_h^T\left(\nabla^T\boldsymbol{u}\boldsymbol{N}_h + \boldsymbol{u}\boldsymbol{B}_{hh}\right)d\Omega\,\boldsymbol{a}_h\right) = \int_\Omega \boldsymbol{N}_h^T\left(\nabla^T\boldsymbol{u}\boldsymbol{N}_h + \boldsymbol{u}\boldsymbol{B}_{hh}\right)d\Omega$

iii) $\frac{d\boldsymbol{K}_{cont}\boldsymbol{a}}{d\boldsymbol{a}_T} = 0$

3) Thermal Energy Residual $\frac{d\boldsymbol{\psi}_{thrm}}{d\boldsymbol{a}} = \frac{d}{d\boldsymbol{a}}\left(\boldsymbol{K}_{advt}\boldsymbol{a} + \boldsymbol{K}_{cond}\boldsymbol{a} + \boldsymbol{K}_{newt}\boldsymbol{a} - \boldsymbol{R}_{thrm}\right)$

a) Advection, $\frac{d\boldsymbol{K}_{advt}\boldsymbol{a}}{d\boldsymbol{a}} = \frac{d\boldsymbol{K}_{advt}\boldsymbol{a}}{d\boldsymbol{a}_u} + \frac{d\boldsymbol{K}_{advt}\boldsymbol{a}}{d\boldsymbol{a}_h} + \frac{d\boldsymbol{K}_{advt}\boldsymbol{a}}{d\boldsymbol{a}_T}$

i) $\frac{d\boldsymbol{K}_{advt}\boldsymbol{a}}{d\boldsymbol{a}_u} = \frac{d}{d\boldsymbol{a}_u}\left(\int_\Omega \boldsymbol{N}_T^T\rho Ch(\nabla T)^T\boldsymbol{N}_u d\Omega\,\boldsymbol{a}_u\right) = \int_\Omega \boldsymbol{N}_T^T\rho Ch(\nabla T)^T\boldsymbol{N}_u d\Omega$

ii) $\frac{d\boldsymbol{K}_{advt}\boldsymbol{a}}{d\boldsymbol{a}_h} = \frac{d}{d\boldsymbol{a}_h}\left(\int_\Omega \boldsymbol{N}_T^T\rho C(\nabla T)^T\boldsymbol{u}\boldsymbol{N}_h d\Omega\,\boldsymbol{a}_h\right) = \int_\Omega \boldsymbol{N}_T^T\rho C(\nabla T)^T\boldsymbol{u}\boldsymbol{N}_h d\Omega$

iii) $$\frac{d\boldsymbol{K}_{advt}\boldsymbol{a}}{d\boldsymbol{a}_T} = \frac{d}{d\boldsymbol{a}_T}\left(\int_\Omega \boldsymbol{N}_T^T \rho C h \boldsymbol{u}^T \boldsymbol{B}_T d\Omega\, \boldsymbol{a}_T\right) = \int_\Omega \boldsymbol{N}_T^T \rho C h \boldsymbol{u}^T \boldsymbol{B}_T d\Omega$$

b) Conduction Residual $$\frac{d\boldsymbol{K}_{cond}\boldsymbol{a}}{d\boldsymbol{a}} = \frac{d\boldsymbol{K}_{cond}\boldsymbol{a}}{d\boldsymbol{a}_u} + \frac{d\boldsymbol{K}_{cond}\boldsymbol{a}}{d\boldsymbol{a}_h} + \frac{d\boldsymbol{K}_{cond}\boldsymbol{a}}{d\boldsymbol{a}_T}$$

i) $$\frac{d\boldsymbol{K}_{cond}\boldsymbol{a}}{d\boldsymbol{a}_u} = 0$$

ii) $$\frac{d\boldsymbol{K}_{cond}\boldsymbol{a}}{d\boldsymbol{a}_h} = \frac{d}{d\boldsymbol{a}_h}\left(\int_\Omega \boldsymbol{B}_T^T k (\nabla T)^T \boldsymbol{N}_h d\Omega\, \boldsymbol{a}_h\right) = \int_\Omega \boldsymbol{B}_T^T k (\nabla T)^T \boldsymbol{N}_h d\Omega$$

iii) $$\frac{d\boldsymbol{K}_{cond}\boldsymbol{a}}{d\boldsymbol{a}_T} = \frac{d}{d\boldsymbol{a}_T}\left(\int_\Omega \boldsymbol{B}_T^T k h \boldsymbol{B}_T d\Omega\, \boldsymbol{a}_T\right) = \int_\Omega \boldsymbol{B}_T^T k h \boldsymbol{B}_T d\Omega$$

c) Newton's Law of Cooling $$\frac{d\boldsymbol{K}_{newt}\boldsymbol{a}}{d\boldsymbol{a}} = \frac{d\boldsymbol{K}_{newt}\boldsymbol{a}}{d\boldsymbol{a}_u} + \frac{d\boldsymbol{K}_{newt}\boldsymbol{a}}{d\boldsymbol{a}_h} + \frac{d\boldsymbol{K}_{newt}\boldsymbol{a}}{d\boldsymbol{a}_T}$$

i) $$\frac{d\boldsymbol{K}_{newt}\boldsymbol{a}}{d\boldsymbol{a}_u} = 0$$

ii) $$\frac{d\boldsymbol{K}_{newt}\boldsymbol{a}}{d\boldsymbol{a}_h} = 0$$

iii) $$\frac{d\boldsymbol{K}_{newt}\boldsymbol{a}}{d\boldsymbol{a}_T} = \frac{d}{d\boldsymbol{a}_T}\left(\int_\Omega \boldsymbol{N}_T^T \cdot 2\alpha \boldsymbol{N}_T d\Omega\, \boldsymbol{a}_T\right) = \int_\Omega \boldsymbol{N}_T^T \cdot 2\alpha \boldsymbol{N}_T d\Omega$$

d) Thermal Load Vector $$\frac{d\boldsymbol{R}_{thrm}}{d\boldsymbol{a}} = \frac{d\boldsymbol{R}_{thrm}}{d\boldsymbol{a}_u} + \frac{d\boldsymbol{R}_{thrm}}{d\boldsymbol{a}_h} + \frac{d\boldsymbol{R}_{thrm}}{d\boldsymbol{a}_T}$$

The thermal load vector does not depend on any of the degrees of freedom; therefore, it does not contribute to the tangential stiffness matrix.

Now that all of the contributions to $\mathbf{K}_T$ have been found, the results can be summarized. The tangential stiffness matrix is best expressed as the assemblage of submatrices based on the terms derived above:

$$\boldsymbol{K}_T^e = \begin{bmatrix} \boldsymbol{K}_{eqlb_{u_{11}}} & \boldsymbol{K}_{eqlb_{u_{12}}} & \boldsymbol{K}_{eqlb_{h_{11}}} & \boldsymbol{K}_{eqlb_{T_{11}}} & \boldsymbol{K}_{eqlb_{u_{13}}} & \boldsymbol{K}_{eqlb_{u_{14}}} & \cdots & \boldsymbol{K}_{eqlb_{T_{13}}} \\ \boldsymbol{K}_{eqlb_{u_{21}}} & \boldsymbol{K}_{eqlb_{u_{22}}} & \boldsymbol{K}_{eqlb_{h_{21}}} & \boldsymbol{K}_{eqlb_{T_{21}}} & \cdots & \cdots & \cdots & \boldsymbol{K}_{eqlb_{T_{23}}} \\ \boldsymbol{K}_{cont_{u_{11}}} & \boldsymbol{K}_{cont_{u_{12}}} & \cdots & \cdots & \cdots & \cdots & \cdots & \boldsymbol{K}_{cont_{T_{13}}} \\ \boldsymbol{K}_{thrm_{u_{11}}} & & & & & & & \vdots \\ \boldsymbol{K}_{eqlb_{u_{31}}} & & & & & & & \vdots \\ \boldsymbol{K}_{eqlb_{u_{41}}} & & & & & & & \vdots \\ \boldsymbol{K}_{cont_{u_{21}}} & & & & & & & \vdots \\ \boldsymbol{K}_{thrm_{u_{21}}} & & & & & & & \vdots \\ \boldsymbol{K}_{eqlb_{u_{51}}} & & & & & & & \vdots \\ \boldsymbol{K}_{eqlb_{u_{61}}} & & & & & & & \vdots \\ \boldsymbol{K}_{cont_{u_{31}}} & & & & & & & \vdots \\ \boldsymbol{K}_{thrm_{u_{31}}} & \cdots & \cdots & \cdots & \cdots & \cdots & \cdots & \boldsymbol{K}_{thrm_{T_{33}}} \end{bmatrix} \quad \textbf{(B.43)}$$

Where the submatrices are defined as follows:

$$
\begin{aligned}
\boldsymbol{K}_{eqlb_u} &= \int_\Omega \boldsymbol{B}_u^T \boldsymbol{D} \boldsymbol{B}_u h d\Omega + \int_\Omega \boldsymbol{N}_u^T \rho h (\nabla \boldsymbol{u}^T)^T \boldsymbol{N}_u d\Omega + \int_\Omega \boldsymbol{N}_u^T \rho h (\boldsymbol{B}_{x_1} u_1 + \boldsymbol{B}_{x_2} u_2) d\Omega \\
\boldsymbol{K}_{eqlb_h} &= \int_\Omega \boldsymbol{B}_u^T \boldsymbol{\sigma} \boldsymbol{N}_s d\Omega + \int_\Omega \boldsymbol{N}_u^T \rho (\nabla \boldsymbol{u}^T)^T \boldsymbol{u} \boldsymbol{N}_s d\Omega - \int_\Omega \boldsymbol{N}_u^T \boldsymbol{b} \rho \boldsymbol{N}_s d\Omega \\
\boldsymbol{K}_{eqlb_T} &= \int_\Omega \boldsymbol{B}_u^T \hat{\boldsymbol{D}} h \boldsymbol{\varepsilon} \frac{d\eta}{dT} \boldsymbol{N}_s d\Omega \\
\boldsymbol{K}_{cont_u} &= \int_\Omega \boldsymbol{N}_s^T \left((\nabla h)^T \boldsymbol{N}_u + h \boldsymbol{B}_{us} \right) d\Omega \\
\boldsymbol{K}_{cont_h} &= \int_\Omega \boldsymbol{N}_s^T \left(\boldsymbol{u} \boldsymbol{B}_{ss} + \nabla^T \boldsymbol{u} \boldsymbol{N}_s \right) d\Omega \\
\boldsymbol{K}_{cont_T} &= \boldsymbol{0} \\
\boldsymbol{K}_{thrm_u} &= \int_\Omega \boldsymbol{N}_s^T \rho C h (\nabla T)^T \boldsymbol{N}_u d\Omega \\
\boldsymbol{K}_{thrm_h} &= \int_\Omega \boldsymbol{N}_s^T \rho C u (\nabla T)^T \boldsymbol{u} \boldsymbol{N}_s d\Omega + \int_\Omega \boldsymbol{B}_{ss}^T k (\nabla T)^T \boldsymbol{N}_s d\Omega \\
\boldsymbol{K}_{thrm_T} &= \int_\Omega \boldsymbol{N}_s^T \rho C h \boldsymbol{u}^T \boldsymbol{B}_{ss} d\Omega + \int_\Omega \boldsymbol{B}_{ss}^T h k \boldsymbol{B}_{ss} d\Omega + \int_\Omega \boldsymbol{N}_s^T \cdot 2\alpha \boldsymbol{N}_s^T d\Omega
\end{aligned}
\tag{B.44}
$$

The shape function and shape function gradient matrices used above have the following definitions:

$$
\begin{aligned}
\boldsymbol{N}_u &= \begin{bmatrix} N_1 & 0 & N_2 & 0 & N_3 & 0 \\ 0 & N_1 & 0 & N_2 & 0 & N_3 \end{bmatrix} \\
\boldsymbol{N}_s &= [N_1 \; N_2 \; N_3] \\
\boldsymbol{B}_u &= \boldsymbol{L} \boldsymbol{N}_u \\
\boldsymbol{B}_{x_1} &= \boldsymbol{L}_{x_1} \boldsymbol{N}_u \\
\boldsymbol{B}_{x_2} &= \boldsymbol{L}_{x_2} \boldsymbol{N}_u \\
\boldsymbol{B}_{us} &= \nabla^T \boldsymbol{N}_u \\
\boldsymbol{B}_{ss} &= \nabla \boldsymbol{N}_s
\end{aligned}
\tag{B.45}
$$

in which the u represents the matrices associated with velocity vector and the s represents the matrices associated with the thickness and temperature scalars.

Local Tangential Stiffness Matrix for the Free Surface Calculation

For the two-noded surface elements the velocity vector (**u**), thickness (h), temperature (T) and width are expressed in terms of the degree of freedom vectors (**a**, $\mathbf{a}_u$, $\mathbf{a}_h$, $\mathbf{a}_T$, $\mathbf{a}_w$) and the shape functions (N_1, N_2):

$$
\begin{aligned}
\boldsymbol{a} &= \langle u_{11}\ u_{21}\ h_1\ T_1\ w_1\ u_{12}\ u_{22}\ h_2\ T_2\ w_2 \rangle^T \\
\boldsymbol{a}_u &= \langle u_{11}\ u_{21}\ 0\ 0\ 0\ u_{12}\ u_{22}\ 0\ 0\ 0 \rangle^T \\
\boldsymbol{a}_h &= \langle 0\ 0\ h_1\ 0\ 0\ 0\ 0\ h_2\ 0\ 0 \rangle^T \\
\boldsymbol{a}_T &= \langle 0\ 0\ 0\ T_1\ 0\ 0\ 0\ 0\ T_2\ 0 \rangle^T \\
\boldsymbol{a}_w &= \langle 0\ 0\ 0\ 0\ w_1\ 0\ 0\ 0\ 0\ w_2 \rangle^T \\
\boldsymbol{u} &= \langle u_1\ u_2 \rangle^T = \boldsymbol{N}_u \boldsymbol{a} \\
h &= \boldsymbol{N}_h \boldsymbol{a} \\
T &= \boldsymbol{N}_T \boldsymbol{a} \\
w &= \boldsymbol{N}_w \boldsymbol{a} \\
\frac{dw}{dx_1} &= \frac{d\boldsymbol{N}_w}{dx_1}\boldsymbol{a} = \boldsymbol{B}_w \boldsymbol{a} \\
\boldsymbol{N}_u &= \begin{bmatrix} N_1\ 0\ 0\ 0\ 0\ N_2\ 0\ 0\ 0\ 0 \\ 0\ N_1\ 0\ 0\ 0\ 0\ N_2\ 0\ 0\ 0 \end{bmatrix} \\
\boldsymbol{N}_h &= [0\ 0\ N_1\ 0\ 0\ 0\ 0\ N_2\ 0\ 0] \\
\boldsymbol{N}_T &= [0\ 0\ 0\ N_1\ 0\ 0\ 0\ 0\ N_2\ 0] \\
\boldsymbol{N}_w &= [0\ 0\ 0\ 0\ N_1\ 0\ 0\ 0\ 0\ N_2]
\end{aligned}
\qquad \textbf{(B.46)}
$$

This discretization can be substituted into the free surface equation to yield the free surface residual:

$$\psi_{wdth} = \boldsymbol{K}_{wdth}\boldsymbol{a} - \boldsymbol{R}_{wdth} = 0$$

$$\text{where } \boldsymbol{K}_{wdth} = \int_0^{le} \boldsymbol{N}_w^T \frac{dw}{dx_1} u_1 ds;\ \boldsymbol{R}_{wdth} = \int_0^{le} \boldsymbol{N}_w^T u_2 ds \qquad \textbf{(B.47)}$$

where s is the distance along the free surface.

The procedure for finding the tangential stiffness matrix for the free surface is the same as that used above, except that the temperature degrees of freedom have no influence and there are now width degrees of freedom.

Width Residual, $\dfrac{d\psi_{wdth}}{d\boldsymbol{a}} = \dfrac{d}{d\boldsymbol{a}}\left(\boldsymbol{K}_{wdth}\boldsymbol{a} - \boldsymbol{R}_{wdth}\right)$

a) Tangential from stiffness matrix, $\dfrac{d\boldsymbol{K}_{wdth}\boldsymbol{a}}{d\boldsymbol{a}} = \dfrac{d\boldsymbol{K}_{wdth}\boldsymbol{a}}{d\boldsymbol{a}_u} + \dfrac{d\boldsymbol{K}_{wdth}\boldsymbol{a}}{d\boldsymbol{a}_h} + \dfrac{d\boldsymbol{K}_{wdth}\boldsymbol{a}}{d\boldsymbol{a}_w}$

i) $\dfrac{d\boldsymbol{K}_{wdth}\boldsymbol{a}}{d\boldsymbol{a}_u} = \dfrac{d}{d\boldsymbol{a}_u}\left(\int_0^{le} \boldsymbol{N}_w^T \frac{dw}{dx_1}[1\ 0]\boldsymbol{N}_u ds\, \boldsymbol{a}_u\right) = \int_0^{le} \boldsymbol{N}_w^T \frac{dw}{dx_1}[1\ 0]\boldsymbol{N}_u ds$

ii) $\dfrac{d\boldsymbol{K}_{wdth}\boldsymbol{a}}{d\boldsymbol{a}_h} = 0$

iii) $\dfrac{d\boldsymbol{K}_{wdth}\boldsymbol{a}}{d\boldsymbol{a}_w} = \dfrac{d}{d\boldsymbol{a}_w}\int_0^{le} \boldsymbol{N}_w^T[1\ 0]\boldsymbol{u}\boldsymbol{B}_w ds\boldsymbol{a}_w = \int_0^{le} \boldsymbol{N}_w^T u_1 \boldsymbol{B}_w ds$

b) Tangential for load vector $\dfrac{d\boldsymbol{R}_{wdth}}{d\boldsymbol{a}} = \dfrac{d\boldsymbol{R}_{wdth}}{d\boldsymbol{a}_u} + \dfrac{d\boldsymbol{R}_{wdth}}{d\boldsymbol{a}_h} + \dfrac{d\boldsymbol{R}_{wdth}}{d\boldsymbol{a}_w}$

i) $\dfrac{d\boldsymbol{R}_{wdth}}{d\boldsymbol{a}_u} = \dfrac{d}{d\boldsymbol{a}_u}\left(\int_0^{le} \boldsymbol{N}_w^T[0\ 1]\boldsymbol{N}_u ds\, \boldsymbol{a}_u\right) = \int_0^{le} \boldsymbol{N}_w^T[0\ 1]\boldsymbol{N}_u ds$

ii) $\frac{d\boldsymbol{R}_{wdth}}{d\boldsymbol{a}_{h}} = 0$

iii) $\frac{d\boldsymbol{R}_{wdth}}{d\boldsymbol{a}_{w}} = 0$

The submatrices derived above can be assembled into a local 10x10 tangential stiffness matrix for the determination of the free surface.